

Linear and nonlinear magnetization dynamics in
permalloy thin films grown on DNA origami and
nanopatterned permalloy/YIG hybrid structures

Présentée le 9 juin 2023

Faculté des sciences et techniques de l'ingénieur
Laboratoire des matériaux magnétiques nanostructurés et magnoniques
Programme doctoral en science et génie des matériaux

pour l'obtention du grade de Docteur ès Sciences

par

Andrea MUCCHIETTO

Acceptée sur proposition du jury

Dr A. Hessler-Wyser, présidente du jury
Prof. D. Grundler, directeur de thèse
Dr C. Adelman, rapporteur
Prof. A. Barman, rapporteur
Dr G. Boero, rapporteur

A dog can not make this journey alone,
but maybe a wolf can.
— Bob Hoskins: Boris

To my family...

Acknowledgements

In this section I want to acknowledge the people that supported me inside and outside the work environment throughout the period of my PhD research.

I thank **Prof. Grundler** first for giving me the opportunity to conduct research in his group and for trusting me with this project. With your guidance, I succeeded in overcoming hard times that were part of my PhD journey. You have constantly shared your technical and theoretical knowledge, that you have worked hard to earn. I truly appreciate that. I thank **Prof. Bastings** for supporting me during my efforts to optimize and fabricate DNA lattices. I am grateful that you allowed me to work in your laboratory using your experimental setups. I thank **Dr. Hessler-Wyser** for being available to act as jury president of my oral examination committee. I thank **Dr. Adelmann**, **Prof. Barman** and **Dr. Boero** for agreeing to evaluate my thesis and join as scientific experts my oral examination committee. I want to thank all my senior LMGN colleagues that supported me daily since the start of my PhD. They shared with me an enormous amount of valuable knowledge covering nanofabrication, experimental setups and measurements and data analysis. I have learnt a lot from all of you. Here they are: **Dr. K. Baumgärtl**, Thank you for sharing your knowledge on BLS, nanofabrication and VNA. It has been a pleasure working with you, I appreciate the fact you involved me in your work and we cooperated together during the XMCD beamtime. **Dr. S. Watanabe**, Thank you so much for sharing your know-how on VNA and AFM/MFM setups. I am grateful to you for being always open to discuss nanofabrication steps. I am thankful to you for allowing me to contribute to your work. **Dr. M. C. Giordano**, Thank you so much for your support and life advices in and out of the lab life. Your resilience and enthusiasm for science are exemplary. Thank you for trusting me with the BLS setup and making me part of some of your measurements of spin wave dynamics in nanotubes. **Dr. P. Che**, Many thanks to you Ping that were always available to help and discuss any problem and issue I would encounter. Working together it is has been really enriching for me, I am happy we could cooperate on several projects. **Dr. A. Kukol'ova**, I thank you for setting a great example of tenacity in that you completed a very challenging PhD. I am glad we had a chance to collaborate, I thank you for that. **Dr. M. Hamdi**, We shared a lot of laughs, food and chats beyond all the stimulating scientific discussions. I am so happy that I have been your colleague and office mate. Thank you so much for sharing your passion on science and physics and always being eager to discuss science and theory. I

benefitted immensely from your knowledge and expertise. **Dr. V. S. Bhat**, Thank you for your initial support on micromagnetic simulation and our collaboration on spin wave excitations in quasicrystals. **Dr. K. An**, Thank you for sharing your knowledge on VNA and on simulations. To the LMGN members that arrived around my 3rd year of PhD I am grateful for bringing a new wave of fresh energy! I thank **H. Guo**, **S. S. Joglekar**, **Dr. M. Xu**, **A. J. M. Deenen** and **A. Duvakina** for all the interesting discussions during the group meeting and the amazing lab retreats. I thank A. Duvakina for taking over and continuing the exciting and challenging project on bridging DNA nanotechnology and nanomagnonics. I thank all the EPFL students that during these years trusted me with being their supervisor for semester projects. To the PBL team at EPFL I am thankful for accepting me as collaborator and supporting me with any advice on how to improve my workflow in DNA nanotechnology. In particular I want to thank: **Dr. E. Kurisinkal**, Thank you very much Eva all the training sessions on fundamentals of DNA nanotechnology and the related experimental setups. I appreciate the fact you always made the time to support me whenever I was struggling with the preparation of the DNA honeycomb lattice, especially in the beginning. **Dr. H. Bila**, Thank you for welcoming me to the PBL lab and most importantly, thank you for being ready to help at any time no matter how busy you were. **Cem Tekin**, Thank you for sharing your experience on DNA preparation and characterization with in-liquid and in-air AFM. To **Dr. S. Mieszczak**, thank you for bringing to LMGN such an exciting project on spin wave confinement which I have had great pleasure to contribute to. I thank you Szymon and Dr. M. Xu for this collaboration. For our collaboration on X-ray - magnon scattering I am thankful to **Dr. S. Wittrock**, **Dr. M. Schneider**, **Dr. B. Pfau**, **Dr. D. Schick** and **Christopher Klose**. This project has stimulated me to expand my knowledge on many aspects and the discussions with our collaborators have always led to exciting and stimulating ideas pushing always forward the research. For the technical support on DNA origami I thank **Dr. J-P. Sobczak**, **Dr. A. A. Rafat** and **Dr. T. Aigner**. I am sincerely grateful to the entire **CMi staff** for managing and maintaining such top-notch facility for nanofabrication at EPFL. I thank the CMi staff for the daily support in the cleanroom. I thank **Dr. C. Dubs** for providing the 11-nm-thick YIG thin film. **SNSF** is acknowledged for financial support via grant 197360.

To the **Nanotech crew**, a sincere thank you for always finding the strength 'to set the bar at a higher level'. I thank **my family** for being there at any moment during both the dark and the bright moments ready to share a smile, a life lesson, an advice and for their unconditional trust and support in my plans and dreams. To **my father** and **my mother** I express my immense gratitude for their patience, for their passion, for their guidance and for all the lessons that they have taught me... and still are teaching me!. To **my sister**, you are always full of enthusiasm that you effortlessly transmit to those around you. An heartfelt 'thank you' for that and for your trust in me.

Lausanne, May 22, 2023

A. M.

Abstract

Spin waves (SWs) are collective excitations of the spin ensemble in systems with magnetic order. In quantum mechanics, a SW is known as a magnon, which is the quasiparticle describing the quantized nature of these wave-like excitations. Magnonics is the research branch in magnetism that studies magnon excitation, propagation and detection in micro- and nanostructures with the ultimate goal to control and engineer magnons for future applications in telecommunications and information processing. Indeed magnons exist in the GHz-THz range possessing wavelengths λ_m that can be as small as few nm. This frequency regime is that assigned to telecommunications. By a propagating magnon, angular momentum flows without electrical charge motion. Hence magnons can propagate through oxides with magnetic order as well. The absence of Joule heating and the short λ_m have raised significant technological interest in engineering magnon-based devices to process and store information as candidate solutions to the conventional-nanoelectronics conundrum of achieving simultaneously device miniaturization, power efficiency and high operational speed. The dynamic magnetic field of a microwave antenna (CPW) irradiated by electromagnetic waves (EMWs) excites magnons in an adjacent magnetic layer. The wavelength mismatch of EMW and magnons at the same frequency limits the coupling efficiency. However to enhance coupling to magnons with $\lambda_m < 100$ nm periodic arrays of nanomagnets are integrated at the interface between the CPW and the magnetic layer. The periodic nanomagnets act as grating coupler (GC) improving the microwave-to-magnon transduction. To optimize the GC functionality unprecedented downscaling of nanomagnet arrangements below 100 nm is sought. Such lateral length scale hard to achieve with routinely available tools for top-down nanofabrication. In our work we fabricate ferromagnetic grating couplers on low damping YIG ($Y_3Fe_5O_{12}$) thin film with 11 and 113 nm thickness. We study microwave-to-magnon transduction in the linear and non-linear regime up to few tens of GHz. Beyond chiral magnon properties in 11 nm thick YIG we explore the magnon-induced reversal of the nanomagnets integrated on top of YIG. Our study as a function of thickness characterizes the power efficiency of magnetization switching by different magnon resonances in hybrid structures for which we realized different interfacial coupling. We found that magnon pulses propagating in both directions induce magnetization reversal. The asymmetric group velocities for chiral magnons in the 11-nm-thick YIG are studied for wavelength down to $\lambda_m = 99$ nm. Stimulated by the efficient magnon excitation via grating couplers in top-down nanopatterned hybrid structures we then explore a novel route to create periodically modulated nanomagnets. We investigate DNA-based nanopatterning tool for feature sizes below 50 nm. In surface-corrugated ferromagnetic thin films we observe

a frequency shift of the magnon band minimum, modified resonance frequencies of confined magnon modes and, by performing micromagnetic simulations, predict the formation of nanoengineered band structures in surface-corrugated thin films with a lateral modulation on the 30-nm length scale. Our results foster the development of novel miniaturized magnetic grating couplers and stimulates future device design and optimization to achieve low-power in-memory computing via short-waved magnons and the magnon-induced reversal effect.

Keywords: Spin waves, magnonics, YIG, DMI, magnonic grating coupler effect, magnon-induced magnetization reversal, Brillouin light scattering, inductive broadband spectroscopy, DNA nanotechnology, micromagnetic modelling

Zusammenfassung

Spinwellen (SWs) sind kollektive Anregungen der Spins in Materialien mit magnetischer Ordnung. In der Quantenmechanik wird eine SW als Magnon bezeichnet, das als Quasiteilchen die quantisierte Natur dieser Anregung beschreibt. Magnonik ist die Forschungsrichtung im Magnetismus, die die Physik und Methoden in Bezug auf Spinwellen Anregung, Ausbreitung and Detektion in Mikro- und Nanostrukturen erarbeitet. Das endgültige Ziel ist, Spinwellen für zukünftige Anwendungen im Bereich der Kommunikations- und der Informationstechnik zu funktionalisieren. Spinwellen existieren in dem GHz bis THz Frequenzintervall und die Wellenlänge kann so kurz wie wenige nm sein. Dieses Frequenzintervall ist bedeutsam für die Kommunikationstechnik. Bei der Ausbreitung einer Spinwelle wird das Drehimpulsmoment ohne Bewegung der Elektronen übertragen. Daher können sich Spinwellen durch Metalle und Oxide, die magnetische Ordnung haben, ausbreiten. Die Abwesenheit der Joule-Wärme und die kurze Wellenlänge haben eine wichtige technologische Relevanz für die Geräte, die Signalen und Daten mit Spinwellen verarbeiten sollen. Ein solches Gerät, das auf Spinwellen basiert, ist eine vielversprechende Lösung für die Herausforderungen der Halbleiter-basierten Nanoelektronik, nämlich die gleichzeitige Verbesserung der Bauelement-verkleinerung, der Leistung-Effizienz und der Verarbeitungsgeschwindigkeit. Die Zeit-abhängige magnetische Feld des koplanaren Wellenleiters regt Spinwellen in einer benachbarten magnetischen Schicht an. Die Fehlanpassung der Wellenlänge von elektromagnetischer Welle und Magnon bei der gleichen Frequenz beschränkt die Kopplung-Effizienz. Magnetische Nanostrukturen mit periodischer Ordnung auf der Grenzfläche zwischen dem Wellenleiter und der magnetischen Schicht sind geeignet um die Kopplung zu Spinwellen, die eine Wellenlänge kürzer als 100 nm haben, zu verstärken. Die periodischen Nanomagnete wirken als Gitterkoppler, die die Transduktion zwischen elektromagnetischen Wellen and Spinwellen verbessern. Um die Funktionalität des Gitterkopplers zu optimieren forschen wir an der Verkleinerung periodischer magnetischen Strukturen unter die 100 nm Längenskala. Solcher Längenmaßstab ist schwer erreichbar mit alltäglicher verfügbarer Top-down Nanofabrikation. In unserer Forschungsarbeit erzeugen wir ferromagnetische Gitterkoppler auf Yttrium-Eisen-Granat (YIG) Schichten, die 11 und 113 nm dünn sind und eine niedriger Spinwellendaämpfung haben. Wir erforschen die Transduktion von elektromagnetischen Wellen zu Spinwellen in dem linearen and nicht-linearen Anregungsbereich bis ungefähr 10 GHz. Neben den chiralen Eigenschaften der Spinwellen in dem 11-nm dicken YIG untersuchen wir die Schaltung der Magnetisierungsrichtung von bistabilen Nanomagneten, die auf YIG-Schichten liegen, aufgrund von sich ausbreitenden YIG-Spinwellen. Betreffs der Schaltung der Magnetisierungsrichtung cha-

rakterisieren wir die Leistung-Effizienz and die Abhängigkeit von der Dicke verschiedener Zwischenschichten zwischen YIG and Nanomagneten. Wir finden dass der Magnetisierungsvektor durch Spinwellen-Pulse, die sich in zwei gegenläufige entgegen beider Richtungen ausbreiten, geschaltet werden kann. In 11-nm dicken YIG sind die unsymmetrischen Gruppengeschwindigkeiten der chiralen Spinwellen für Wellenlängen so kurz wie 99 nm ermittelt werden. Wir wenden DNA-basierte Nanotechnologie an, um strukturelle Eigenschaften der Magnete auf einer Längenskala von weniger als 50 nm zu verändern. In ferromagnetischen Dünnschichten von der DNA erzeugten mit Oberflächen-Modulation beobachten wir eine Frequenzveränderung des Spinwellen-Bandstrukturminimums und eine Frequenzveränderung der Spinwellenresonanz, die durch die Dicke bestimmt ist. Mit mikromagnetischen Simulationen sagen wir die Entstehung einer künstlichen Bandstruktur in ferromagnetischen Dünnschichten mit Oberflächen-Welligkeit voraus, die mit einer Periode von 30 nm variiert. Unsere Ergebnisse fördern die Entwicklung verkleinerter magnetischer Gitterkoppler. Sie ermöglichen die Optimierung von Hybridstrukturen, die mit niedriger Leistung In-Memory-Computing durch Spinwellen mit kurzen Wellenlängen und durch Spinwellensignalspeicherung zum Ziel haben.

Stichwörter: Spinwelle, Magnonik, YIG, DMI, magnetische Gitterkoppler effekt, Magnetisierungsrichtung Schaltung bei propagierenden Spinwellen, Brillouin Lichtsstreuung, induktive breitband Spektroskopie, DNA Nanotechnologie, mikromagnetische Modellierung

Contents

Acknowledgements	i
Abstract (English/Français/Deutsch)	iii
List of figures	xi
List of tables	xiii
1 Research motivation and introduction	1
2 Theory and literature review	5
2.1 Basic concepts of magnetism	5
2.2 Energy terms in micromagnetism	7
2.2.1 Heisenberg exchange energy	7
2.2.2 Dzyaloshinskii-Moriya interaction	7
2.2.3 Zeeman energy	8
2.2.4 Demagnetization energy	8
2.2.5 Magnetocrystalline anisotropy	9
2.2.6 Stoner-Wohlfarth model	9
2.2.7 Effective magnetic field	10
2.3 Magnetization dynamics	11
2.3.1 Landau-Lifshitz-Gilbert equation	11
2.4 Ferromagnetic resonance	11
2.5 Magnon dispersion	13
2.6 Magnon dispersion in the presence of iDMI	16
2.7 Magnonic crystals (MCs)	17
2.8 The magnonic grating coupler effect	17
2.9 Magnon-magnon cooperativity	19
2.10 Angular momentum transfer and magnetization switching	19
3 Methods	23
3.1 Micromagnetic simulations	23
3.2 All-electrical spin wave spectroscopy (AESWS)	24
3.2.1 General aspects of inductive broadband spectroscopy	24
3.2.2 Coplanar waveguide design and excitation spectrum	26

3.2.3	Group velocity and amplitude non-reciprocity	27
3.2.4	Displaying measured spectra	28
3.3	Brillouin light scattering	29
3.3.1	Basics of Brillouin light scattering (BLS) process	29
3.3.2	BLS microscopy setup	30
3.4	Top-down nanofabrication	33
3.4.1	Fabrication of one-dimensional periodic arrays of Py stripes	33
3.4.2	Fabrication of coplanar waveguides on Py stripes	34
3.5	Bottom-up magnonics nanotechnology based on DNA	35
3.5.1	DNA structure and chemistry	35
3.5.2	DNA nanotechnology	37
3.5.3	Bottom-up driven down scaling of magnonic grating couplers	38
3.5.4	Annealing and deposition protocols of DNA honeycomb lattice	41
3.5.5	Gel electrophoresis	44
3.5.6	Evaporation of Py on DNA on a bare mica substrate	45
3.5.7	DNA deposition on pre-processed substrates	46
4	Results	49
4.1	Magnon-induced reversal of Py stripes integrated on 113-nm-thick YIG	49
4.1.1	All-electrical spin-wave spectroscopy characterization	49
4.1.2	Switching yield diagram	54
4.1.3	Multi-frequency magnon-assisted nanomagnet reversal resolved by microfocus BLS	57
4.1.4	Magnon-assisted nanomagnet reversal by magnon pulses with μ BLS	60
4.2	Inductive spectroscopy of LPE-grown 11-nm-thick YIG	62
4.2.1	Field-dependent VNA spectra and avoided crossing	63
4.2.2	Magnon-assisted switching: switching field distribution and switching yield diagram	65
4.2.3	Amplitude non-reciprocity, chiral magnon propagation and iDMI estimation	67
4.3	Thermal magnon spectra of bottom-up nanopatterned Py and YIG thin films	70
4.3.1	Atomic force microscopy characterization of DNA origami on mica	71
4.3.2	BLS microscopy of thermal magnons	71
4.3.3	Perpendicular standing spin waves in a DNA-decorated YIG thin film	74
4.3.4	Towards unprecedented miniaturization of magnonic crystals	76
5	Conclusions and outlook	81
5.1	Conclusions	81
5.2	Outlook	83
A	Appendix	85
A.1	Methods	85
A.1.1	Experimental equipment for the preparation of DNA samples	85

A.1.2	Annealing protocol for the customized DNA origami lattice ordered and obtained from Tilibit nanosystems	85
A.2	Experimental data	86
A.2.1	Magnon-induced reversal in 113-nm-thick YIG	86
A.2.2	Inductive spectroscopy of LPE-grown 11-nm-thick YIG	87
A.2.3	BLS measurements of confined magnon modes in corrugated Py	87
A.2.4	Additional micromagnetic simulation data	89
A.3	Scripts	90
Bibliography		110
Curriculum Vitae		111

List of Figures

2.1	Stoner-Wohlfarth model	10
2.2	Polder susceptibility	13
2.3	KS model for YIG	14
2.4	Band structure for surface corrugated thin film - literature review	18
2.5	Coupling regimes and cooperativity	19
2.6	Stoner-Wohlfarth mode for non-zero external field	22
3.1	MuMax3 simulation geometry	24
3.2	Scattering matrix and VNA setup	25
3.3	CPW excitation, real and reciprocal space spectrum	26
3.4	Transmission VNA spectra	27
3.5	BLS: Magnon-photon scattering process	30
3.6	Sketch of the whole BLS setup at LMGN	31
3.7	BLS chip mount and chip view through the GGG substrate	32
3.8	BLS wave vector limit and KS formalism	33
3.9	Process flow	34
3.10	DNA constituents and double helix model	36
3.11	DNA nucleotides' structures	37
3.12	DNA-PF2 origami sketch	39
3.13	DNA-tile self-assembly of DNA honeycomb lattice	42
3.14	Gel electrophoresis	45
3.15	Bottom up miniaturization of grating couplers by DNA lattices	46
3.16	Process steps to obtain surface corrugated Py with DNA templates	47
4.1	VNA measurement at -25 dBm of S_{21} in Py/Cu/YIG	50
4.2	VNA reflection spectra on 113-nm-thick YIG	51
4.3	VNA Transmission spectra on 113nm YIG	52
4.4	Extraction method for critical fields	53
4.5	Critical fields comparison in 113nm YIG	54
4.6	Switching yield at 14 mT in 113nm YIG	55
4.7	Switching power efficiency of magnons in 113-nm-thick YIG	56
4.8	BLS overview: BLS illumination, BLS laser focus spot and spectra	57
4.9	Thermal magnons in Py/Cu stripes measured by spatially-resolved μ BLS	58

4.10 BLS measurements on Py/Cu stripes with magnon continuous wave excitation	59
4.11 BLS backside illumination for time-resolved BLS measurements	60
4.12 BLS spectra before and after magnon pulses at 2 GHz and 4.15 GHz	60
4.13 BLS spectra before and after magnon pulses at 4.15 GHz for large power levels	61
4.14 VNA spectra for Py/SiO ₂ /YIG devices at $P_{\text{irr}} = -9$ dBm	63
4.15 +50 mT DE spectra in 11nm YIG with different YIG/Py	64
4.16 Estimated cooperativity for Py/YIG and Py/SiO ₂ /YIG GC devices	64
4.17 AESWS spectra for 11-nm-thick YIG	66
4.18 Critical fields estimated for 11-nm-thick YIG	66
4.19 Switching yield in 11-nm-thick YIG for 34 and 38 mT	67
4.20 Switching yield for stripes on 11-nm-thick YIG	68
4.21 Magnon amplitude non-reciprocity between $\text{Mag}(S_{21})$ and $\text{Mag}(S_{12})$	68
4.22 Group velocities of magnons in 11-nmYIG at $P_{\text{irr}} = -5$ and -1 dBm	69
4.23 Group velocity in 11-nm-thick YIG for $k = 2.75 \text{ rad}/\mu\text{m}$	70
4.24 AFM real and reciprocal space of DNA lattice	72
4.25 AFM analysis of surface corrugated Py on DNA origami	72
4.26 Sketch of BLS experiment	73
4.27 Raw BLS frequency spectra, f_{res} , FWHM and N_x of surface corrugated Py	74
4.28 Magnon band minimum BLS characterization and comparison with AFM	75
4.29 AFM of Py/DNA-PF2/YIG	75
4.30 BLS frequency spectra for Py/DNA-PF2/YIG	76
4.31 Spin pinning boundary parameter fit on BLS data for Py/DNA-PF2/YIG	77
4.32 Micromagnetic simulation of magnon band structure in surface-corrugated Py thin films	78
4.33 AFM of DNA honeycomb lattice before and after evaporation of 3-nm-thick Py	80
5.1 Outlook: magnetic bit pattern writing by magnon interference	84
A.1 Experimental equipment in PBL	85
A.2 Switching yield 20 mT	87
A.3 Switching yield 14 mT of nanostripes beneath the emitter CPW	88
A.4 Switching yield 20 mT of nanostripes beneath the emitter CPW	88
A.5 S_{12} and S_{21} spectra for 11nm YIG	89
A.6 Spin pinning parameter fit	89
A.7 Band gap width and center at 180, 150 and 60 mT of different surface corrugated thin films	90

List of Tables

4.1	Magnon amplitude non-reciprocity η	68
4.2	Estimated iDMI values in 11-nm-thick LPE-grown YIG	70

1 Research motivation and introduction

Magnetization fluctuations around its equilibrium configuration are called spin waves (SWs) [20]. In quantum mechanics SWs are referred to as *magnons* which are the quasiparticle describing the discrete nature of such spin excitations. Magnon resonances falls within the relevant frequency range for information and communication technology [56]. In the same frequency regime GHz-THz, electromagnetic waves in air have a wavelength $\lambda_{EM} \sim$ cm while magnons feature a wavelength $\lambda \sim$ nm \div μ m. Magnon propagation carries angular momentum flow without electron motion. This avoids Joule heating. Therefore magnons represent a valid candidate for a novel information carrier in a future non-charge-based beyond-CMOS technology in that information is processed by wave-based operations.

Nanomagnonics is the research field combining physics, device design and materials science to investigate and control magnon propagation in magnetic nanostructures. To establish nanomagnonics as a future paradigm for the computing technology efficient control of magnon dispersion with $\lambda_m < 100$ nm (short-waved magnons) must be achieved. This enables unprecedented downscaling of operating device while preserving high operational speed (i.e. high group velocity) and low power consumption. To excite short-waved magnons magnonic crystals are fabricated by nanostructuring magnetic films mostly relying on conventional top-down nanolithography. A magnonic crystal (MC) is fabricated by periodically patterning a magnetic structure so that an artificial band structure is formed with transmission and stop bands for magnon propagation. MCs have been engineered to operate as grating couplers (GC) when integrated between a microwave antenna and an underlying magnetic layer where magnons can propagate [60]. The GC functionality is crucial to realize optimal coupling to short-waved magnons overcoming the wavelength mismatch that exists between λ_m and λ_{EM} . In the past years MCs have been integrated on low damping YIG thin films [127], [115] and advanced control of short-waved magnon at the nanoscale has been demonstrated via the magnon grating coupler effect [60]. These works proved the potential of a magnon-based technology to achieve logic operations utilizing short-waved magnons at low fields and steering magnon beams by means of ad-hoc artificially patterned crystals [127] and experimentally discovered the magnon-induced reversal of nanomagnet switching [115], [133]. The magnon-

induced nanomagnet reversal is an important discovery to push forward nanomagnonics as future wave-based computing technology. The magnon-induced nanomagnet reversal demonstrates the ability to use magnons to write magnetic bits without conversion to the electrical domain. State-of-the-art nanomagnonics relies on top-down nanopatterning. This technique has been so far highly successful. However the main design rule for GC suggests to miniaturize the GC in order to enhance the coupling to short-waved magnons. Conventional lithography faces at least two bottlenecks: (i) the tool spatial resolution determined by the electron or photon wavelength used for exposure and (ii) the resolution, linewidth roughness and sensitivity of chemical resists that are used in the patterning process. To advance state-of-the-art nanolithography new materials are being investigated as resist candidates at ~ 10 nm resolution and techniques based extreme ultraviolet lithography or synchrotron radiation are being optimized [128], [138], [139]. These are stimulating results that are however based on tools and facilities that are hard to get access routinely. As the technology-driven trend urgently requires miniaturization, the lateral dimensions of nanomagnets are shrunk down at length scales for which exchange interactions dominate the magnon dispersion thus leading to an isotropic behavior. However to maximize the full potential of nanomagnonics it is desired to preserve and still control the anisotropic magnon dispersion even at large wave vector (k). Recently several works have addressed this aspect investigating chiral and unidirectional magnon propagation in ultra thin films. The presence of interfacial Dzyaloshinskii-Moriya interaction (iDMI) has been observed in ultra thin films of low magnon damping materials [135], [114] revealing asymmetric magnon group velocity.

Motivated by the current progress in the field of nanomagnonics and its open challenges, we focus on three main topics in this thesis:

- Magnon-induced nanomagnet reversal characterization

This effect was discovered in a hybrid structure Py/YIG with direct interface [133]. The authors reported a nonlinear phenomenon in that Py stripes' magnetization is reversed by spin waves (SWs) propagating over $25 \mu\text{m}$. We aim at a deeper microscopic understanding of the mechanism. We propose to investigate which interactions are relevant for the magnon-induced reversal. We prepare two types of device. Between Py and YIG we place a spacer layer made of (i) 5-nm-thick Cu or (ii) 5-nm-thick SiO_2 . The former suppresses direct magnetic exchange while still allowing for spin current transmission and dipole-dipole interaction, whereas the latter suppresses the spin current transmission allowing only for dipole-dipole interaction. By inductive spectroscopy (AESWS, section 3.2) and laser-based magnon detection (BLS, section 3.3) we measure both types of magnetic interfaces. We study their magnetization dynamics at different irradiation power P_{irr} levels in order to explore the effect of linear and non-linear dynamics. We characterize the critical fields and critical powers that determines magnon-induced nanomagnet reversal. We also characterize the switching power efficiency of differ magnon resonances. Stimulated by the several inspiring works of short-waved magnons in ultra thin YIG films (e.g. [125], [125]) we investigate the same effect in 11-nm-thick and 113-nm-thick YIG so to unveil the thickness-dependence of magnon-induced reversal. To

summarize, in this part of the thesis (sections 4.1 and partly 4.2) we address:

- Switching dependence of magnetic interface Py/YIG
- Switching power efficiency
- Switching by magnon pulses
- Thickness dependence of switching

- Magnetization dynamics in 11-nm-thick YIG

By inductive broadband spectroscopy we probe magnetization dynamics of liquid-phase-epitaxy grown 11-nm-thick YIG with integrated ferromagnetic nanostripes. The nanostripes act as grating couplers thus enabling short-waved magnons. We detect magnons with a wavelength as small as $\lambda_m = 99$ nm. We probe the chiral propagation of short-waved magnons by extracting the group velocity v_g . We characterize magnon non-reciprocity and iDMI. By preparing devices with direct exchange Py/YIG and with an interlayer spacer 5-nm-thick SiO_2 the magnetization dynamics in the hybrid structure Py/YIG is explored for different interfacial coupling. Magnon-induced reversal is investigated to complete the thickness-dependence study. To summarize, in this second part (section 4.2) of the thesis we focus on:

- Large- k magnon excitation and detection in ultra thin film YIG
- Magnon amplitude non-reciprocity and chiral propagation characterization
- Py/YIG coupling

- Bottom-up approach to achieve sub-50-nm patterning

In the third part of this thesis we explore the application of DNA nanotechnology as nanopatterning tool to fabricate periodically patterned nanomagnets with lateral modulation < 50 nm. Lateral modulation by surface corrugation has already been investigated via top-down approaches based on etching and lithography. Surface modulation as thin as 2 nm has been demonstrated to lead to band structure formation in thin films [85], [97]. These results stimulate us to pursue a novel route for nanostructuring magnetic thin films that has the potential to go beyond the limitations of our top-down lithography processes. Hence we propose combining DNA nanotechnology and nanomagnonics. Our overarching goal is to realize magnonic crystals (MCs) with the first Brillouin zone falling in the exchange-dominated range of wave vectors for magnon propagation. MCs can then be integrated in a magnonic device to operate as grating coupler. We expect this to enhance the coupling to exchange-dominated magnons. The lattice pitch ranges from 120 nm down to 31 nm. With the support of the Programmable Biomaterials Laboratory at EPFL ([140]) we prepare a DNA-based 2D honeycomb lattice. For other sets of DNA samples we rely on commercially available designs provided by

Tilibit nanosystems GmbH ([141]). The geometry of the commercially available DNA lattice is based on a square lattice. We select geometries with different rotational symmetries to explore magnon dispersion in artificial crystals with different symmetry axis. This allows us to compare with accomplished works on similar geometries fabricated by top-down nanopatterning. Considering the high-risk nature of such project we complement our experimental efforts with micromagnetic modelling of ferromagnetic thin films. Here we study magnon band structure formation in Py thin films featuring the surface topography modulation of the real systems. The simulations provide a further validation towards the feasibility of our approach. We numerically explore the influence of Py film thickness in the formation of a band structure induced by the surface corrugation. We experimentally characterize the DNA lattice structural integrity with atomic force microscopy (AFM) and optimize deposition protocols for DNA on different substrates. We evaporate Py thin films on DNA-decorated surfaces. We characterize the topography of the thin film and consequently investigate the thermally-activated magnetization dynamics by BLS. In this part (section. 4.3) of the research we work on:

- Micromagnetic modelling of magnon band structure in surface corrugated thin films
- Optimization of DNA deposition protocols in dry environment on mica and on YIG
- AFM characterization of DNA lattice geometries
- BLS study of thermally-activated magnetization dynamics in surface corrugated thin films grown on DNA

In this report we first introduce the basics of micromagnetism and magnon dispersion in ferromagnetic thin films with and without iDMI (chapter 2). Then the experimental techniques of all-electrical spin wave spectroscopy (section 3.2) and Brillouin light scattering setup (section 3.3) are discussed along with micromagnetic modelling (section 3.1) and sample fabrication (sections 3.5 and 3.4). Chapter 4 presents and discusses the main experimental outcome of this PhD project. In chapter 5 we summarize the experimental outcome highlighting the main conclusions of this work and providing an outlook to future research that this work inspires.

2 Theory and literature review

In this chapter we introduce the main concepts of magnetism and micromagnetics. We review the models and formula concerning magnon dispersion and magnonic crystals which are relevant for this thesis. We conclude with a review of DNA nanotechnology and our strategy how it can be exploited to create magnets patterned at so far not achieved lateral length scales.

2.1 Basic concepts of magnetism

Quantum electrodynamics attributes microscopic magnetic momenta μ_q to spin and angular momenta of electrons. The total magnetic moment \mathbf{m} is related to the total angular momentum \mathbf{J} by the following relationship

$$\mathbf{m} = \gamma \mathbf{J} \quad (2.1)$$

\mathbf{J} is obtained by summation of spin and orbital momenta (for detailed review of summation rules [44]); $\gamma = \frac{g\mu_0|e|}{2m_e}$ is the gyromagnetic ration ([20]) with $|e|$, m_e , μ_0 and g being respectively the electron charge, the electron mass, the vacuum permeability and the Landé factor (numerical values can be found in [34]). For metallic ferromagnets the approximations $\mathbf{J} \approx \mathbf{S}$ and $g \approx 2$ hold true. The projection of the electron spin along one direction is $\frac{\hbar}{2}$, with \hbar being the reduced Planck's constant. The magnetic moment of an electron is $\mu_B = \frac{|e|\hbar}{2m_e}$ and it is labelled as Bohr magneton. These quantities have quantized nature and modelling of physical phenomena at the atomic length scale must consider this. For micro- and nano-structures, as those investigated in this thesis, a classical approach, assuming the system to be a continuum, can still be utilized. In the continuum limit, one defines the magnetization $\mathbf{M} = \sum_i \mathbf{m}_i / V$ as the magnetic moment density where V is the volume over which the summation is performed. This physical quantity allows to classify a material's response to an external magnetic field \mathbf{H} according to the relationship:

$$\mathbf{M} = \vec{\chi} \mathbf{H} \quad (2.2)$$

$\vec{\chi}$ is referred to the magnetic susceptibility tensor. In case of homogeneous and isotropic materials, the magnetic susceptibility is a scalar quantity χ . According to its sign and magnitude, materials are classified as follows:

Diamagnetic materials have no permanent magnetic moment. In the presence of an external field \mathbf{H} , a weak magnetization is formed against \mathbf{H} . χ is negative and $|\chi| \sim 10^{-5}$.

In paramagnetic materials permanent magnetic moments exist that are not ordered at zero field. Increasing the external field leads to magnetic alignment thus giving rise to a macroscopic non-zero \mathbf{M} . χ is positive and $|\chi| \sim 10^{-4}$

Ferromagnetic and antiferromagnetic materials possess permanent magnetic moments as well. Spontaneous magnetic ordering is of quantum-mechanical nature. The ordering is driven by exchange interaction. Exchange interaction favors anti-parallel (parallel) alignment of neighboring magnetic moments for antiferromagnets (ferromagnets). For antiferromagnets (ferromagnets), χ is positive and vanishingly small (up to the order of 10^6). In antiferromagnets, at zero field the macroscopic magnetization is near zero and a large external magnetic field is needed to realize full magnetic alignment. In ferromagnets, magnetic domains might be formed. Each magnetic domain features a non-zero macroscopic magnetization. For a random alignment of many magnetic domains the remnant magnetization is zero whereas upon application of external fields, magnetic domains align to the applied field direction. At large fields the system becomes magnetically saturated and $|\mathbf{M}| = M_S$, with M_S defined as saturation magnetization. This parameter is temperature dependent ([129]):

$$M_S(T) = M_S(T=0) \left[1 - a \frac{T^{2/3}}{T_C^{2/3}} \right]. \quad (2.3)$$

a is a constant depending on the short-range exchange interaction and T_C is the Curie temperature. Above this critical value, the ferromagnet becomes a paramagnet.

Ferrimagnetic materials possess neighboring magnetic moments that are anti-parallel. The magnitude of magnetic moments aligned along opposite directions is different hence $\mathbf{M} \neq \mathbf{0}$. Within a specific frequency range, their spin dynamics can be modelled assuming ferromagnetic behavior.

When describing electromagnetic fields in matter the magnetic flux density \mathbf{B} is relevant:

$$\mathbf{B} = \mu_0(\mathbf{M} + \mathbf{H}) = \mu_0(\chi + 1)\mathbf{H} \quad (2.4)$$

Here we assume a scalar susceptibility. The quantity $\mu_0(\chi + 1)$ is the material permeability and $\mu_r = (\chi + 1)$ is the relative permeability.

2.2 Energy terms in micromagnetism

The ground state magnetization of a ferromagnet is determined by the interplay of several interactions. The interactions have different typical length scales and favors different magnetic alignment. By minimizing the total free energy functional the equilibrium configuration is found. In the samples considered in this thesis the micromagnetic approach [12] provides successful physical modelling. The key assumption is that the magnetization is a continuous vector. This means that neighboring magnetic moments change direction by only a small amount. In the following we introduce the relevant energy terms.

2.2.1 Heisenberg exchange energy

This energy contribution comes from a type of interaction acting on short-range and of quantum-mechanical nature. Indeed it can be understood as consequence of Coulomb interaction, Heisenberg's uncertainty principle and Pauli exclusion principle [34]. The exchange energy for an N -electron system is calculated by:

$$E_{\text{ex}} = - \sum_{i < j}^N 2J_{ij} \mathbf{S}_i \cdot \mathbf{S}_j. \quad (2.5)$$

$2J_{ij}$ is the coupling constant and its sign determines ferromagnetic (>0) or antiferromagnetic (<0) alignment of neighboring spins. In the continuum framework E_{ex} can be recast in the form of a volume integral [5]:

$$E_{\text{ex}} = \frac{A_{\text{ex}}}{M_S^2} \int (\nabla \mathbf{M})^2 dV. \quad (2.6)$$

A_{ex} is the exchange stiffness and typical values are of the order of 10 pJ/m. This formulation suggests that exchange energy is large when magnetization is inhomogeneous over short length scales.

2.2.2 Dzyaloshinskii-Moriya interaction

Dzyaloshinskii-Moriya interaction (DMI) is an antisymmetric exchange interaction firstly formulated in Refs. ([11], [10]). In the quantum-mechanical picture, the DMI energy term is:

$$E_{\text{DMI}} = \mathbf{D}_{ij} (\mathbf{S}_i \times \mathbf{S}_j) \quad (2.7)$$

with \mathbf{D}_{ij} being the DM vector. In a continuum model [55] it reads:

$$E_{\text{DMI}} = \int \mathbf{D} \mathbf{M} (\nabla \times \mathbf{M}) dV \quad (2.8)$$

This interaction favors a noncollinear equilibrium state in that neighboring spins are orthogonal to each other. This, in combination with symmetric exchange interaction (eq. 2.5), give rise to spin canting and formation of chiral magnetic textures. With the progress of nanotechnology multilayer systems with thin films combining ferromagnets and heavy metals have been fabricated and investigated. Here, interfacial DMI (iDMI) arises giving origin to non-trivial topological magnetic textures and non-reciprocal magnon propagation ([103], [45] and [40]). iDMI plays an important role in tailoring nonreciprocal dispersion of magnons in ultra thin films.

2.2.3 Zeeman energy

The Zeeman energy describes the interaction of magnetic moments with an external field \mathbf{H}_{ext} following this formula:

$$E_Z = -\mu_0 \int (\mathbf{H}_{\text{ext}} \cdot \mathbf{M}) dV \quad (2.9)$$

Zeeman interaction is such that the system is in equilibrium and minimum energy when its magnetization aligns with the external field \mathbf{H}_{ext} .

2.2.4 Demagnetization energy

An object with magnetization \mathbf{M} generates a magnetic field that is called *stray field* in the region outside the object and *demagnetization field* \mathbf{H}_d inside the object. Considering Maxwell's equation $\nabla \cdot \mathbf{B} = 0$ and Eq.2.4 a discontinuity in the magnetization acts either as a source or sink of magnetic field. \mathbf{H}_d is responsible for the magnetostatic self-energy term and acts on the magnetization:

$$E_d = -(\mu_0/2) \int (\mathbf{H}_d \cdot \mathbf{M}) dV \quad (2.10)$$

The demagnetization field is spatially inhomogeneous and its explicit formulation is often a complicated theoretical task. It can be generally expressed as a function of the magnetization via the demagnetization tensor \vec{N} :

$$\mathbf{H}_d = -\vec{N} \mathbf{M} \quad (2.11)$$

The components of \vec{N} are called demagnetization factors. For uniformly magnetized material in an ellipsoid as all off-diagonal tensor components are zero:

$$N = \begin{pmatrix} N_x & 0 & 0 \\ 0 & N_y & 0 \\ 0 & 0 & N_z \end{pmatrix}. \quad (2.12)$$

It must hold: $N_x + N_y + N_z = 1$. For a thin film where the thickness (along z) is much smaller than the other two in-plane dimensions one can make these approximations $N_x = N_y \approx 0$ and $N_z \approx 1$. The demagnetization effects are often referred to as *shape anisotropy*.

2.2.5 Magnetocrystalline anisotropy

Magnetocrystalline anisotropy (MCA) originates from spin-orbit coupling in that the magnetization prefers to align along specific crystallographic directions thus giving rise to an anisotropy energy terms E_a . Details on MCA can be found in [42]. Py is an alloy that is optimized to avoid MCA. At room temperature Py has also no magnetostriction. MCA is weak in YIG ([35], [91]).

2.2.6 Stoner-Wohlfarth model

We introduce now a model describing coherent magnetization reversal that is based on two energy terms we have introduced. In the Stoner-Wohlfarth model the energy landscape is defined by anisotropy and Zeeman energy. The model describes uniform magnetization rotation in a magnetic system that is single-domain. The energy depends on the angles of magnetization and external field with respect to the easy-axis direction of the magnetic system and can be expressed as:

$$E = KV(\sin \gamma)^2 - M_S V H \cos(\phi - \gamma), \quad (2.13)$$

where K is the anisotropy constant, H is the field magnitude and V is the magnetic volume. Further parameters are γ the angle between the magnetization vector and the easy axis and ϕ the magnetic field angle measured from the easy axis. Magnetization and field are coplanar with the easy axis. Two energy minima are found that are separated by the potential barrier ΔE (Fig. 2.1). The critical switching field (coercive field H_C) is found by simultaneous solving for $\partial E / \partial \phi = 0$ and $\partial^2 E / \partial \phi^2 = 0$ [34]. Figure 2.1b shows the hysteresis curve $M(H)$ with the coercive field for the single-domain particle with H applied along the easy axis.

In Eq. 2.13 we assume that the shape anisotropy provides the uniaxial anisotropy. In case of an ellipsoidal body of revolution, the anisotropy constant is defined as:

$$K = K_{\text{eff}} = \frac{1}{2} M_S^2 (N_x - N_z), \quad (2.14)$$

assuming the magnetic field is directed along the z -axis. Using Eq. 2.14 the total energy (Eq.2.13) is now rewritten as:

$$E = \frac{1}{2} M_S^2 (N_x - N_z) \cdot V \cdot (\sin \gamma)^2 - M_S V H \cos(\phi - \gamma), \quad (2.15)$$

In Fig. 2.1 we illustrate the angular dependence of the total energy for $H = 0$. In Fig. 2.1a two energy minima are observed in the absence of external field. These minima correspond to the two configurations in which the magnetization is collinear with the easy axis (z -axis). The system is called bistable. In Fig. 2.1b the field value at which $M = 0$ is called coercivity field H_C . We will discuss in section 2.10 the modified energy landscape when the external field is non-zero and how this can lead to magnetization reversal in bistable systems.

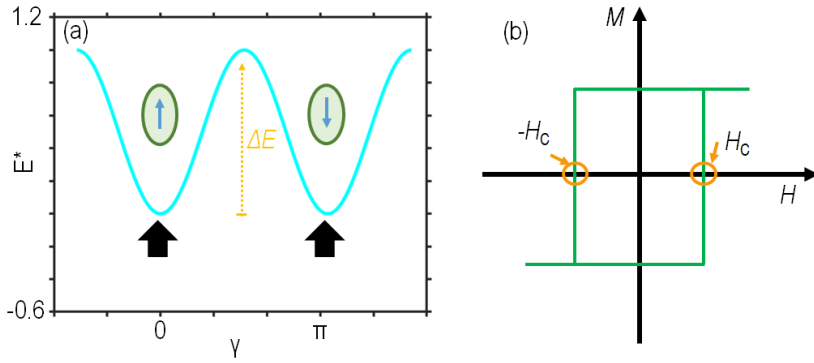


Figure 2.1: The angular dependence of the normalized total energy $E^* = \frac{E}{K_{\text{eff}} V}$ is illustrated in (a) for zero field. The two energy minima are indicated by black arrows. In (b) the hysteresis loop is sketched for coherent magnetization reversal.

2.2.7 Effective magnetic field

The summation of all the energy terms defines the total energy functional $E_{\text{tot}}[\mathbf{M}]$ that is a function of the magnetization \mathbf{M} and its orientation:

$$E_{\text{tot}} = E_{\text{ex}} + E_{\text{DMI}} + E_Z + E_d + E_a. \quad (2.16)$$

The equilibrium magnetization minimizes the energy functional. The total energy density functional E_{tot} is utilized to define an effective magnetic field \mathbf{H}_{eff} :

$$\mathbf{H}_{\text{eff}} = -(1/\mu_0) \frac{dE_{\text{tot}}}{d\mathbf{M}}, \quad (2.17)$$

which enters the Landau-Lifshitz-Gilbert equation discussed in the next section.

2.3 Magnetization dynamics

2.3.1 Landau-Lifshitz-Gilbert equation

In magnetostatics, at equilibrium the magnetization is aligned with the effective field \mathbf{H}_{eff} . To generate a dynamic response of a magnetic body, \mathbf{M} must tilt away from the \mathbf{H}_{eff} direction or vice versa. When these two vectors are not parallel to each other a non-zero torque originates: $\mathbf{T} = \mu_0 \mathbf{m} \times \mathbf{H}_{\text{eff}}$. In classical Newtonian mechanics this determines a time evolution of the angular momentum \mathbf{L} : $\frac{d\mathbf{L}}{dt} = \mathbf{T}$. From Eq. 2.1 magnetic and angular momentum are linked to each other. This allows to write the equation of motion for magnetization dynamics as proposed by Landau and Lifshitz ([3]):

$$\frac{d\mathbf{M}}{dt} = -|\gamma|\mu_0 \mathbf{M} \times \mathbf{H}_{\text{eff}} \quad (2.18)$$

The LL equation (LLE) describes the magnetization precession around its equilibrium direction with angular velocity $\omega_H = |\gamma|\mu_0 H_{\text{eff}}$. This equation lacks of a term describing dissipation. To take into account energy dissipation a damping term, describing a viscous force, was introduced at a later stage by Gilbert [9]. The Landau-Lifshitz-Gilbert equation (LLGE) reads:

$$\frac{d\mathbf{M}}{dt} = -|\gamma|\mu_0 \mathbf{M} \times \mathbf{H}_{\text{eff}} + (\alpha/M_S) \frac{d\mathbf{M}}{dt} \times \mathbf{M}. \quad (2.19)$$

α is named *Gilbert damping* and allows for a phenomenological description of energy dissipation. The LLGE describes the precessional motion of magnetization that over a certain time ($\sim \frac{1}{\alpha\omega_H}$) relaxes to the equilibrium direction. YIG together with hematite ($\alpha - \text{Fe}_2\text{O}_3$) have the lowest Gilbert damping of about $\sim 10^{-5}$. Materials with small damping parameter α are sought after to achieve long magnon lifetime and decay lengths. LLGE can be solved numerically; for the case of small spin precessional angle (linear dynamics) the LLGE can be linearized for analytical solution.

2.4 Ferromagnetic resonance

The LLGE is utilized to describe resonances in a magnetic materials [20]. We start by modelling uniform magnetic precession in that all spins precess with the same phase. This resonant mode is named *ferromagnetic resonance* (FMR) and the corresponding wave vector k is $k_{\text{FMR}} = 0$. It is instructive to neglect at first the damping term and use the LLE. The magnetic field (magnetization) is modelled as sum of a static \mathbf{H}_0 (\mathbf{M}_0) and a dynamic component \mathbf{h}_d (\mathbf{m}_d). In equilibrium $\mathbf{H}_0 \times \mathbf{M}_0 = 0$ holds. We assume small perturbation such that $|\mathbf{H}_0| \gg |\mathbf{h}_d|$ and $|\mathbf{M}_0| \gg |\mathbf{m}_d|$, hence we consider only linear deviations from the equilibrium configuration. The linearized LLE reads:

$$\frac{d\mathbf{m}_d}{dt} = -\gamma\mu_0(\mathbf{m}_d \times \mathbf{H}_0 + \mathbf{M}_0 \times \mathbf{h}_d) \quad (2.20)$$

We adopt complex notation and assume harmonic time dependence for both components \mathbf{m}_d and \mathbf{h}_d obtaining:

$$i\omega\mathbf{m}_d + \gamma\mu_0\mathbf{m}_d \times \mathbf{H}_0 = -\gamma\mu_0\mathbf{M}_0 \times \mathbf{h}_d \quad (2.21)$$

In the linear approximation, dynamic components are non zero only in the plane orthogonal to the equilibrium direction assumed to be the x-direction in the following. The solution to this set of equations is given by $m_{d,x} = 0$, $m_{d,y} = \chi h_{d,y} + i\chi_a h_{d,z}$ and $m_{d,z} = -i\chi_a h_{d,y} + \chi h_{d,z}$. χ and χ_a are the diagonal and off-diagonal components, respectively, of the Polder's susceptibility tensor $\vec{\chi}$:

$$\chi = \frac{\gamma\mu_0 M_0 \omega_H}{\omega_H^2 - \omega^2} \text{ and } \chi_a = \frac{\gamma\mu_0 M_0 \omega}{\omega_H^2 - \omega^2}. \quad (2.22)$$

The dynamic magnetization is given by $\mathbf{m}_d = \vec{\chi} \mathbf{h}_d$ with:

$$\vec{\chi} = \begin{pmatrix} 0 & 0 & 0 \\ 0 & \chi & i\chi_a \\ 0 & -i\chi_a & \chi \end{pmatrix} \quad (2.23)$$

In the ideal lossless case the susceptibility diverges at resonance where $\omega = \omega_H$. In a realistic case, damping must be taken into account and such divergence is avoided. Moreover, the dynamic contribution from the demagnetization field must be included in the mathematical treatment: $\mathbf{h}_{d,\text{dem}} = -\mathbf{N}_d \mathbf{m}_d$. Kittel [4] was first to develop the formalism for FMR in a real sample and arrived at:

$$f_r = \frac{\gamma\mu_0}{2\pi} \sqrt{[H_0 + (N_y - N_x)M_S][H_0 + (N_z - N_x)M_S]} \quad (2.24)$$

For Kittel equation one assumes the external magnetic field at equilibrium is pointing along x. f_r indicates the frequency of the ferromagnetic resonance (FMR). For an ideal thin film $N_y = N_z = 0$ and the resonance is determined by

$$f_r = \frac{\gamma\mu_0}{2\pi} \sqrt{[H_0 + M_S]H_0}, \quad (2.25)$$

assuming the x-direction to be in the plane of the film. Taking into account damping and an actual experimental configuration on thin films where the dynamic external field is along y

the susceptibility components read [20]:

$$\text{Re}(\chi_{yy}) = \frac{\omega_M(\omega_M + \omega_H)(\omega_r^2 - \omega^2)}{(\omega_r^2 - \omega^2)^2 + [(\alpha\omega)(2\omega_H + \omega_M)]^2} \text{ and} \quad (2.26)$$

$$\text{Im}(\chi_{yy}) = \frac{\alpha\omega\omega_M[\omega^2 + (\omega_M + \omega_H)^2]}{(\omega_r^2 - \omega^2)^2 + [(\alpha\omega)(2\omega_H + \omega_M)]^2} \quad (2.27)$$

Figure 2.2 reports the ferromagnetic resonance of a thin film as function of an in-plane mag-

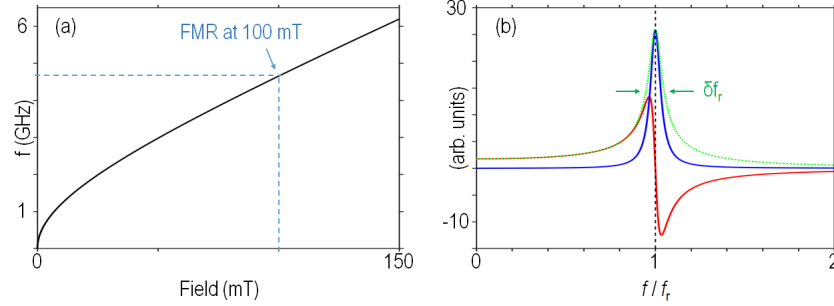


Figure 2.2: (a) Ferromagnetic resonance frequency f_r line as a function of external magnetic field for a thin film ($N_z = 1$). The assumed magnetic parameters are $\mu_0 M_S = 176$ mT, $A_{\text{ex}} = 3.76$ pJ/m, $\alpha = 0.03$, $\gamma/(2\pi) = 28.024$ GHz/T. (b) Real (red), imaginary (blue) and magnitude (green) of the Polder's susceptibility illustrated as a function of the frequency normalized to the resonant value at +100 mT. The black dashed line indicates $f = f_r$.

netic field and the real and imaginary susceptibility components at +100 mT. The imaginary susceptibility reaches its maximum at resonance while the real part crosses the zero point. This indicates a $\pi/2$ phase delay of \mathbf{m}_d with respect to the external driving field \mathbf{h}_d . The linewidth δf_r of $\text{Im}(\chi_{yy})$ is extracted to characterize the Gilbert damping [53]:

$$\delta f_r = \frac{|\gamma|}{2\pi} \mu_0 \delta H + 2\alpha f_r \quad (2.28)$$

with δH being the linewidth broadening ascribed to extrinsic mechanisms and film inhomogeneities.

2.5 Magnon dispersion

We discuss collective spin excitations which reflect spin waves (magnons) with a finite wave vector k . In such cases neighboring precessing spins exhibit a non-zero relative phase shift thus giving rise to the wave-like excitation with finite $k_{\text{tot}} = \sqrt{k^2 + \kappa_n^2}$ and wavelength $\lambda = \frac{2\pi}{k_{\text{tot}}}$. To couple to these excitations the external driving must be spatially inhomogeneous or confined locally. The perturbation in the magnet might propagate due to exchange and dipolar coupling of neighboring spins. Indeed to evaluate the dispersion of non-zero k magnons both dipolar (long-range) and exchange (short-range) interactions are to be taken into account. The mathematical treatment of such modelling has been formulated for thin films by Kalinikos and

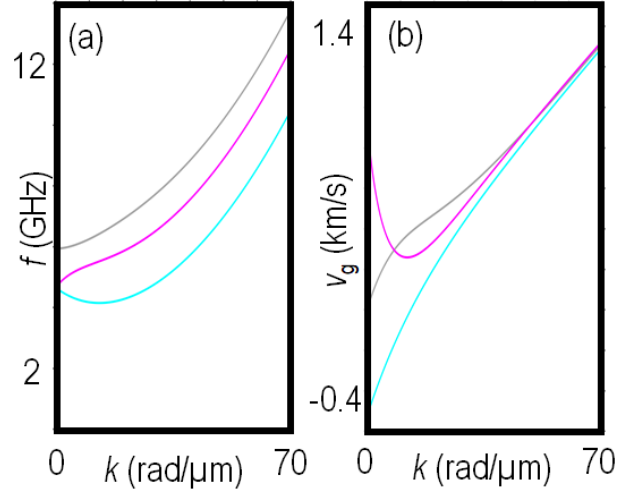


Figure 2.3: (a) Magnon resonant frequencies as a function of in-plane wave vector k for 113-nm-thick YIG corresponding to Damon-Eshbach, DE (magenta) and Backward-volume, BV (cyan) configurations. A field of 100 mT is assumed to exist in the film plane. In grey the magnon dispersion for the case of Damon Eshbach magnons considering quantization across the thickness of the thin film ($DE+PSSWI$). (b) Group velocity for the modes displayed in (a). All data are calculated at 100 mT in-plane field along the x-axis and the in-plane wave vector k is along the y-axis.

Slavin (KS formalism) [16]. In Fig. 2.3 we show the application of this model and present the dispersion relations $f(k_{\text{tot}})$ of magnon modes in 113-nm-thick YIG for 100 mT in-plane field. The magnon wave vector is decomposed in in-plane \mathbf{k} and out-of-plane κ_n components hence the total wave vector magnitude is $k_{\text{tot}} = \sqrt{\kappa_n^2 + k^2}$ by considering the magnon quantization across the thickness hence it holds $\kappa_n = (n\pi/t)$; with $n = 0, 1, 2, \dots$ and t being the thickness. Using $k_{\text{tot}} = \sqrt{k^2 + \kappa_n^2}$ KS formalism models a magnon dispersion relation as follows:

$$\omega(\mathbf{k}_{\text{tot}}, \mathbf{H}) = \sqrt{(\omega_H + \omega_M l_{\text{ex}}^2 k_{\text{tot}}^2)(\omega_H + \omega_M(l_{\text{ex}}^2 k_{\text{tot}}^2 + F_n))} \quad (2.29)$$

with

$$F_n = 1 - P_n(\cos \phi)^2 + \frac{\omega_M P_n(1 - P_n)(\sin \phi)^2}{\omega_H + \omega_M l_{\text{ex}}^2 k_n} \quad (2.30)$$

and

$$P_n = (k/k_n)^2 + \frac{2k^3}{k_n^4 L} [1 - (-1)^n \exp -kt] \frac{1}{1 + \delta_{0n}}. \quad (2.31)$$

Here the exchange length $l_{\text{ex}} = \left(\frac{2A_{\text{ex}}}{\mu_0 M_S^2}\right)^2$ [54]. The magnon group velocity is obtained via:

$$v_g = \partial\omega / \partial k. \quad (2.32)$$

In Fig. 2.3b we show the group velocities of different magnons modes at 100 mT. Magnon properties depend on their propagation direction \mathbf{k} with respect to \mathbf{M}_0 the magnetization direction. Magnon with propagation direction $\hat{k} \perp \hat{M}$ are called Damon-Eshbach (*DE*) magnons whereas we refer to the case $\hat{k} \parallel \hat{M}$ as Backward-Volume (*BV*) mode. In-plane propagating magnons can also be quantized across the thickness therefore $\kappa_n \neq 0$. In Fig. 2.3 (grey curves) we report the case of $\kappa_n = 1$. Due to the nature of dipolar interactions, a magnon dispersion at low k ($l_{\text{ex}} k_{\text{tot}} \ll 1$) is anisotropic hence the orientation of magnon propagation \mathbf{k} with respect to equilibrium magnetization \mathbf{M}_0 determines magnon propagation properties, as one can appreciate comparing the cyan and magenta lines in Fig. 2.3. At large k ($l_{\text{ex}} k_{\text{tot}} \gg 1$) exchange interaction dominates the magnon dispersion and makes it isotropic with $f_r \sim k_{\text{tot}}^2$. The group velocity for DE magnons is positive while in BV at small k we find $v_g < 0$. The group velocity for quantized modes across the thickness starts at 0 km/s at $k = 0$. DE magnons feature the largest group velocity. These are usually preferred for transmission experiments in the range of dipolar SWs. In the presence of dipolar interaction magnon dispersion is anisotropic and this originate non-reciprocal magnon propagation. Such behavior is lost at large k where, in ferromagnets, as the symmetric exchange governs the dynamics. In the presence of antisymmetric exchange such as iDMI non-reciprocal propagation is established in the dipole-exchange dominated as well. In general, non-reciprocity is an interesting feature of magnons with potential applications in the field of wave-based devices operating as isolators, circulators etc. We discuss magnon dispersion in the presence of iDMI in section 2.6.

KS model is used to model confined magnon modes as well. Magnon modes confined along the thickness are called perpendicular standing spin waves (PSSWs). For $\kappa_n \neq 0$ and $k = 0$ the dispersion according to KS formalism can be recasted in a simpler form [90]:

$$\omega_{\text{PSSW},d_s} = \gamma\mu_0 \sqrt{\left(H_0 + \frac{2A_{\text{ex}}}{\mu_0 M_S} \frac{d_s^2 \pi^2}{t^2}\right) \left(H_0 + \frac{2A_{\text{ex}}}{\mu_0 M_S} \frac{d_s^2 \pi^2}{t^2} + M_S\right)} \quad (2.33)$$

Here t is the thickness and d_s counts the number of half oscillations across the thickness. d_s in a real sample can deviate from n as assumed so far. This parameter depends on the spin pinning boundary conditions. d_s is referred to as spin pinning parameter. The spin pinning boundary conditions depend on the spin alignment at the interface. For classical physics often only two options are considered in which a standing wave has either zero or maximum amplitude at a boundary. Interestingly for a spin wave the amplitude can take intermediate values at the boundary as well [16]. When comparing the KS formalism to data obtained on a sample, d_s is used to fit the calculated dispersion relation to the measured resonance frequencies.

2.6 Magnon dispersion in the presence of iDMI

The iDMI adds a linear term in k to the dispersion and the new resonance frequency as a function of H and k reads [114] [58]:

$$\omega_{\text{tot}}(\mathbf{k}_{\text{tot}}, \mathbf{H}) = \omega_0(\mathbf{k}_{\text{tot}}, \mathbf{H}) + \frac{2\gamma D}{M_S} [(\hat{n} \times \hat{M}) \cdot \mathbf{k}] \quad (2.34)$$

with $\omega_0(\mathbf{k}_n, \mathbf{H})$ being the magnon dispersion according to KS model (Eq. 2.29). D is the iDMI strength, \hat{n} the symmetry breaking direction (e.g. the growth direction in case of multilayers), \mathbf{k} the magnon wave vector and $\hat{M} = \mathbf{M}/M_S$. The second term can be either positive or negative. This depends on the direction of the magnetization and magnon propagation with respect to the symmetry breaking axis. For thin films, this formula suggests the contribution to iDMI is zero when the magnetization points out-of-plane (i.e. $|\hat{n} \times \hat{M}| = 0$). For in-plane fixed field, magnons possessing the same k feature different frequencies according to their in-plane propagation direction or in other words this effect is anisotropic in the plane as it depends on the angle between the magnetization and the wave vector. The frequency difference between counterpropagating magnons occurs when $\mathbf{k} \perp \mathbf{M}$. The group velocity is modified by the iDMI. Denoting $v_{g,0}$ the group velocity expressed by the KS model in Eq. 2.32 the group velocity with iDMI contribution reads:

$$v_{g,\text{tot}} = v_{g,0} + v_{g,\text{DMI}} \quad (2.35)$$

$$\text{with } v_{g,\text{DMI}} = \frac{2\gamma D}{M_S} [(\hat{n} \times \hat{M}) \cdot \hat{k}] \quad (2.36)$$

The second term $v_{g,\text{DMI}}$ is constant while its sign depends on the magnon wave vector direction. The second term is the iDMI-induced velocity term [58].

By measuring the frequency difference δf_{\pm} of counterpropagating magnons one can deduce the iDMI strength using:

$$\delta f_{\pm} = 2 \frac{\gamma D}{\pi M_S} |\mathbf{k}|. \quad (2.37)$$

As an alternative approach, the group velocity asymmetry δv_g can be extracted by transmission measurements and then the iDMI strength can be estimated. δv_g measures the group velocity difference between the slow ($v_{r\text{mg},-}$) and fast ($v_{r\text{mg},+}$) propagating direction of the same magnon mode in the presence of iDMI. δv_g is expressed as:

$$\delta v_g = |v_{g,+} - v_{g,-}| = \frac{4\gamma D}{\pi M_S}. \quad (2.38)$$

Recently, an empirical model has been adopted to explain the magnetic field dependent group velocity asymmetry observed in 7-nm-thick YIG [114]:

$$\delta v_g = 2v_{g,\text{DMI}} \cdot \arctan(H/H_0). \quad (2.39)$$

Equation 2.39 explained the observed behavior in that the group velocity asymmetry reached an asymptotic value for a magnetic field with a magnitude larger than a critical threshold H_0 .

2.7 Magnonic crystals (MCs)

Magnonic crystals are created by magnetic materials possessing periodic modulation of different constituents or specific parameters (e.g. A_{ex} , M_S or other parameters, local magnetic fields, strain, temperature). Magnon dispersion relation $\omega(\mathbf{k}, \mathbf{H})$ in these systems feature engineered band gaps and minibands [63]. Analogously to the case of electron states in the periodic crystal potential and electronic band structure, for MCs we can apply a formalism based on Bloch's theorem. The spatially modulated magnetic moment can be expressed as a Bloch wave $\mathbf{m} = \exp(i\mathbf{k} \cdot \mathbf{r}) \mathbf{u}_{\mathbf{k}}(\mathbf{r})$ where the position vector is $\mathbf{r} = (x, y, z)$ and $\mathbf{u}_{\mathbf{k}}(\mathbf{r})$ possess the same translational invariance as that of the MC, hence it holds $\mathbf{u}_{\mathbf{k}}(\mathbf{r}) = \mathbf{u}_{\mathbf{k}}(\mathbf{r} + \mathbf{R})$. \mathbf{R} is the crystal period. By adopting Fourier formalism the Bloch wave can be recasted as:

$$\mathbf{m}(\mathbf{r}) = \sum_{\mathbf{G}} \mathbf{m}_{\mathbf{k}}(\mathbf{G}) \exp[i\mathbf{r} \cdot (\mathbf{G} + \mathbf{k})] \quad (2.40)$$

with \mathbf{G} indicating the reciprocal lattice vectors that must fulfill the condition $\mathbf{G} \cdot \mathbf{R} = 2\pi N$ with $N \in \mathbb{Z}$ and \mathbf{k} is a wave vector belonging to the first Brillouin zone (BZ1). The BZ is defined by the MC periodicity; assuming a one-dimensional MC with lattice constant p the boundaries of BZ1 coincide with $k_{\text{BZ1}, \pm} = \frac{\pm\pi}{p}$. For a fixed k_{BZ} inside the BZ1 the dispersion features several solutions $f_q(k)$ that are identified by their miniband number $q \in \mathbb{N}$. Depending on the strength of the periodic modulation band gaps are opened. The modulation strength determines the band gap width. The exact solution $f_q(k)$ can be analytically evaluated by the plane wave method ([41], [22]). In our work we model magnon dispersions in periodic structures by numerically solving the LLGE. In this scenario, the allowed magnon states are formed by coherent Bragg scattering at the periodic potential and constructive interference.

2.8 The magnonic grating coupler effect

We have discussed that 1D MCs possess eigenstates with wavevectors $\mathbf{k} = \mathbf{k}_{\text{BZ}} + q\mathbf{G}$ where $q = 0, \pm 1, \pm 2, \pm 3, \dots$ and $|\mathbf{G}| = \frac{2\pi}{p}$ such that their magnitude behaves $\sim \frac{|q|}{p}$ for large $|q|$. MCs are artificially tailored to control magnon phase, energy and velocity. MCs belong to the metamaterial systems where quasiparticle dispersion can be engineered. In photonics and plasmonics it has been shown that periodic patterning provides wave matching thus enhancing the coupling between two different wave guiding media [93]. Though similar to the periodic artificial crystals such functional transducer elements are named grating couplers. Grating couplers (GCs) are periodic systems designed particularly such that dispersion branches are back-folded to the Γ point at $k = 0$. For magnonic GCs established in 2013 [60] the magnon bandstructures were backfolded. At the crossing points given by $\mathbf{k} = \mathbf{k}_1 + q\mathbf{G}$, enhanced microwave-to-magnon transduction was observed. The corresponding GC modes were observed in 1D and 2D grat-

ings [60], [78]. Following Bloch's theorem, the magnonic grating coupler excites magnons with a wavelength $\lambda = q \cdot 2\pi/p$. The excitation of exchange-dominated magnons requires miniaturization of GCs by reducing p .

Utilizing the Co stripes acting as GC on top of a YIG thin film, magnons with a wavelength $\lambda = 50$ nm have been excited and detected [89]. This defines the current state-of-the-art for short-waved magnon excitation using the magnonic grating coupler effect[125]. For nanomagnonics state-of-the-art top-down nanopatterning at the sub-100-nm lateral length scale is needed. Techniques have been developed relying on high-energy photon illumination and synchrotron-based equipments. However these techniques are very expensive, require large facilities and are not commonly available. Another route is possible via bottom-up nanotechnology. We investigate in this thesis the integration of DNA nanotechnology into nanomagnetism as nanopatterning tool to engineer magnetic nanostructures at lateral length scales even below state-of-the-art conventional lithography. In section 3.5 we introduce the main concepts of DNA nanotechnology and describe our research methodology on how to exploit DNA nanotechnology to progress towards sub-100-nm lateral patterning in nanomagnonics.

It has been demonstrated that a surface corrugation δ of 2 nm in a ferromagnet leads to the backfolding of branches, formation of bandgaps and minibands for magnons [85]. We highlight in Fig. 2.4 selected results from this work. In Fig. 2.4a the DE dispersion relation of the plane film is shown. Figure 2.4b displays the same film but with $\delta = 2$ nm and a periodicity of surface corrugation of $a_z = 300$ nm. The boundaries of the first Brillouin zone (BZ1) are $|k_{\text{BZ1}}| = \frac{\pi}{a_z} = 10.5$ rad/ μm . This value is still below the exchange-dominated range of wave vectors according to the KS model [16]. This value δ is encouraging for our DNA based nanotechnology introducing a similar corrugation.

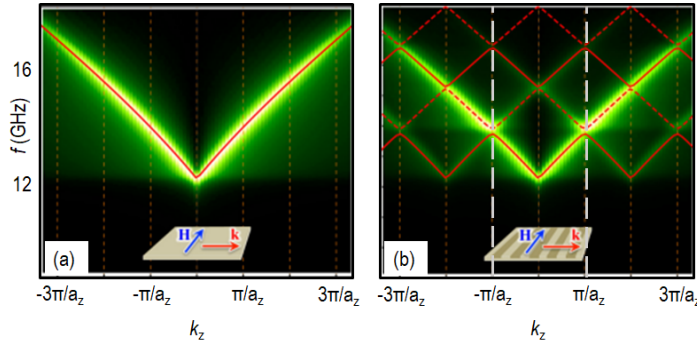


Figure 2.4: (a) and (b) are adapted from [85]. The magnon band structure for Damon-Eshbach propagation is reported for (a) a plain film and for (b) a surface corrugated thin film. The authors have assumed the magnetic parameters of permalloy. The applied field is 150 mT. (b) The grey dashed lines defines the BZ1 boundaries.

2.9 Magnon-magnon cooperativity

For (quantum) information processing the ability to tune and control quasiparticles' interaction and interconversion processes is of fundamental importance (Fig. 2.5). Large efforts are directed to understand how to prepare and optimize physical systems to achieve e.g. strong magnon-magnon, magnon-photon and magnon-phonon coupling [95]. Several studies have addressed magnon-magnon coupling in magnetic hybrid bilayers achieving strong coupling and cooperativity tunability by controlling magnetization alignment and interfacial interactions [83].

The figure of merit of magnon-magnon coupling is the cooperativity C [67]:

$$C = \frac{g^2}{\kappa_{m1}\kappa_{m2}} \quad (2.41)$$

with g quantifying the coupling strength and κ_{m1} and κ_{m2} representing the half widths at half maximum of the resonances of the isolated magnon modes. C counts the oscillations of the hybridized mode before decoherence settles in [132]. Depending on κ_{m1} , κ_{m2} and g different coupling regimes are identified (Fig. 2.5). Magnon-magnon coupling has been probed in

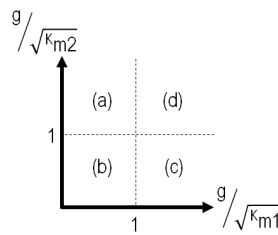


Figure 2.5: Sketch of different scenarios of quasiparticles' coupling inspired by [67]. Depending on the ratio of the coupling strength and the dissipation rates of the two modes one classifies the coupling as (a) magnetically induced transparency, (b) weak coupling, (c) Purcell effect and (d) strong coupling.

artificial magnetic crystals on ferromagnetic layer. The influence of external fields and shape has been characterized [137]. In this thesis we explore magnon-magnon coupling by inductive broadband spectroscopy performed on 11-nm-thick YIG with integrated one-dimensional periodic arrays of Py nanostripes.

2.10 Angular momentum transfer and magnetization switching

Achieving energy-efficient control of the local magnetization is key for the functionality of spintronic and magnonic devices. In particular, the ability of writing/reading magnetic bits via magnons without the need for conversion to the electrical domain is of great interest as this feature could boost an all-magnon-based on-chip information processing and storage platform. In this paragraph we review relevant literature on mechanisms of angular momentum

transfer that can trigger magnetization switching.

Spin torques by s - d exchange coupling and spin-orbit coupling

In this part we introduce mechanisms based on *spin transfer torque* (STT) and *spin-orbit torque* (SOT). Detailed insights can be found in [100] and [72]. The basic scenario of spin torques is the interaction between spin polarized electron flow and localized magnetic moments due to angular momentum conservation. The interaction was first explained with s - d exchange coupling and the *spin transfer effect*, (ST effect). Slonczewski [21] predicted that magnetization can be reversed by the ST effect and later Berger, independently, predicted magnetization precession via ST effect [19]. For the case of *spin orbit torque* (SOT), the current-induced torque occurs via charge-to-spin conversion governed by spin-orbit coupling (SOC) of a single material or in a heterostructure [124]. Here a non-zero electric field creates nonequilibrium orbital occupation that via SOC leads to SOT. Different microscopic mechanisms drive SOT, e.g. Spin Hall effect, orbital Hall effect and Rashba effect are the most widely investigated. However, recent works have investigated thermally-generated, phonon- and magnon-driven SOTs. We refer to STT when the electrical current flows across the interface of different materials and to SOT when the electrical current flows in the plane parallel to the interface. To describe current-induced torques we consider the typical trilayer structure made of ferromagnet (FM1)/normal metal (NM)/ferromagnet (FM2). In our discussion FM1 is the free layer to which we aim to transfer momentum and/or switch magnetization \mathbf{M}_1 . FM2 is the reference layer with magnetization \mathbf{M}_2 . FM2 defines the spin polarization. Due to its mathematical form the Slonczewski STT is also often referred to as *damping-like torque* τ_{DL} (refer to Eq. 2.19 for comparison with damping term). A common expression for current-induced torques is ([100]):

$$\tau_{el} = \tau_{FL} \hat{M} \times \hat{\xi} + \tau_{DL} \hat{M} \times (\hat{M} \times \hat{\xi}). \quad (2.42)$$

The first term is called field-like, FL, torque and the second term is the damping-like, DL, (i.e. Slonczewski-like) torque. τ_{FL} and τ_{DL} are respectively the magnitude of the FL and DL torque. The quantity $\hat{\xi}$ is a unit vector directed along the incident spin orientation. Electron spin tunnelling is another mechanism that can induce SOT. This occurs for tunnelling barrier layers with a thickness less than 2 nm [117], [66].

Magnon transfer torque

Angular momentum flow carried by precessing spins provides a magnon spin current $\mathbf{J}_{m,s}$ [68]. $\mathbf{J}_{m,s}$ has the following key advantages in comparison to the electronic spin current $\mathbf{J}_{e,s}$: energy dissipation is reduced due to the absence of Joule heating as no electron motion is involved and transmission in insulators becomes possible with long decay length [82] (and references therein). Recently magnon-torque-induced magnetization switching has been experimentally investigated at zero external magnetic field [104]. Using a trilayer structure consisting of a high spin current source substrate, a NiO spacer and the ferromagnet Py the electrical spin current was converted to magnon spin current at the interface with NiO. NiO features different magnetic phases depending on its thickness. As an insulator only magnons can carry

spin angular momentum across its thickness. The authors observed current-dependent reversal of the Py and attributed this observation to magnon transfer torque. Further studies of magnetization switching by magnon transfer torque were conducted on perpendicularly magnetized garnet thin films [117], [121]. In Ref. [104] the authors proved that direct exchange coupling is not essential for magnon-torque-induced magnetization switching.

Thermomagnonic torque

Angular momentum transfer can be initiated and/or assisted by thermal fluctuations. In 2010 Slonczewski proposed magnonic STT induced by heat flowing through the interface of a ferrite/NM/free magnet system. The ferrite provides thermally-generated magnon spin current. The mechanism requires large s-d exchange coupling such that the magnon spin current can then be converted in the normal metal to conduction electron current. This can then travel to the interface with the free magnet and here the spin accumulation can be large enough to create sizeable torques [46]. Overall, a more efficient method than electrical STT for switching was predicted.

Spin pumping

Spin pumping (SP) is related to STT by the Onsager reciprocity [43]. SP defines the generation of a spin current by the precessing magnetization of a magnet. In a multilayer FM/NM system the precessing magnetization in the ferromagnet loses torque by emitting spin current into the NM thus acting as a *spin pump*. Spin pumping depends on the interfacial coupling and interface quality. The physical quantity that takes this into account is so-called interfacial mixing conductance $g^{\uparrow\downarrow} = g_r^{\uparrow\downarrow} + i g_i^{\uparrow\downarrow}$, with $g_r^{\uparrow\downarrow}$ ($g_i^{\uparrow\downarrow}$) being the real (imaginary) part [24]. $g^{\uparrow\downarrow}$ is key for the SP mechanism and also known as *spin mixing conductance*. Via SP the magnetization dynamics of a magnet can inject spin current into an adjacent material. In case of an NM as adjacent material the spin current can travel across the NM thickness provided its thickness is smaller than its spin diffusion length. From SP, spin torques can originate that modify magnetization vector and dynamics. It has been predicted that SP renormalizes the gyromagnetic ratio and Gilbert damping [26]. The former effect is proportional to $g_i^{\uparrow\downarrow}$ whereas the latter grows with $g_r^{\uparrow\downarrow}$. The SP-induced damping enhancement is reflected in the resonance linewidth [70]. For realistic FM/NM interfaces it is often assumed $g_i^{\uparrow\downarrow}$ being vanishingly small hence $g^{\uparrow\downarrow} \approx g_r^{\uparrow\downarrow}$ [27], [26].

Microwave assisted switching

Resonant microwave assisted switching (MAS) was first demonstrated by Thirion et al. in 2003 [29]. They investigated dynamics of magnetization reversal in a 20-nm-diameter Co particle. The system was a single-domain magnet hence its reversal dynamics was governed by the Stoner-Wohlfarth model (section 2.2.6). As such the only competition was between shape anisotropy field and applied external field. The authors applied an external magnetic below the coercive field H_C threshold for quasistatic switching. This favored one magnetization direction in the ground state (blue arrow in Fig. 2.6) while the opposite direction formed the metastable state (red arrow in Fig. 2.6). Upon irradiation with RF pulses that hit the FMR frequency (Eq. 2.24) the magnetization precessed and for large pulses the nanoparticle left the

metastable state jumped to its stable ground state (Fig. 2.6). The reversal thus achieved was called MAS.

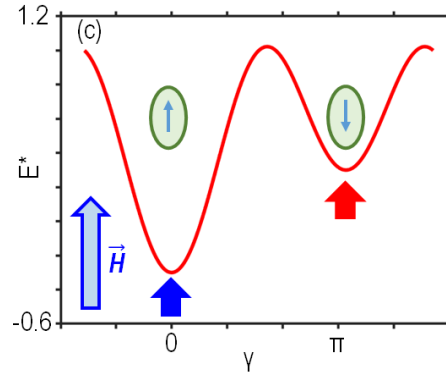


Figure 2.6: The normalized total energy E^* is reported for $H = 0.5H_K$ as a function of γ . $H_K = \frac{2K_{\text{eff}}}{\mu_0 M_S}$ represents the anisotropy field. The blue (red) arrow indicates the stable (metastable) state. The field is applied along the direction that favors the alignment indicated by the blue arrow. The $H = 0$ case is shown in Fig. 2.1.

Reversal by domain wall motion

Magnetization reversal can occur via nucleation and propagation of magnetic domains. This implies the formation and propagation of domain walls. The nucleation of a domain is triggered by DL and/or FL torques. This can be assisted by DMI. Once the domain is nucleated further application of DL torque expands or shrinks the size of the size thus moving the domain wall (DW). Therefore, via DW motion, the newly nucleated domain can extend to the whole magnetic body thus completing magnetization reversal [130]. For magnetic nanowires it has been demonstrated both theoretically and experimentally that propagating magnons exerted enough torque to depin a DW and initiate its motion [81], [50].

3 Methods

3.1 Micromagnetic simulations

We solve the LLG equation (Eq. 2.19) numerically to interpret the experimental data and make predictions concerning the magnon bandstructure modification through nanopatterning of e.g. YIG and Py. To conduct such micromagnetic modelling we use the MuMax3 solver that is a GPU-accelerated micromagnetic solver based on finite difference analysis [65]. With this software and with a postprocessing MATLAB code that we wrote, we model the magnon band structures of the system of different samples (see section 4.3.4).

We first present a MuMax3 simulation to solve the LLG equation (Eq. 2.19) at $T = 0$ K assuming parameters for Py such as $M_s = 800$ kA/m and $A_{\text{ex}} = 13$ pJ/m. The Gilbert damping is set to $\alpha = 10^{-8}$. We are interested on the formation of magnonic crystal with tailored band structure and not on magnon propagation and decay. To obtain well defined minibands and frequency gaps we chose such a small α . The system extends over 9720 nm along x and 31.2 nm along y . The thickness t (along z) is varied (Fig. 3.1). The cell size is 3 nm, 2.08 nm and 1 nm in x -, y -, and z -direction respectively. The field is applied along $+y$ and magnon propagation along x is investigated.

We model a surface corrugated thin film by decomposing it, along the thickness axis, in three main regions namely (i) a dot lattice, (ii) a plain film and an (iii) antidot lattice (Fig. 3.1). Periodic boundary conditions are applied along x and y . The field is 90 mT and directed along $+\hat{y}$. Magnetization is initialized in a uniform state along $+\hat{y}$, the system is relaxed and the equilibrium magnetization vector $\hat{m}_0(\mathbf{r}) = \mathbf{M}_0(\mathbf{r}, t) / M_s$ of each unit vector. To excite magnetization dynamics the following time- and space-dependent magnetic field, with amplitude A and cutoff frequency f_C , is applied:

$$h_p(\mathbf{r}, t) = \begin{cases} (\hat{x} + \hat{z})A \cdot \text{sinc}(2\pi f_C(t - t_d)) & \text{if } |x| \leq 10.5 \text{ nm} \\ 0 & \text{if } |x| > 10.5 \text{ nm} \end{cases}$$

Here t_d defines the time instant at which the magnetic pulse reaches its maximum value. In

our study, unless else specified, we use the following parameter values: $f_C = 100$ GHz, $A = 1$ mT, sampling time $t_s = 5$ ps, $t_d = 10 \times 5$ ps and a total simulation time $t_{\text{tot}} = 4096 \times 5$ ps. During the dynamic simulation the magnetization vector $\hat{m}(\mathbf{r}, t) = \mathbf{M}(\mathbf{r}, t) / M_S$ is recorded at each multiple of t_s . We remove the static magnetic contribution by defining the dynamic magnetization unit vector $\hat{m}_d(\mathbf{r}, t) = \hat{m}(\mathbf{r}, t) - \hat{m}_0(\mathbf{r})$. The z-component $m_{d,z}(\mathbf{r}, t)$ is considered for further analysis. This is multiplied by the Hanning window. Then the 2D FFT $\varphi(k_x, y, z, f) = \text{FFT}[m_{d,z}(x, y, z, t)]$ is computed. The Fourier analysis is applied to the time coordinate and the x coordinate. This process is applied separately for each thickness layer. After the FFT calculation, the power spectral density (PSD) $20 \cdot \log_{10}[|\tilde{m}_{d,z}(k_x, y = 0, z = t/2, f)|]$ is reported as a function of the propagation wave vector k_x and frequency f . Such data provide the band structure with characteristic band gaps in case of periodically modulated properties.

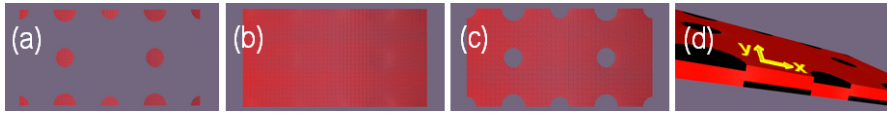


Figure 3.1: (a-c) Images taken with Muview [142] of layers composing the simulated geometry. (a) Dot lattice, (b) plain film and (c) antidot lattice corresponding to different layers of the final geometry that is shown in (d). (d) The red regions are magnetic material and the black zones are void. The system in (d) is used to model surface corrugated thin-film Py as deposited on a periodic DNA lattice.

3.2 All-electrical spin wave spectroscopy (AESWS)

3.2.1 General aspects of inductive broadband spectroscopy

AESWS is an inductive technique for RF broadband analysis of standing and propagating magnons. An electromagnetic (EM) signal oscillating at a frequency f is sent by the Vector Network Analyzer (VNA) to the device under test (DUT). Typically our DUT is made of on-chip integrated coplanar waveguides (CPW1 and CPW2) fabricated on a magnetic layer (YIG in our case). CPWs are fabricated to achieve 50Ω impedance matching so as to transfer efficiently electromagnetic waves to/from conventional RF circuits working up to 26.5 GHz (the maximum probed frequency by our VNA). The CPW geometry defines the space-dependence of the generated inhomogeneous field which consequently defines a specific FFT spectrum. The maxima of the FFT spectrum indicate which wave vector the CPW can efficiently transfer into the spin system (i.e. the underlying magnetic layer) as shown in Fig. 3.3. Coupling RF signals to large- k magnons is made possible by integrating periodic arrays of nanomagnets between the CPW and the YIG (see section 2.8). With such an approach the state-of-the-art AESWS methodology has achieved detection of magnons with $k = 135 \text{ rad}/\mu\text{m}$ [125]. The DUT response in frequency-domain is characterized by measuring its scattering S matrix (Fig. 3.2). A complex voltage signal a_1 is provided to port 1, the instrument measures magnitude, phase, real and imaginary part of the transmitted (reflected) signal b_2 (a_2). The S parameters are

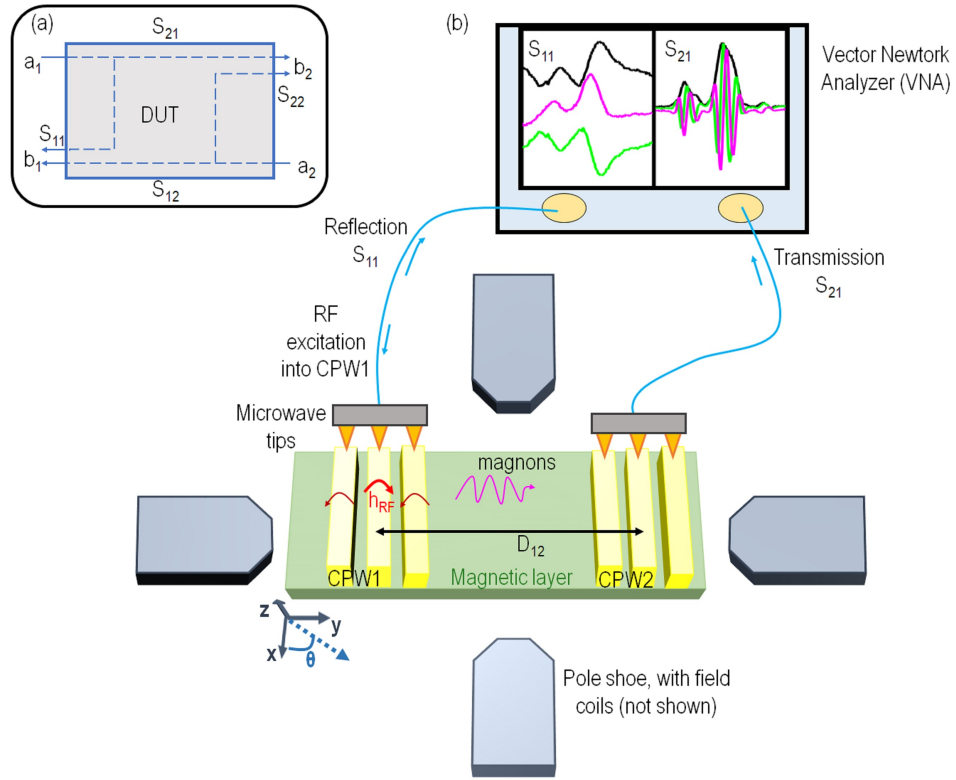


Figure 3.2: (a) Sketch of S parameters used for a 2-port VNA. (b) The VNA is in electrical contact with CPW1 and CPW2 via microwave tips. The RF excitation is injected into CPW1 thus generating an inhomogeneous microwave field. This excites magnons that can propagate to reach CPW2. Here, they are detected by Lenz’s law of induction as transmission signal S_{21} . Besides, the injected electromagnetic power at CPW1 features an absorption peak when hitting a magnon resonance. In the VNA screen magnitude (black), imaginary part (green) and real part (magenta) of S_{11} and S_{21} are shown as insets for the first GC resonance (4.75 ÷ 5.3 GHz range). The magnetic field is externally controlled via pole shoe and field coils which are operated by bipolar voltage suppliers. The setup covers magnetic fields in the range ± 90 mT at any in-plane angle θ .

defined as follows:

$$S_{ij} = \frac{b_i}{a_j}. \tag{3.1}$$

They are unitless complex variables. They describe the *global* response of the DUT. The instrument can be configured in two operation modes that we call (i) asymmetric and (ii) symmetric jumper configuration. In the asymmetric jumper configuration the instrument is configured to efficiently emit from one port 1 (2) and detect at port 2 (1). In the symmetric configuration the instrument emits and detects signals with equal efficiency using both ports 1 and 2.

Measurements are repeated while sweeping the magnetic field magnitude (direction) in order

to obtain field-dependent (angle-dependent) spectra. The magnetic field is applied via pole shoes wound with field coils. The magnetic field control is achieved by a home-built software. The magnetic field is bipolar. An Hall sensor, mounted below the sample stage, monitors and sends a feedback signal reflecting the locally sensed external field. The whole VNA setup is mounted on a vibration isolation table (not shown in Fig. 3.2b).

3.2.2 Coplanar waveguide design and excitation spectrum

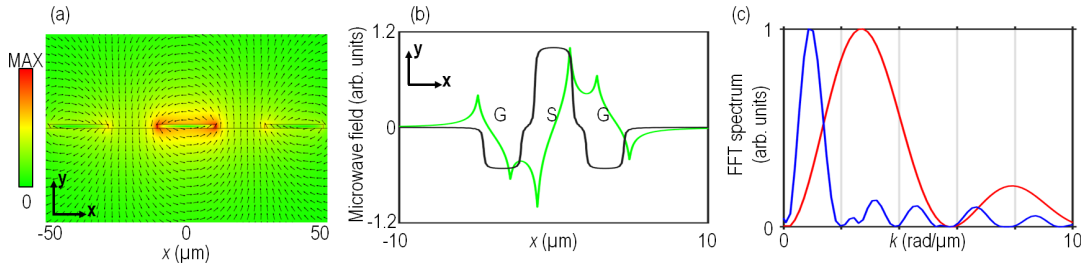


Figure 3.3: (a) COMSOL simulation of magnetic flux density magnitude when i_{rf} at 5 GHz is injected inside the waveguide. The RF current is applied along $-\hat{z}$. The color scale indicates the field magnitude and the black arrows show the field direction in space. The arrow length is normalized by the amplitude for sake of better visibility. (b) Space-dependent evolution of in-plane (out-of-plane) microwave field component is shown in black (green). The ground (G) and signal (S) lines' cross section is illustrated to match the field's space-dependence to the CPW position. (c) FFT spectra of the microwave field for a CPW with w_s (w_g) = 2.1 μm (1.4 μm) in blue and with w_s (w_g) = 0.6 μm (0.4 μm) in red.

The CPW design can be optimized and validated by means of a three-dimensional electromagnetic simulator. A detailed treatment of the analytical relationship between the characteristic impedance Z_0 of an electronic component to its material and geometrical parameters is found in [18]. The CPW geometry we adopt for our research is taken after [115], [59], [48]. The CPW design length is 121.6 μm hence much shorter than the wavelength of the EM wave for the relevant frequency GHz regime. We assume therefore the RF current i_{rf} and the RF magnetic field \mathbf{h}_{rf} to be constant along \hat{z} (Fig. 3.2). However, \mathbf{h}_{rf} is inhomogeneous in the xy -plane. The injected i_{rf} oscillates at a frequency f and propagates along \hat{x} . It goes through the signal line (S) and given the SHORT-type geometry of the CPW splits into two components collected back by the ground (G) pads. S and G line widths are $w_s = w_g = 2.1 \mu\text{m}$ and the separation gap between G and S lines is $w_g = 1.4 \mu\text{m}$. The CPW design is such that the EM cross-talk between neighboring antennas is minimized. COMSOL simulations are conducted for different CPW geometries to extract the CPW excitation spectrum (Fig. 3.3c). The in-plane microwave field component is strongest at the center of the signal line whereas the out-of-plane component is strongest near its edges (Fig. 3.3c). The inhomogeneous field excites magnons with defined

wave vectors. The induced voltage by a propagating magnon below a CPW is given by

$$V_i = \frac{d\Phi_{\text{CPW}}}{dt} = \frac{\mu_0}{2} \int_{V_s} \mathbf{h}_{\text{rf}} \cdot \frac{d\mathbf{M}}{dt} dV \quad (3.2)$$

With V_s being the sample volume, Φ_{CPW} the magnetic flux beneath the CPW and \mathbf{M} the sample magnetization and $\frac{d\mathbf{M}}{dt}$ being expressed as

$$\frac{d\mathbf{M}}{dt} = i\omega\mathbf{m} \exp i(\omega t - \mathbf{k} \cdot \mathbf{r}) \quad (3.3)$$

In this formalism, magnons propagating along x -direction lead to a signal $V_i \sim \int \mathbf{h}_{\text{rf}}(x) \exp ik_x x$, i.e. the Fourier transform of the microwave field along the x -direction. For the CPW geometry that we use, in the FFT spectrum of the microwave field we find the main k peak at $k_1 = 0.86 \text{ rad}/\mu\text{m}$. At higher wave vectors we observe several other peaks with smaller intensity. These wave vectors can also excite magnons though with lower efficiency than k_1 . In general, $k_1 \sim (w_s + w_g)^{-1}$ [37]. Hence by reducing w_s and/or w_g , k_1 can be made larger. However impedance matching for antennas with miniaturized dimensions is challenging. This provides further motivation to our efforts to integrate DNA nanotechnology into nanomagnonics fabrication processes as a patterning tool to achieve miniaturized grating couplers to push microwave-to-magnon transducers beyond the state-of-the-art.

3.2.3 Group velocity and amplitude non-reciprocity

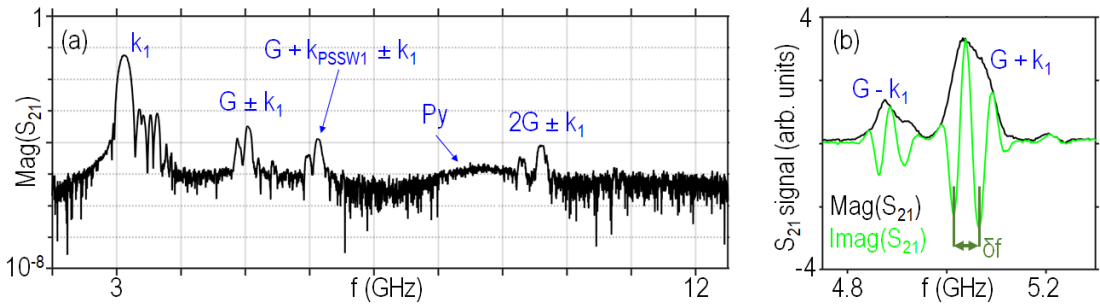


Figure 3.4: (a) $\text{Mag}(S_{21})$ in log-scale at +40 mT measured at $P_{\text{irr}} = -15 \text{ dBm}$ for a device with Py/SiO₂/YIG interface. Main resonances are indicated with the corresponding magnon wave vector (blue labels). (b) Linear scale plot of $\text{Mag}(S_{21})$ [$\text{Imag}(S_{21})$] in black [green]. The noise level is at $\approx -50 \text{ dB}$

Magnon excitation via CPWs possesses a k distribution as shown in Fig. 3.3c. Therefore the resonance peak features a frequency broadening according to the magnon dispersion relation $f = f(\mathbf{k})$. Figure 3.4 shows the scattering parameter S_{21} at +40 mT. S_{21} is measured with CPWs integrated on 113 nm thick YIG. The signal line width is $w_s = 2.1 \mu\text{m}$, while the signal-to-

ground separation is $w_g = 1.4 \mu\text{m}$. Underneath the CPWs Py stripes are fabricated and act as magnonic grating couplers. The stripes are 100 nm wide and 20 nm thick. The periodicity of the stripe array is $p = 200 \text{ nm}$. The Py stripes are separated from the YIG by 5-nm-thick SiO_2 . In Fig. 3.4 many peaks are seen. The first broad one reflects the pronounced k distribution around k_1 . The further peaks are attributed to magnon modes in YIG with wave vectors such as $\mathbf{G} \pm \mathbf{k}_1$, $\mathbf{G} + \mathbf{k}_1 + \mathbf{k}_{\text{PSSW1}}$, $2\mathbf{G} \pm \mathbf{k}_1$. The broad peak around 6.7 GHz is related to the FMR in the Py stripes forming the GC. $\mathbf{k}_{\text{PSSW1}}$ corresponds to κ_1 of the KS model (section 2.5). In (b) the linear magnitude and imaginary part of the transmitted signal between 4.8 and 5.2 GHz is shown. The imaginary part features signal oscillations. These oscillations are indicative of a frequency-dependent phase accumulation φ by the magnon packet as it travels away from the emission point [62]:

$$\varphi = k \cdot d_{\text{eff}} \quad (3.4)$$

where d_{eff} , the effective travelled distance for phase accumulation, is often approximated to D_{12} (Fig. 3.2). Therefore a full period in the measured oscillatory signal of the imaginary part (Fig. 3.4b) represents a wave vector shift $\delta k = 2\pi/d_{\text{eff}}$. The corresponding frequency shift δf is extracted from the data as in Fig. 3.4. We estimate the group velocity v_g according to:

$$v_g = \frac{d\omega}{dk} \approx \frac{2\pi\delta f}{\delta k} = \delta f \cdot d_{\text{eff}}. \quad (3.5)$$

To characterize non-reciprocity of magnons propagating in different directions (section 4.2.3) we define the parameter η that it measures the asymmetry of magnon amplitude A for magnons bearing opposite \mathbf{k} [126]:

$$\eta = \frac{A_{\mathbf{k}}^{12} - A_{\mathbf{k}}^{21}}{A_{\mathbf{k}}^{12} + A_{\mathbf{k}}^{21}}. \quad (3.6)$$

For a constant field, the transmission is measured once sending input signal at port 1 and detecting the response at port 2 (i.e. $S_{\mathbf{k}}^{21}$). In a second measurement cycle port 2 emits the RF signal while port 1 detects it thus detecting $S_{\mathbf{k}}^{12}$. To extract A we fit a Lorentzian to the signals $\text{Mag}(S_{12})$ and $\text{Mag}(S_{21})$. We use the fitted amplitude of the curve to calculate η based on Eq. 3.6.

3.2.4 Displaying measured spectra

The VNA detects magnitude, phase, imaginary (Im) and real (Re) parts of the induced voltages (scattering parameters). The detection is phase-coherent with the excitation. For the raw signal $Im[S]$ ($Re[S]$) we evaluate the median value $\langle Im[S(f)] \rangle$ ($\langle Re[S(f)] \rangle$) across all fields, for each frequency point. The median value is subtracted from the raw signal thus obtaining $\delta Im[S_{ij}(f, H)] = Im[S_{ij}(f, H)] - \langle Im[S_{ij}(f)] \rangle$; analogously we obtain $\delta Re[S_{ij}(f, H)]$.

With these two quantities we build the linear magnitude signal as $Mag(S_{ij}) = [\delta Im^2(S_{ij}) + \delta Re^2(S_{ij})]^{1/2}$ where the f and H has been dropped from the notation. Such procedure remove field-independent disturbances in the spectra. In some occasions, where a temporal drift impacts the measurements another route is followed which we call the the next-neighbor subtraction. Values S_{ij} taken at the same frequency and adjacent field values are subtracted according to: $\Delta S_{ij}(f, H_q) = S_{ij}(f, H_{q+1}) - S_{ij}(f, H_q)$; with S_{ij} being the raw linear magnitude as measured by the VNA.

The scientific colour map bam [143] is utilized to display VNA data to prevent visual distortion of the data and exclusion of readers with colour vision deficiencies [108].

3.3 Brillouin light scattering

Brillouin light scattering (BLS) characterization of magnetic excitations is based on magnon-photon interaction. This laser-based technique is harnessed for optical detection from GHz range up to a few THz [13]. It has been pioneered by two independent works of Brillouin ([1]) and Mandelstam ([2]). BLS allows for detection of frequencies of magnons as a function of applied field H and, depending on laser focus, with high spatial resolution. In implementations BLS is used to resolve magnon phase, wave vector, and temporal dynamics [71]. One of BLS key advantages is the ability to probe both coherent and incoherent (e.g. thermally-activated) magnons. In this PhD thesis we rely on this technique to probe magnetization dynamics in top-down nanopatterned Py/YIG hybrid structures and explore thermally-activated magnetization dynamics in surface corrugated Py thin films. In this chapter we introduce the physics this optical spectroscopy technique, we discuss the BLS microscopy and momentum transfer and describe the setup at LMGN focusing on the relevant components for our research. More details can be found in [115].

3.3.1 Basics of Brillouin light scattering (BLS) process

The magnon is detected via magnon-photon interaction. In a semiclassical picture, magnons generate time- and space- dependent variations $\delta\epsilon(\mathbf{r}, t)$ in the dielectric tensor ϵ of the probed magnetic material due to spin-orbit coupling. A photon, that scatters at the surface of the magnetic material, picks up such $\delta\epsilon(\mathbf{r}, t)$ in that the reflected photon is modulated at a frequency f_m , with f_m being the characteristic magnon frequency. In terms of scattering among quasiparticles (Fig. 3.5a,b), an incoming photon ($f_{p,in}, \mathbf{k}_{p,in}$) can generate (annihilate) a magnon (f_m, \mathbf{k}_m) upon scattering and this is called Stokes (Anti-Stokes) process. The quantum-mechanical description imposes energy and momentum conservation therefore the frequency $f_{p,out}$ and wave vector $\mathbf{k}_{p,out}$ of the scattered photon satisfy the following equations:

$$hf_{p,in} \pm hf_m = hf_{p,out} \quad (3.7)$$

$$\hbar\mathbf{k}_{p,in} \pm \hbar\mathbf{k}_m = \hbar\mathbf{k}_{p,out} \quad (3.8)$$

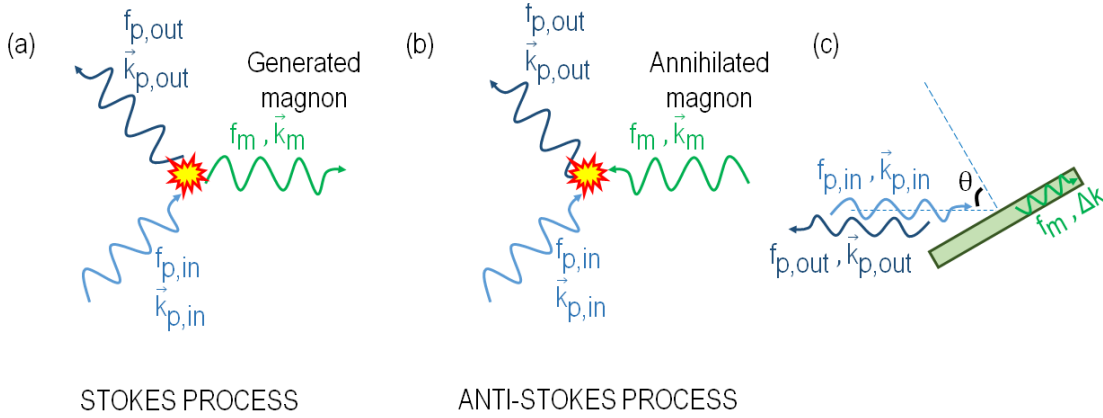


Figure 3.5: (a),(b) Sketches of magnon-photon interaction via a Stokes (magnon creation) and Anti-stokes process (magnon annihilation). (c) Sketch of the incident and inelastically back-scattered beam motivating in-plane momentum conservation with a magnon (green).

Equation 3.8 refers to the case of translational invariance. In the case of magnetic films, this applies to the in-plane momentum component only, i.e. the wave vector components in the plane of the film (Fig. 3.5c). A monochromatic laser beam is focused on the magnetic sample, impinging at an angle θ_{in} . Elastically scattered light is reflected at an angle $\theta_{out} = \theta_{in}$. In the backscattering geometry the BLS detector collects $\mathbf{k}_{p,out}$ being antiparallel to $\mathbf{k}_{p,in}$ (Fig. 3.5c). In this configuration the in-plane momentum transfer Δk is approximated by:

$$\Delta k = 2|\mathbf{k}_{p,in}| \sin \theta_{in} \quad (3.9)$$

Therefore collected photons have a wave vector shifted by the quantity Δk . $|\mathbf{k}_{p,in}| = \frac{2\pi}{\lambda_L}$ is defined by the laser wavelength λ_L . $\lambda_L = 473$ nm and 532 nm, in the two LMGN setup. The maximum achievable $\Delta k = 2|\mathbf{k}_{p,in}| = 26.6$ rad/ μm considering $\lambda_L = 473$ nm. Figure 3.6 shows a full schematic of the μBLS setup including components for time-resolved measurements at LMGN. A monochromatic solid-state laser emits a linearly polarized beam with horizontal polarization. In LMGN setup a solid state laser emits a beam that is focused via an objective lens with numerical aperture $\text{NA} = 0.85$ onto the sample and back-reflected photons ($\theta_{in} = 0^\circ$) are collected. The laser beam is focused down to a beam diameter 250÷300 nm on the sample surface. Given its frequency resolution combined with high spatial resolution, we use BLS to probe magnon propagation and excitations in magnonic crystals with lateral modulation of few hundreds of nm [71], [39], [69]. The temporal allows us to measure group velocities, the lifetimes and decay length.

3.3.2 BLS microscopy setup

The BLS instrumentation offers high-contrast and high-frequency resolution. We use a multi-pass Fabry-Perot interferometer to analyze the scattered light. An extensive and exhaustive description of such setup is available [14, 23]. In our experiments we have used an optical

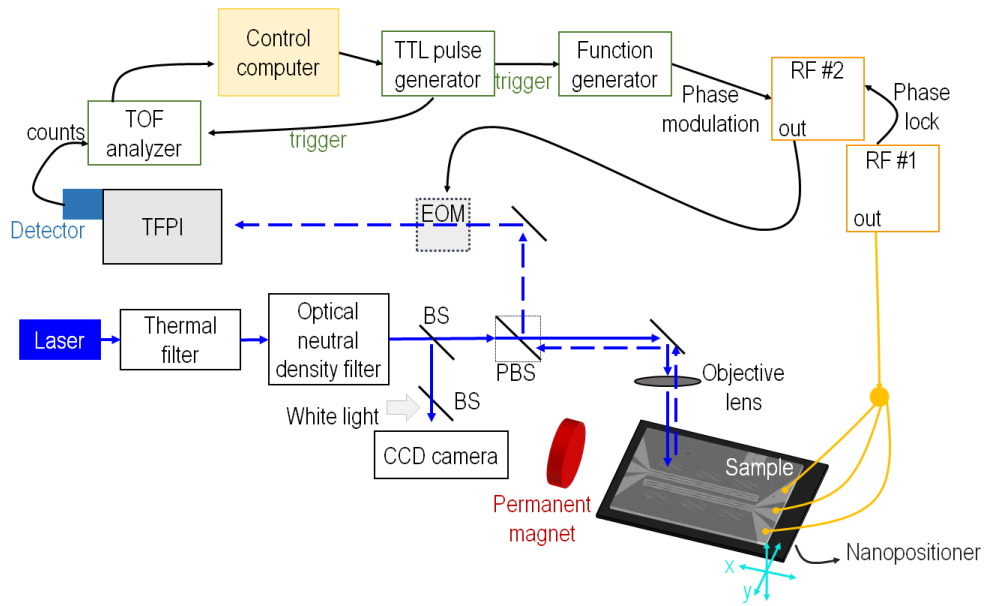


Figure 3.6: Sketch of the whole BLS setup, including components and connections to conduct phase-resolved BLS (PR-BLS). A nanopositioner finely controls the sample position. A permanent magnet generates an in-plane field along $\pm \hat{x}$. The permanent magnet is attached to a moving stage. Hence the field is variable in the range $2 \div 200$ mT. Signal generator 1 (SG1) is connected to the on-chip antenna for coherent magnon excitation while SG2 is connected to an electro-optic-modulator (EOM) to generate a reference signal that is the copy of the same signal injected into the CPW. This is needed for PR-BLS. The TOF analyzer acquires incoming photons and their timestamp.

power ≤ 1 mW when illuminating from the topside (i.e. direct incidence on the YIG surface) and an optical power of ≈ 2 mW when illuminating from the backside through the GGG substrate). The objective lens with NA = 0.85 is an Olympus LCPLFLN100xLCD lens. The large NA collects photons over a broad regime of incidence angles. The backreflected light is composed of both elastically and inelastically scattered photons. The latter are only a small fraction. Typically the signal is $10^{-6} \div 10^{-4}$ times smaller than the elastically scattered part (this estimation is valid for thermally-activated magnons). Upon scattering with magnons, the photon polarization is rotated by 90° . We make use of a Glan-Taylor prism (GTP) to separate the horizontally polarized photons from those that have inelastically scattered. The horizontally polarized photons pass straight the GTP and are partially re-directed to a CCD camera. This signal is utilized to monitor the laser spot on the sample. The inelastically scattered photons have a vertical polarization and after entering on the GTP they are directed to a the six-pass tandem Fabry-Perot interferometer (TFPI) [144]. Photons are transmitted by the interferometer only when matching its frequency. The TFPI frequency is adjusted by controlling the mirror spacing between the relevant etalons. The transmitted photons are received by a silicon avalanche photodiode detector. Each photon causes an electrical pulse that is read out by a time-of-flight (TOF) electronics (Fast ComTec MCS6A). This transmits

further the information to the control computer. The TFPI is controlled via a software package [69] that matches the readout frequency and the time of detection. The information provided by the TOF electronics is key to achieve time-resolution. To excite coherent magnons on-chip integrated CPWs are utilized. The CPW is wire bonded to an RF waveguide that is itself connected via an RF connector to the signal generator (SG1 in Figs 3.6, 3.7). RF excitation of magnons increases the signal strength.

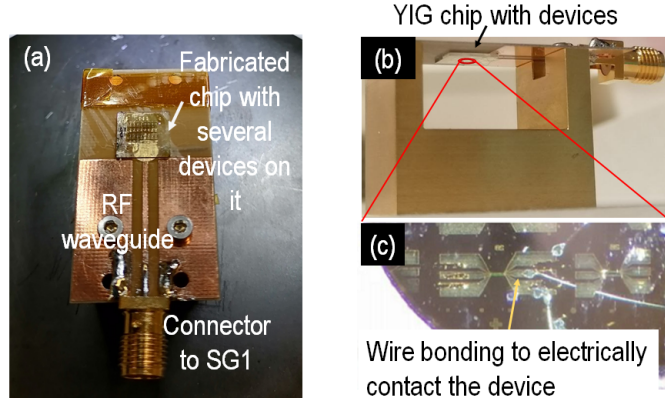


Figure 3.7: (a) The chip is glued on a macroscopic RF waveguide. The CPW and the waveguide are electrically connected via wire bonding. The RF waveguide is connected via an RF connector to SG1 (Fig. 3.6). In the configuration shown the BLS laser is focused on the top surface. (b) The sample is mounted on the same RF waveguide and in this case the whole system is mounted upside down to allow light to impinge through the substrate onto the active region. (c) Detailed picture of the device under study. The photograph is taken looking through the substrate. Bonding wires are attached to the G, S, G pads of the device.

In the case of BLS measurements of thermally-activated magnons the signal generator is turned off. The laser is focused on the sample to probe magnons excited by thermal fluctuations (thermal magnons). This detection scheme reveals the eigenmodes of the magnetic sample. Magnon population starts energetically at the lowest available energy level, therefore the lowest frequency peak observed in BLS indicates the magnon band minimum. Following the KS formalism (sect. 2.5) the DE and BV magnon branches define the range (outer boundaries) of allowed magnon states. Moreover, due to the negative group velocity at small finite k of the BV mode the magnon band minimum in frequency is realized for $|\mathbf{k}| \neq 0$ (Fig. 3.8). The wave vector detection limit (Eq. 3.9) of our BLS setup allows us to probe spin wave excitations up to $|\mathbf{k}_{\max}| = 26.6 \text{ rad}/\mu\text{m}$ (black dashed lines in Fig. 3.8). When discussing the frequency shift of the magnon band minimum in section 4.3.2 we refer to the magnon state with $|\mathbf{k}| \neq 0$, that is detected with the BLS capabilities, residing at the lowest frequency (red arrows in Fig. 3.8).

The integration time to collect the signal from thermal magnons for thin films is usually few hours long to achieve a large signal-to-noise ration. Before data analysis the raw BLS spectra are normalized. The normalization process scales each dataset by the number of the detector photon count at the elastically scattered peak (peak at zero GHz frequency shift). This procedure minimizes effects of drifts and laser power fluctuations on the measured BLS

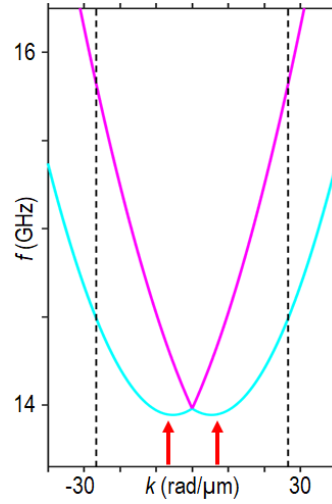


Figure 3.8: DE (magenta) and BV (cyan) magnon branches predicted by the KS formalism (Eq. 2.29) for 5-nm-thick Py in an in-plane field of 240 mT. Further magnetic parameters are $\mu_0 M_S = 797$ mT and $A_{\text{ex}} = 11$ pJ/m. These values are extracted from our own measurements. The red arrows indicate the magnon band minimum that occurs at non-zero finite k . The dashed black lines indicate the BLS wave vector detection limit $|\mathbf{k}_{\text{max}}| = 26.6$ rad/ μm .

intensity thus allowing relative comparison of spectra taken at different fields and for different time periods.

3.4 Top-down nanofabrication

To nanopattern YIG and fabricate on-chip integrated devices we work in the cleanroom infrastructure of the Center of MicroNanotechnology CMi at EPFL. Here we apply self-optimized process flows aiming at the nanofabrication of the devices investigated in this thesis. We benefit of established technical know-how by former PhD students at LMGN as a starting point [115], [127], [116], [119].

3.4.1 Fabrication of one-dimensional periodic arrays of Py stripes

Fig. 3.9 illustrates the main steps to nanofabricate Py/Cu stripes on 113-nm-thick YIG. Cu (5 nm thickness) is DC-sputtered with 1.42 nm/s deposition rate in the Alliance-Concept DP650 sputtering chamber. Py is electron-beam evaporated (Leybold Optics LAB600H) at a 0.4 nm/s rate in a base pressure of $1.5 \cdot 10^{-6}$ mbar. To pattern HSQ stripes, first the sample surface is cleaned with acetone and IPA, then it is dried. An additional cleaning step is taken in that the sample is dipped for 90 s in CD26 (TMAH 2.4%). It has been observed that this improves surface adhesion for our particular choice of materials. The sample is heated for 10 minutes at 120 °C and then let it cool down to room temperature. HSQ 2% (commercially available as XR-1541-002, from DuPont) is spin-coated for 60 s at 4000 rpm. Electron beam lithography

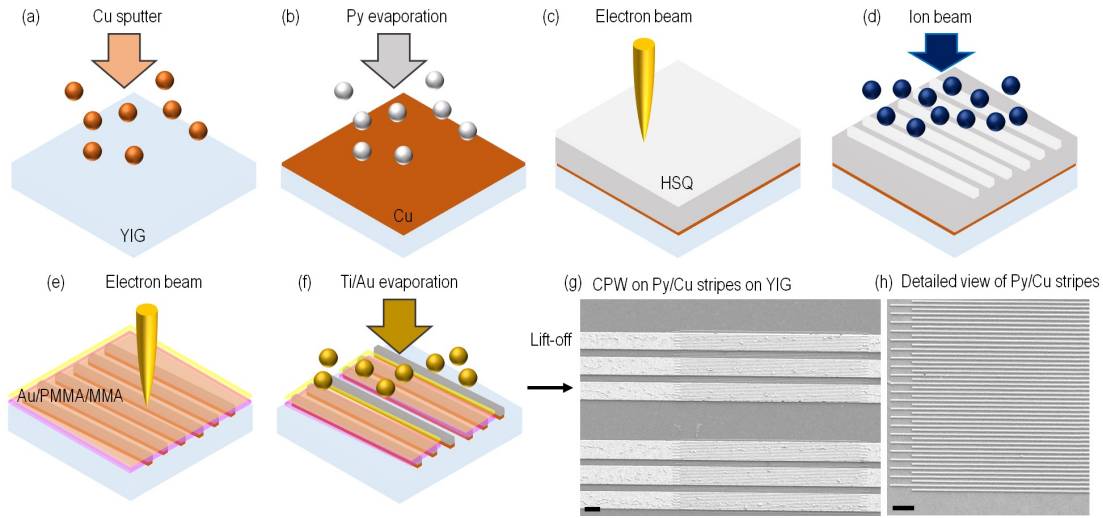


Figure 3.9: Process flow to fabricate Py stripes on 113-nm-thick YIG with Cu spacer. (a-b) After cleaning the YIG surface with acetone, IPA and heating the sample to remove moisture, Cu is sputtered on YIG and Py is evaporated on Cu. (c) HSQ is exposed to EBL and after development HSQ stripes are formed. (d) Using the patterned HSQ as hard mask the same pattern is transferred to the Py layer thus determining Py stripes. (e) The sample is cleaned with acetone, IPA and heated up to remove moisture then is coated with PMMA/MMA + Au for the second EBL so that CPW pattern is exposed. (f) After a descum step, Ti/Au are evaporated to form the CPW. (f-g) SEM images of a completed device and detailed view of the Py stripes. The scale bars are (g) $2 \mu\text{m}$ and (h) $1 \mu\text{m}$.

(EBL), operating at 100 keV, is utilized to write HSQ stripes and CPWs and it is conducted with a Raith EBPG5000+ system. We use a 3 nA beam current and 1.25 nm resolution. The exposure dose is $5400 \mu\text{C}/\text{cm}^2$ and for the proximity effect correction, we set $\beta = 7$ and $\eta = 1.4$. We expose the same pattern at $5200 \mu\text{C}/\text{cm}^2$ and $5600 \mu\text{C}/\text{cm}^2$ to later explore the best produced stripes. The development lasts for 2 minutes in a CD26/NaCl solution. This is a solution that is prepared at LMGN mixing 500 mL of CD26 with 25 g of NaCl (Sodium chloride ROTI@METIC 99.999% (5N)). It is prepared following [38]. Then the sample is gently moved into a water bath for at least 5 minutes. It is important to avoid making bubbles or turbulent flows whenever breaking the liquid surface of developer or water. The last step is to blow nitrogen on the sample to dry it and here also one must take extra care to control the gas flow. The ion beam etching (Veeco Nexus IBE350) step is conducted sending the Ar^+ ions at 3° tilt from the sample surface normal for 56 seconds with the recipe *LOW_IBE* that is developed by CMi staff. After scanning electron microscope (SEM) inspection we decide the optimal pattern onto which CPW are written.

3.4.2 Fabrication of coplanar waveguides on Py stripes

In the second EBL step for coplanar waveguides (CPWs) preparation, both MMA EL9 and PMMA A4 are spin-coated at 4000 rpm. After each spin-coating step the chip is heated at 180°

for 5 minutes. To prepare a conductive layer for EBL we sputter a 10-nm-thick Au top layer. EBL is conducted with 30 nA beam current and 10 nm resolution. The exposure dose is $515 \mu\text{C}/\text{cm}^2$ and for the proximity effect correction, we set $\beta = 7$ and $\eta = 0.2$. Au is removed by wet etching 15 s with a chemical etchant (TechniEtch ACI2) based on $\text{KI} + \text{I}_2$. Resist development in MiBK:IPA 1:3 solution lasts 70 seconds. Then the chip is directly transferred to a water tank. The chip is left in the water for 70 seconds. The development in MiBK:IPA 1:3 solution is time-sensitive. Hence the chip must be fully out of the bath when 70 seconds have elapsed and swiftly transferred into the water-containing beaker. Before Ti/Au evaporation the chip is exposed for 10 seconds to an oxygen plasma (200 W, O_2 flow = 200 sccm and pressure = 0.5 mbar) to remove residuals from the development step, in particular resist residuals at the pattern edges (*descum* step). 5 nm thick Ti and 120 nm Au are evaporated and then the chip is placed in acetone bath for 4.5 days. The lift-off processing is finished by gently rubbing the sample with a cotton swab to remove metal layer residuals.

The process flow described above is conducted to fabricate also magnonic grating coupler on Py/SiO_2 with only exception of step (a) (Fig. 3.9) in that now SiO_2 (5 nm thickness) is evaporated.

3.5 Bottom-up magnonics nanotechnology based on DNA

We emphasize selected concepts and methods of the DNA nanotechnology that are relevant for the experiments. We describe our research methodology to utilize DNA nanotechnology as bottom-up approach to fabricate periodically-patterned magnetic nanostructures. Reviews about how the controlled synthesis of DNA structures has evolved into different branches of nanotechnology can be found in [146], [109], [80], [99], [122], [134], [112], [79]. Along these lines, we conclude this section by describing the experimental protocols we have optimized to prepare such structures.

3.5.1 DNA structure and chemistry

It is instructive to begin with a description of the deoxyribonucleic acid (DNA) structure and its chemistry in order to understand the relevance of this molecule in modern nanotechnology. The DNA structure (Fig. 3.10) was independently investigated by Franklin and Wilkins, who in 1953 observed two periodicities, 0.34 nm and 3.4 nm, in DNA fibers by X-ray diffraction patterns [8], [6] and by Watson and Crick, who in the same year formulated the double helix model for the DNA structure [7]. In the following we describe the details of the DNA structure and chemistry that have led to the proliferation of DNA self-assembly in nanotechnology. The DNA is constituted by deoxyribonucleotides (or nucleotides). Nucleotides have three main components (Fig. 3.11): (i) a nitrogen-containing (nitrogenous) base, (ii) a pentose ring, i.e. an organic cyclic compound with five carbon atoms and (iii) a phosphate PO_4^{3-} (Fig. 3.10). Nitrogen-containing bases are divided in pyrimidine and purine. The former contains Adenine (A) and Guanine (G) bases and the latter contains Cytosine (C) and Thymine (T). In

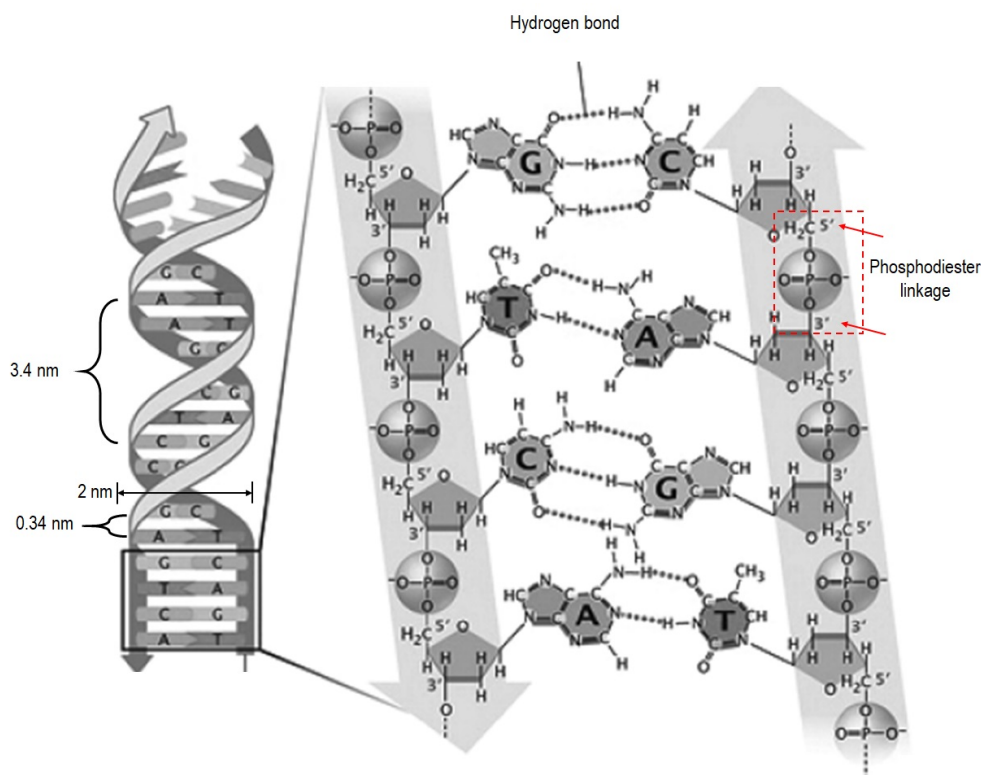


Figure 3.10: This image is adapted from [61]. On the left side the DNA double helix model is shown. The letters A, C, G and T identify the four nitrogen-containing bases. The width of the double helix is 2 nm and the two periodicities 0.34 and 3.4 of the major and minor groove are indicated. On the right side a detailed sketch illustrates the structure inside each single strand and how two single strands interact with each other to form the helix. Inside the single strand 5' and 3' indicate the carbon atom of the pentose ring. The stacking of phosphate groups alternating with pentose rings is forming the DNA backbone. On the side of the backbone the nitrogen-containing bases are leaning out. This facilitates interaction with other bases. The interaction is driven by hydrogen bonds. By convention, single-strand DNA is always written from the carbon atom 5' to the carbon atom 3', in this sketch the vertical arrows indicate this direction for each of the single strand. The phosphodiester linkage is highlighted by the dashed red box

the DNA molecule, successive nucleotides are covalently linked by adjacent phosphate groups forming a phosphodiester linkage [123] (Fig. 3.10). All the phosphodiester linkages along one DNA strand have the same orientation and give the structure a specific polarity. This linkage is formed by two oxygen atoms of the phosphate group which bind to the hydrogen of the carbon atom on site 5' of the pentose ring and to the hydroxyl group of the next nucleotide at the carbon atom on site 3' (red arrows in Fig. 3.10). This provides an ordered stacking of nucleotides which defines a chain structure. The chain forms the hydrophilic and covalently-bounded backbone of the DNA. Pentose rings and phosphates are positioned along the chain while the bases lean on the side of the chain. Bases belonging to different chains interact with each other via hydrogen bonds. These interactions lead to the formation of double-strand

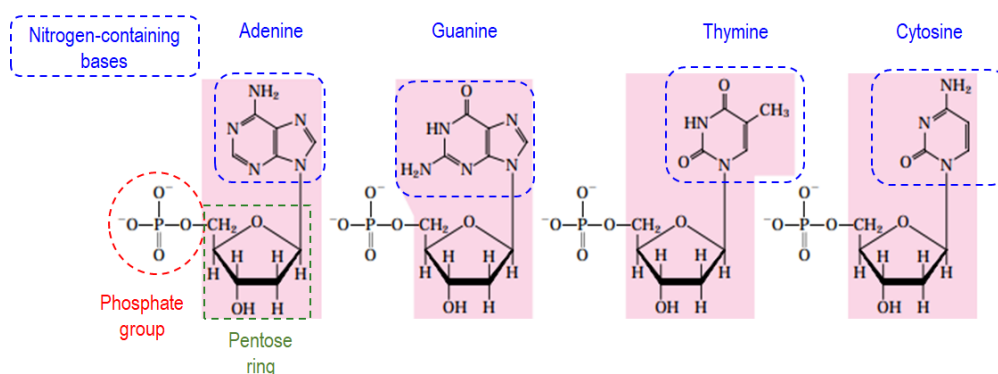


Figure 3.11: This image is adapted from [123]. The structure of the four deoxyribonucleotides is reported. From left to right, respectively, the panel illustrates the Adenine (A), Guanine (G), Thymine (T) and Cytosine (C) bases (on the top) with the chemical bond to the pentose ring. The pentose ring is chemically bonded to the phosphate group.

DNA which has helicoidal structure as predicted by Watson and Crick. The length of a DNA molecule is conventionally reported in units of base pairs (*bp*). The helix periodicity is 3.4 nm. The spacing of neighboring bases on the same single-strand DNA is 0.34 nm. The interaction among bases are specific: A binds to T and C binds to G, there is no A-G and T-C binding. These interactions are often known as Watson-Crick base-pairing interaction and they represent one of the main mechanisms at the core of DNA nanotechnology (section 3.5.2).

3.5.2 DNA nanotechnology

Inspired by the specific base-pairing interaction Seeman proposed in 1982 [15] the first algorithm to form stable DNA junctions and promoted the idea to utilize these as building blocks for more complex structures such 3D objects and crystals. Since then the field of DNA nanotechnology has evolved significantly. In 2006 Paul Rothemund proposed a method to construct arbitrary geometrical shapes by using a long single strand DNA (scaffold) that folds onto itself following a pre-designed pattern [33]. There have been several ongoing efforts to improve DNA structural control, stability and explore the application of DNA-based nanostructures to build nanorobots, plasmonic and photonic structures [112], [51]. DNA self-assembly can be engineered to form 2D and 3D structures at the nanoscale.

To achieve self-assembly we follow two approaches based on (i) DNA origami [118] and (ii) DNA tiles [28]. DNA origami is achieved by hybridization of a long ($\sim 1 \div 2$ kbp) single-strand DNA (*DNA scaffold*) with many short (<60 bp typically) single-strand DNA fragments (*staple strands*). DNA tiles are single-strand DNA fragments of short length (~ 100 bp) that combine together to form a unit that further operates as an element for the assembly of a more complex nanosystem. The tile is a more rigid structure than the origami. Depending on the termination of each DNA fragment the terminal parts of a strand are named *blunt* or *sticky*. The self-assembly of tiles ending with blunt ends occurs via π - π orbital interaction whereas with sticky

ends the interaction among tiles is driven by the conventional Watson-Crick base-pairing. In this thesis we work with DNA tiles possessing sticky ends.

The DNA nanotechnology described so far has demonstrated the ability to build via the bottom-up approach 2D and 3D nanoarchitectures with high spatial resolution [75], [64]. The impact of DNA nanotechnology in nanoengineering and microsystems has been wide. It still gains momentum, in that several fields of research dealing with fabrication and patterning have turned to DNA nanotechnology in an attempt to push the patterning capability to minimum length scales below state-of-the-art lithography. *DNA-assisted lithography* (DALI) has gained interest in that DNA origami has been utilized to pattern at the sub-10-nm lateral length scales silicon substrates. Using DALI plasmonic [92] and photonic new structures were created [76]. In 2018 Gür et al. [86] realized a plasmonic waveguide by stacking horizontally close to each other gold nanoparticles by careful preparation of neighboring DNA strands on a chemically pre-treated substrate. Here the spatial resolution was ~ 2 nm. They achieved plasmon propagation over a series of Au nanoparticles over a few microns. From octahedral DNA frames Shani et al. [113] have created a 3D template that was then coated with Nb and provided a DNA-based 3D nanostructure with structure-engineered superconducting properties.

3.5.3 Bottom-up driven down scaling of magnonic grating couplers

Stimulated by the discussed achievements in different subfields of nanoscience, we aim at patterning ferromagnets by DNA nanotechnology to achieve magnonic nanostructures with unprecedentedly small feature size for, in case of magnonic crystals, ultrashort lattice constants. Our overarching goal is to fabricate magnonic crystals with the first Brillouin zone covering the exchange-dominated range of wave vectors. To this end, we work on developing a novel bottom-up nanopatterning approach realizing periodic patterning at sub-50-nm lateral length scale, thus approaching the exchange-length length scale. In such a way, MCs operate as grating couplers with optimal coupling to exchange-dominated magnons. For this, nanomagnonics requires a down scaling of grating couplers below the ones provided by state-of-the-art lithography. In this thesis, we develop and optimize the technical know-how for DNA-enabled nanomagnonics in terms of surface pre-treatment, deposition protocol and process flow for different DNA samples that we explore. The different DNA structures, that we investigated, are described in the following paragraphs.

Isolated DNA origami on YIG

Considering the exploratory nature of this research and its high risks we approached Tilbit nanosystems [141] which provided preassembled DNA nanoobjects. We ordered two samples that are discussed in this paragraph and in the following one.

It is instructive to begin with the simple cuboid DNA origami (Fig. 3.12). Such DNA-origami nanoobjects are isolated and dispersed on the surface without forming any lattice. Here we

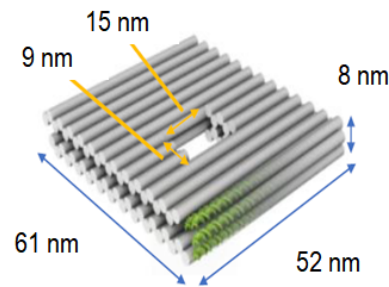


Figure 3.12: Sketch is adapted from Tilibit [141]. The image shows a 3D rendering of the DNA origami with relevant dimensions. We call this structure DNA-PF2.

optimize the deposition for the DNA origami on 100-nm-thick YIG. These experiments are preparatory to acquire technical know-how and we explore protocols to immobilize DNA origami on YIG. The DNA origami design in Fig. 3.12 has a thickness of 8 nm. We call it DNA-PF2. We fine-tune the DNA deposition protocol. When deposited, several separated DNA origami reside on the surface. We target to have a high coverage.

The optimal step-by-step protocol by which we achieve DNA-PF2 coverage on a 100-nm-thick YIG is the following:

- YIG is exposed to an O_2 plasma for 25 minutes at 200 W (O_2 flow = 200 sccm, $P = 0.5$ mbar). The oxygen plasma aims at enhancing surface hydrophilicity which is needed for the DNA-containing solution to spread over the surface. The recipe is conducted in the CMi cleanroom
- Deposition must be conducted immediately after oxygen plasma treatment. The sample is brought to the Programmable Biomaterials Laboratory (PBL) and placed inside a fumehood where we conduct the remaining steps of the protocol.
- Drop-casting of 10 μ l of 0.1 nM concentrated DNA-PF2
- Incubate for 10 minutes: during this time we leave the sample inside a petri dish that is covered with a lid. We put a wet Kimwipe[®] tissue (Sigma Aldrich, Product No. Z188956) on the inner side of the lid so to keep the moisture in the sample environment and avoid that the DNA-containing droplet dries too fast.
- The rinsing step is made of a series of subsequent baths in different ethanol/water (in volume percentage) mixtures: the sample is dipped for 3 seconds consecutively in each of these solutions 25/75, 50/50, 70/30, 80/20 and 90/10.
- Gently drying by blowing inert gas.

Customized DNA origami lattice purchased from Tilibit nanosystems

We discussed in detail a DNA origami sample with Tilibit nanosystems that has a lattice

constant $p = 60$ nm. The design thickness is 8 nm (Fig. 4.24). We deposit the DNA-lattice as template for ferromagnet over-growth. This period p is at the limit of the conventional state-of-the-art nanolithography that our group performs. We intentionally use this structure to establish a comparison to similar geometries fabricated by conventional top-down nanolithography. Via an iterative process involving testing different parameters in the deposition protocol and discussing the experimental outcome with the experts from tilibit named Dr. A. A. Rafat and Dr. T. Aigner, we have achieved the following deposition protocol to obtain DNA lattices immobilized in dry environment on mica. The entire protocol is conducted inside a fumehood in PBL:

- 1 We start with the 50 nM DNA solution that is ordered and obtained from tilibit
- 2 We cleave mica and place it inside a petri dish
- 3 We mix 4 μ l of DNA solution in 46 μ l of buffer A
- 4 We dropcast 50 μ l of the diluted solution onto the mica surface
- 5 We wait 5 minutes of incubation time. We cover the petri dish with a wet dust-free tissue to maintain the moisture in the environment around the sample.
- 6 We rinse with 1 ml of buffer B letting the liquid flow on the surface along a precise direction. We tilt the chip if necessary to maintain the buffer/liquid flow in one direction. This step should take 10 seconds. The buffer is provided from a pipette with an opening diameter of 1 mm.
- 7 We dry away the remaining buffer droplet by blowing inert gas. We use additionally a Kimwipe[®] tissue to soak the droplet from the edge of the mica chip.

All buffers and starting DNA solution have been purchased from Tilibit. Buffer A is prepared with 1 mM EDTA, 5 mM TRIS, 12.5 mM MgCl₂ and 100 mM NaCl. Buffer B is prepared with 1 mM EDTA, 5 mM TRIS and 12.5 mM MgCl₂.

After deposition the DNA lattice geometry is characterized via AFM as it is discussed in section 4.3.1. So far we have presented DNA samples forming isolated structures or with a periodicity that is in the lateral length scale of conventional lithography. Now we introduce the DNA-based structure that enables us to achieve nanopatterning at lateral length scale below 50 nm.

Preparation of DNA-tile-based self-assembled lattice

In this paragraph we discuss our own experimental work by which we fabricate 2D DNA-based periodic lattices (Fig. 3.13). The optimization of the preparation protocol and deposition protocol on mica were very challenging and benefited from the collaboration with the Programmable Biomaterials Laboratory [140] at EPFL. The colleagues are experts in DNA synthesis, protein and cells engineering as well as characterization. We used their experimental

setups to conduct our DNA preparation. Together with PBL our lab purchased a specific DNA synthesizer. By our own synthesis we targeted at a nanoscale DNA lattice which has a honeycomb lattice structure, a feature size of 18 nm and a lattice constant of 30 nm. This lattice is not commercially available. We aimed at this lattice as it would provide the nanotemplate for e.g. Py overgrowth and creation of a surface corrugation in Py that is not achievable by our own top-down nanolithography. The effect of surface corrugation in ferromagnetic thin films is discussed in the framework of magnonics in section 2.8. The main challenge was to achieve the honeycomb lattice in patches with a side length of a few μm .

In the starting phase of the project former PBL members Dr. Kurisinkal, Dr. Hale and Dr. Comberlato trained me on the setups for biological and chemical characterization. For the realization of our targeted sample we consider the processing parameters and the chemical buffers of the published works [101], [32]. Throughout the course of this PhD thesis we found it hard to obtain a reproducible one-to-one correspondence with the published procedures and samples when preparing nominally similar structures. Further exploration and optimization of the annealing protocol were needed. Several discussions with Prof. M. M. C Bastings, the Head of PBL, and Cem Tekin (PhD student at PBL) have led to new annealing processes deviating from those published in [101], [32]. We conducted atomic force microscopy (AFM) and gel electrophoresis (see paragraph 3.5.5) to characterize the DNA samples prepared with the different process parameters. We have found a protocol that works best to achieve 2D DNA honeycomb lattice extending over a few μm . We note that the yield is small. Based on our experience and discussion with PBL members, we assume that the annealing process (see below) is very sensitive to chemical concentration of different constituents in the buffer solution, the humidity and the temperature beyond the control capability that our setups offer on these parameters. The high sensitivity of the process was not known from studying the published works and literature.

By means of DNA-tile self-assembly we prepare two-dimensional DNA honeycomb lattices with a lattice pitch $p = 30$ nm and a hexagon side length $l = 18$ nm. The DNA lattice thickness is 2 nm when this is adsorbed perfectly flat on the substrate. The thereby designed surface corrugation is expected to be large enough to induce band-structure formation by surface corrugation as predicted by the formalism in [85].

3.5.4 Annealing and deposition protocols of DNA honeycomb lattice

In Fig. 3.13 we report the building block of the honeycomb lattice (Fig. 3.13a). This is a tripod, i.e. a three terminal junction. At the end of each terminal there is an overhanging strand providing the sticky end. The tripod is formed by combining three different single strands (strand #1, #2 and #3 in Fig. 3.13). We prepare a liquid solution containing the three strands. The procedure to prepare the liquid solution was first presented in [101]. The authors of this work, in particular Dr. Kurisinkal, trained us in the starting phase of the project concerning the preparation of the liquid solution containing DNA strands.

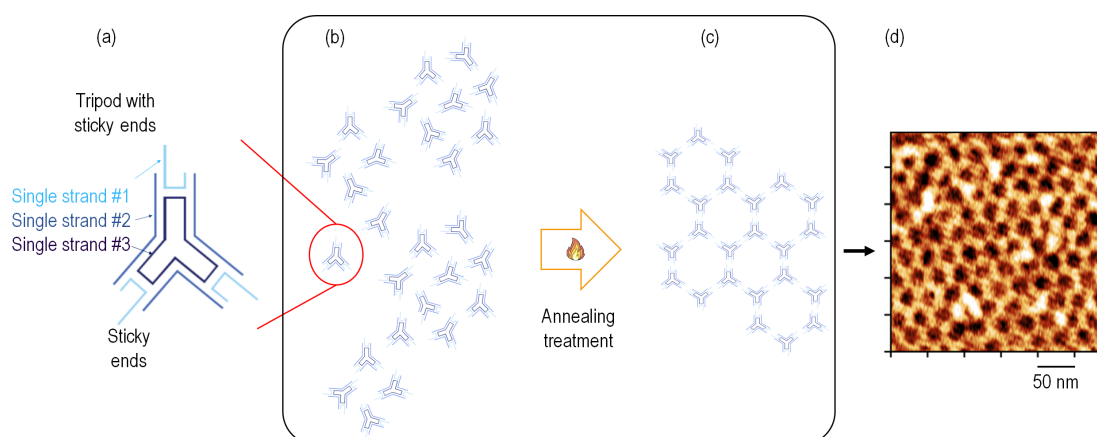


Figure 3.13: (a) The tripod is the building block of the self-assembled 2D honeycomb lattice. The tripod is formed by three strands that are shown with different colors: strand #1, #2 and #3. (b) The liquid solution contains tripods that are randomly dispersed. (c) After annealing the tripods have interacted with each other via sticky ends and have formed the periodic lattice. (d) The honeycomb lattice is imaged with an atomic force microscope after deposition on mica in dry environment.

The liquid solution is prepared by adding strand #1 ($0.6 \mu\text{M}$), strand #2 ($1.8 \mu\text{M}$), and strand #1 ($1.8 \mu\text{M}$) to 5 mM tris(hydroxymethyl)aminomethane (TRIS) (BioRad,#1610716), 1 mM ethylenediaminetetraacetic acid (EDTA) (Cat. No. 60-00-4), 10 mM magnesium acetate (MgAc2) (Cat. No. 16674-78-5). The liquid solution is based on sterile filtered MilliQ water. We have specified the concentration of each constituent because their actual volume amount depend on the total volume of the final liquid solution. Here below we give an example of the step-by-step preparation protocol for $100 \mu\text{l}$ total volume of liquid solution. We assume these following starting concentrations: strand #1 ($C_1 = 12 \mu\text{M}$), strand #2 ($C_2 = 12 \mu\text{M}$), strand #1 ($C_3 = 12 \mu\text{M}$), TRIS ($C_{\text{TRIS}} = 50 \text{ mM}$), EDTA ($C_{\text{EDTA}} = 10 \text{ mM}$) and MgAc2 ($C_{\text{MgAc}_2} = 100 \text{ mM}$).

- 1 Using the starting concentrations, calculate the volume of each chemical constituent to be added in the final liquid solution to obtain the targeted final concentration. For example, to obtain $0.6 \mu\text{M}$ strand #1 in the final solution we estimate the volume to be added to be $V_1 = \frac{100 \mu\text{L} \cdot 0.6 \mu\text{M}}{C_1} = 5 \mu\text{l}$.
- 2 The sum volume of all these chemical constituent is smaller than $100 \mu\text{l}$, i.e. the total volume. Calculate this difference volume δV .
- 3 δV amounts to the volume of sterile filtered MilliQ water that must be added
- 4 In a PCR tube (Fisherbrand™ 0.5mL Flat-Cap PCR Tube, Cat. No 14-230-200) pour the sterile filtered MilliQ water first.
- 5 Then add $10 \mu\text{l}$ TRIS
- 6 Add $10 \mu\text{l}$ EDTA

- 7 Then add 10 μl MgAc₂
- 8 Mix the solution
- 9 Then add 5 μl strand #1
- 10 Then add 15 μl strand #2
- 11 Then add 15 μl strand #3
- 12 Mix the solution and split in two tubes of equal volume
- 13 The solution is ready for annealing and the annealing is started (see below).

This process is adapted from [101]. The liquid solution undergoes a thermal treatment, called annealing. After annealing the tripods in the solution have formed the honeycomb lattice by interacting with each other according to the base-pairing interaction (Fig. 3.13c). The annealing process is a thermal treatment and supports the lattice formation extending over long-range. A review on temperature control for lattice formation by DNA nanotechnology is found in [98]. A small volume of the liquid solution is taken and drop-casted on the mica sample to immobilize the DNA honeycomb lattice on the dry substrate. In the following we provide the protocols for annealing and for deposition in air on a dry mica substrate. Mica is the established substrate material to attract the charged DNA material such that flat patches can be achieved. We tested the optical properties and found that BLS spectroscopy can be performed through mica. This offers specific advantages for the investigation of samples.

We present the annealing protocol to fabricate the targeted 2D DNA-based lattice. The best annealing recipe to prepare the DNA honeycomb we have established is the following:

- 1 Heat up the liquid solution to 80 °C and incubate for 5 minutes
- 2 Lower the temperature to 65 °C and incubate for 10 minutes
- 3 At a rate of -1 °C/h the solution is cooled from 65°C to 22 °C for 43 cycles.
- 4 Then the solution is kept at 22 °C.

In case the sample is not used within a few hours after the end of the annealing process, the solution is stored at 4 °C.

Once the annealing step is completed the DNA is deposited on mica. The operation is conducted inside a ventilated fumehood to avoid contamination. This is the step by step procedure that we follow:

- 1 Mica is cleaved and tilted at an angle $<10^\circ$.

- 2 Drop-cast 2 μl of DNA lattice on the center of the mica chip.
- 3 Incubate for 10 s
- 4 Rinse with 10 μl of MgAc_2 (Mg^{2+} concentration = 10 μM)
- 5 Rinse with sterile filtered Milli-Q water
- 6 Dry the liquid droplet by touching the chip edges with a thin Kimwipe[®] tissue
- 7 Blow with inert gas to dry

Steps 6 and 7 must be conducted with extra care, paying attention to touch only the edges of the chip and to regulate the gas flow respectively. Milli-Q water is a type of highly purified water with conductivity 0.055 $\mu\text{S}/\text{cm}^2$ and no particle residual above the 0.22 μm dimensions. DNA lattice formation and geometry is characterized by atomic force microscopy (AFM). We note that the scientific literature presents different strategies to immobilize DNA lattices on surfaces. In the starting phase of the project we discussed with members of the LBNI group [145] at EPFL, who contributed to the this work published in [101]. This helped us to further fine tune the different steps and parameters for our final deposition protocol outlined above. The protocol was then optimized over the course of repeated measurements.

3.5.5 Gel electrophoresis

Gel electrophoresis (EP) is a well-established technique in the field of biology to probe the structure of DNA and peptides [25] without involving a drying process. The EP is a technique that separates charged biomolecules in a solution via the drift motion under the presence of an applied uniform electric field. A detailed review and exhaustive introduction of the EP technique can be found in [25], [52]. In EP, a gel is used as the matrix within which DNA and proteins migrate under the influence of an electric field. In our research we work with agarose and polyacrylamide (PA) gels. The latter has higher resolving performance. Agarose is a polysaccharide (complex sugar), PA is a molecular sieve obtained by mixing acrylamide and bis-acrylamide. Agarose is easy to prepare, is non-toxic and allows for fast readout. Figure 3.14 reports a photograph of the agarose gel after electrophoresis completion. The agarose determines the pore size which is the key aspect when fine-tuning the parameters of the electrophoresis to the sample to be probed. PA is a neurotoxin, extra-care must be taken when preparing the gel which takes longer. However the pore size is more uniform. Agarose gel is usually adopted to study DNA fragments of length 50÷20000 base pairs (bp), whereas PA resolves small fragments and works up to 500 bp. We combine agarose gel electrophoresis with AFM. We use PA gel electrophoresis (PAGE) as a troubleshooting tool to investigate the correct folding and annealing of periodic structures. To inspect the gel after EP, a UV illumination tool is adopted. Prior to casting the DNA into the gel matrix, the DNA is mixed with a color dye, which fluoresces upon UV irradiation.

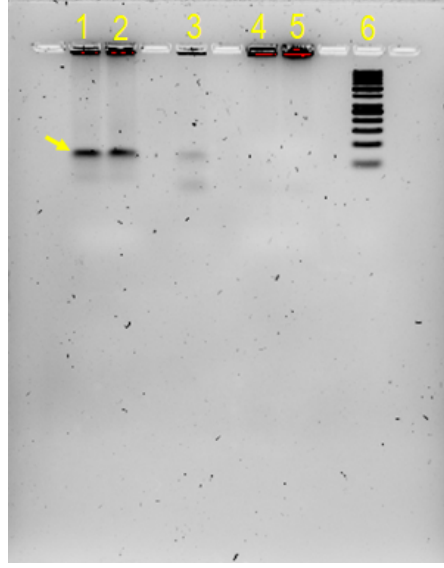


Figure 3.14: (a) Electrophoresis documentation using an agarose gel and UV illumination. The yellow numbers identify the lanes loaded with different samples. This gel documentation is part of a study that we conducted to troubleshoot the quality and degradation of DNA honeycomb lattice samples prepared at an earlier time. Each black band (an example is indicated by the yellow arrow) represents DNA fragments with a certain length. The last lane to the right (lane 6) is the reference sample called *DNA ladder* with DNA fragments of known length.

3.5.6 Evaporation of Py on DNA on a bare mica substrate

In Fig. 3.15 we sketch our approach to deposit the ferromagnetic thin films. After AFM characterization of the DNA lattice on mica we evaporate a Py thin layer followed by an Al layer to protect against oxidation (Fig. 3.15a). The ferromagnet is covering the DNA shown in Fig. 3.15b. We expect that the ferromagnet inherits the periodic surface corrugation of the DNA structure. The FFT analysis of the topography signal acquired on a Py film is reported in Fig. 3.15c. The FFT analysis demonstrates that the surface corrugation is taken by Py. The peaks (circles) correspond in reciprocal space to a wave vector $|\mathbf{k}_{\text{GC1}}| = 232 \text{ rad}/\mu\text{m}$. In real space this corresponds to a wavelength $\lambda = \frac{2\pi}{|\mathbf{k}_{\text{GC1}}|} = 27 \text{ nm}$. This wave vector could give rise to the first grating coupler mode of the surface corrugated ferromagnet. It falls inside the exchange dominated regime of spin waves. To highlight the importance of the specific surface corrugation that we achieved in Py, we now envision that this wave vector is provided to a magnon resonance in YIG. For the YIG parameters of Fig. 2.3, the KS formalism predicts a resonant frequency f_r (group velocity v_g) in Damon-Eshbach configuration at $|\mathbf{k}_{\text{tot}}| = |\mathbf{k}_{\text{GC1}}|$ of $f_r = 87 \text{ GHz}$ ($v_g = 4.4 \text{ km/s}$). For a magnonic crystal the wave vector $|\mathbf{k}_{\text{BZ1}}| = 116 \text{ rad}/\mu\text{m}$ defines the first Brillouin zone that falls inside the exchange-dominated regime. The wavelength associated to $|\mathbf{k}_{\text{BZ1}}| 116 \text{ rad}/\mu\text{m}$ this wave vector is $\lambda = 54 \text{ nm}$.

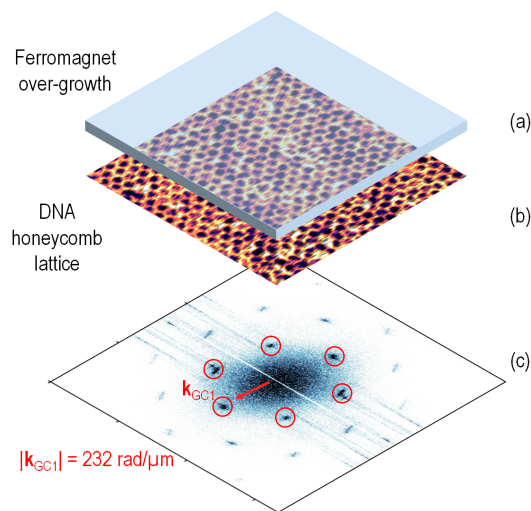


Figure 3.15: (a) Ferromagnetic layer is deposited on top of (b) the DNA lattice. Here the DNA lattice is the honeycomb geometry. The ferromagnetic thin film on top of the DNA lattice exhibits periodic surface corrugation. (c) The FFT analysis of the topography signal show the typical hexagonal diffraction pattern. The red circles identifies the first diffraction mode. The red arrow indicate the wave vector length $|k_{GG1}| = 232 \text{ rad}/\mu\text{m}$. In the FFT image (c) higher-order diffraction are observed.

3.5.7 DNA deposition on pre-processed substrates

In section 3.5.1 we introduced that the backbone structure of the DNA is negatively charged because of the ionized phosphate groups (Fig. 3.10). Here we introduce how electrostatic charges and interactions determine practical aspects of DNA-based structures' preparation and on-surface immobilization.

To maintain the structural integrity of DNA-based lattices and to enable their immobilization on substrates, cations are used to counterbalance the excess negative charge. Cations are added to the DNA-containing solution before the thermal annealing. Furthermore, cations are used in the chemical buffers that are utilized during the deposition protocols. The type and concentration of cations are parameters that need to be explored and optimized. In our case we have adopted 10 mM Mg^{2+} . Mica is a widely used common substrate because it is easy to cleave and after cleavage its surface is atomically flat [73]. Mica contains K^+ in each cleavage plane but these ions diffuse easily away when mica is immersed in water. Hence to mediate the interaction between the DNA-based lattices and the mica, divalent cations are used to counterbalance the negative charge of mica and create an electrostatic bond to the phosphate groups in the DNA [68]. Several works have focused on characterizing DNA-based lattices' stability and on-surface immobilization as functions of type and concentrations of cations [84], [87]. As the main component of the liquid solution is water, the substrate onto which one aims at immobilizing DNA samples must be hydrophilic. This means that the substrate must have a negatively charged surface. This is achieved by pre-treating the substrate with oxygen plasma which leads to the formation of oxygenated groups on the substrate surface.

Oxygen plasma is a widely used technique to enhance hydrophilicity and promote adhesion of DNA-based structures on substrates [49], [120], [102]. The oxygen plasma treatment is a process that must be optimized for the specific DNA-based structure that one is using and the targeted substrate for deposition.

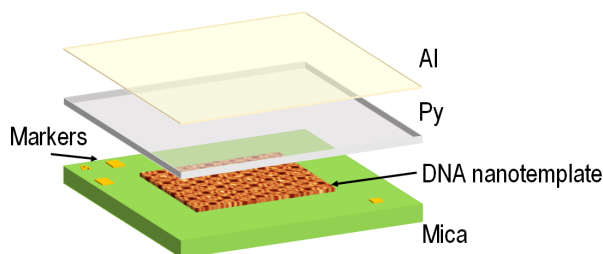


Figure 3.16: A graphical view of all layers realizing the bottom-up nanopatterned Py thin film. Markers are fabricated via EBL and lift-off processing on mica for identification and retrieval of regions of interest during measurements, then the DNA lattice is immobilized on mica in dry environment. Py is evaporated in a vacuum chamber and capped, without breaking the vacuum, by a thin layer of Al as a protection layer from oxidation.

To enable spatially resolved and reproducible BLS microscopy we fabricate markers on relevant substrate before depositing the DNA samples. The markers enable us to define specific regions of interest (ROIs) that are decorated by the DNA sample. By the markers, we readdress reproducibly the ROIs in the μ BLS setup. They allow us also to relate AFM topography images to BLS microscopy data. In the presence of the prepatterned markers, the mica can not be cleaved before DNA deposition. The top-down patterning likely modifies the surface charge and chemistry of the substrate. These modifications have an impact on the DNA adsorption. Hydrophilicity enhances DNA adsorption. To achieve this we pre-treat the surface of mica with 10 s of oxygen plasma at 200 W. We use an O_2 flow of 200 sccm and a pressure of 0.5 mbar. After the oxygen plasma treatment we conduct the DNA deposition within the shortest timescale possible. We have observed that for YIG the oxygen plasma treatment must be extended to 25 minutes to absorb DNA. After DNA deposition, the sample is imaged in dry environment at room temperature with an atomic force microscope (AFM). After localizing several ROIs we proceed with the Py evaporation followed by Al evaporation processes. We do not break the vacuum between the two evaporation processes. The Al layer protects the Py from oxidation (Fig. 3.16).

4 Results

4.1 Magnon-induced reversal of Py stripes integrated on 113-nm-thick YIG

Stimulated by the previous work on magnon-induced magnetization reversal of Py stripes prepared directly on YIG [133], [115] we fabricated on 113-nm-thick YIG one-dimensional grating couplers by patterning Py stripes with 200 nm periodicity. The Py stripes are 20 nm thick, 100 nm wide and have alternating lengths 25 and 27 μm . We prepared two kinds of devices: (i) with a Cu spacer (*sample_Cu*) and (ii) with a SiO₂ spacer (*sample_SiO₂*) between Py and YIG. In both cases the spacer were 5 nm thick. The objective was to study the nonlinear phenomenon of magnon-assisted magnetization reversal in the presence of (i) spin currents and dipolar coupling and (ii) only dipolar coupling, respectively. The work contributes to an understanding about which interaction is important for the reversal and about the power efficiency of different magnon modes to induce switching.

4.1.1 All-electrical spin-wave spectroscopy characterization

Based on the two sets of samples we conduct field- and power-dependent spectroscopy to measure reflection and transmission to understand the global response of the device in the frequency domain and identify critical fields and powers that are relevant for magnon-induced reversal. The devices are measured in Damon-Eshbach (DE) configuration. The field H is swept from negative to positive values so that the SW transmitted signal at $H > 0$ is in the favorable direction of the DE non-reciprocity. The power is swept from the lowest to the highest values. Figure 4.2 (4.3) summarizes reflection (transmission) measurements for devices with the two kinds of magnetic interfaces for $P_{\text{irr}} = -25, -15$ and -5 dBm.

It is instructive to comment on the observed resonance frequency resonances in Fig. 4.1. The field is swept from -90 to +90 mT with 2 mT steps. The measurement is conducted at $P_{\text{irr}} = -25$ dBm. The signal non-reciprocity between negative and positive fields is explained by the SW propagation in DE configuration. The branches existing from -90 to 0 mT and the ones at high

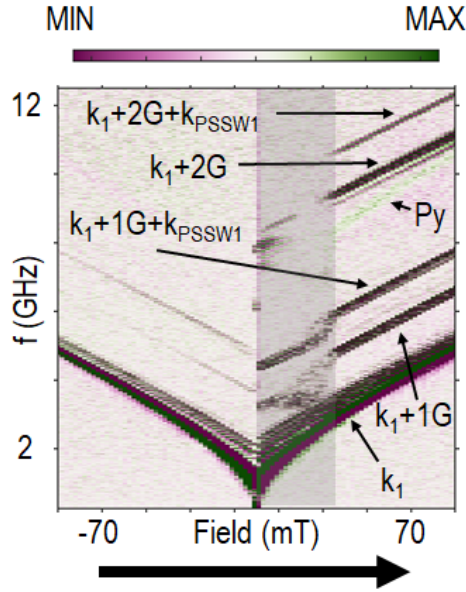


Figure 4.1: Transmission spectrum ΔS_{21} for *sample_Cu*. The shaded field regime is the interesting regime for studies on magnon-induced reversal.

positive fields are explained by Kalinikos-Slavin formalism [16]. In these field ranges the Py stripes are parallel aligned with the YIG and the external field. The corresponding wave vectors are indicated inside the panel for each branch for large H . k_1 is the main CPW-induced mode, G is the reciprocal lattice vector of the periodic lattice made of Py stripes and k_{PSSW1} is the wave vector of the first perpendicular standing spin wave (PSSW) mode. All these branches, indicated in Fig. 4.1, have positive slope $df/dH > 0$.

At low positive fields (the gray shaded area) branches behave differently and exhibit shifted frequencies. This is the region of interest for magnon-induced reversal. Figure 4.2 summarizes reflection spectra for *sample_Cu* and *sample_SiO2* showing linear magnitude of scattering parameter S_{11} after nearest neighbor subtraction. The field H is swept from -90 to +90 mT. Here we focus on the field region from -10 to +50 mT. Spectra are taken at different irradiation powers $P_{irr} = -25, -15$ and -5 dBm. For negative fields the Py and the YIG are aligned to the external field. The internal field reduces as H is brought to zero. Hence we observe branches going to lower values (with $df/dH > 0$). Crossing zero field, several branches show a frequency discontinuity and then $(df/dH) > 0$. The coercivity of YIG is ≤ 2 mT. Two branches (indicated with blue arrows in Fig. 4.2a) feature $df/dH < 0$. We interpret the upper one of these branches to be the Py ferromagnetic resonance when the Py magnetization is antiparallel to \mathbf{H} and to the YIG (*AP state*). Due to shape anisotropy, the coercivity of the Py stripes is larger than that of the plain film YIG (that is ≤ 2 mT). In the AP state, the Py internal field decreases as the external field is gradually increased. Hence the Py frequency branch has negative slope $df/dH < 0$. When the external field exceeds the Py stripes' coercivity they align parallel to \mathbf{H} and branches $df/dH > 0$. In the following we call this field, where $df/dH < 0$ is regained,

critical field. The two lower frequency branches are interpreted as resonances from the

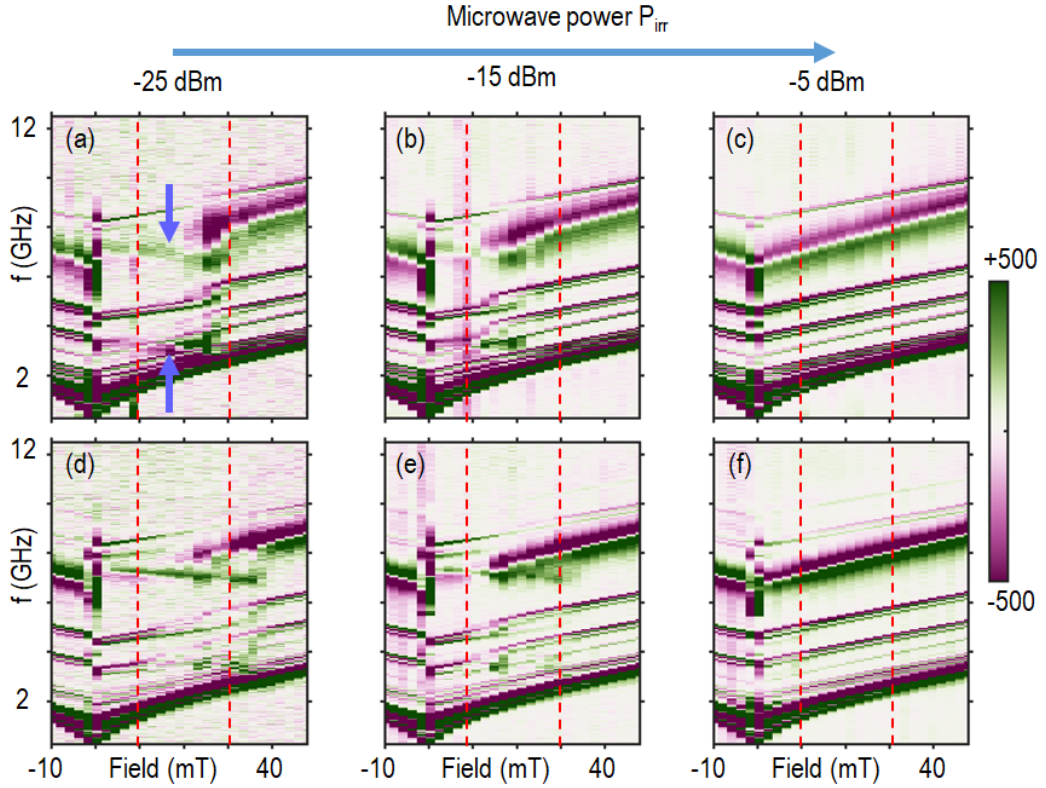


Figure 4.2: Reflection spectra ΔS_{11} for (a)-(c) *sample_SiO₂* and for (d)-(f) *sample_Cu*. Irradiation power is indicated for each of the three columns. The system is each time initialized at -90 mT, here the reported spectra focus on the magnetic field region of the nanomagnet reversal. Red dashed lines reflect 21 mT (left) and 34 mT (right). The blue arrows in (a) mark branches discussed in the text

magnonic grating coupler effect in the AP state. The presence of Cu or SiO₂ modifies the strength of selected branches (compare the branch indicated by the red arrow in Fig. 4.3f). In particular those modes coupling to PSSW feature larger signal with Cu spacer. In the literature [88] PSSWs in exchange coupled hybrid structures show enhanced signals. The Cu spacer allows for dynamic exchange interaction via spin currents [30] as the Cu thickness is smaller than the spin diffusion length [36]. We observe narrow linewidths for magnon modes in YIG. The Py fundamental mode has a broader linewidth. For the same resonance, the linewidth is broader in materials with larger Gilbert damping. This can be appreciated by comparing the linewidths of the branches of the second GC mode in YIG and the Py fundamental mode in Fig. 4.2. In a further experiment we have recorded the thermal spectra of Py resonance by means of microfocus BLS while magnons were propagating in the underlying YIG. We did not observe any change in Py linewidth due to magnons in the underlying YIG layer.

In the following we discuss changes in coercive fields when measuring at increased power.

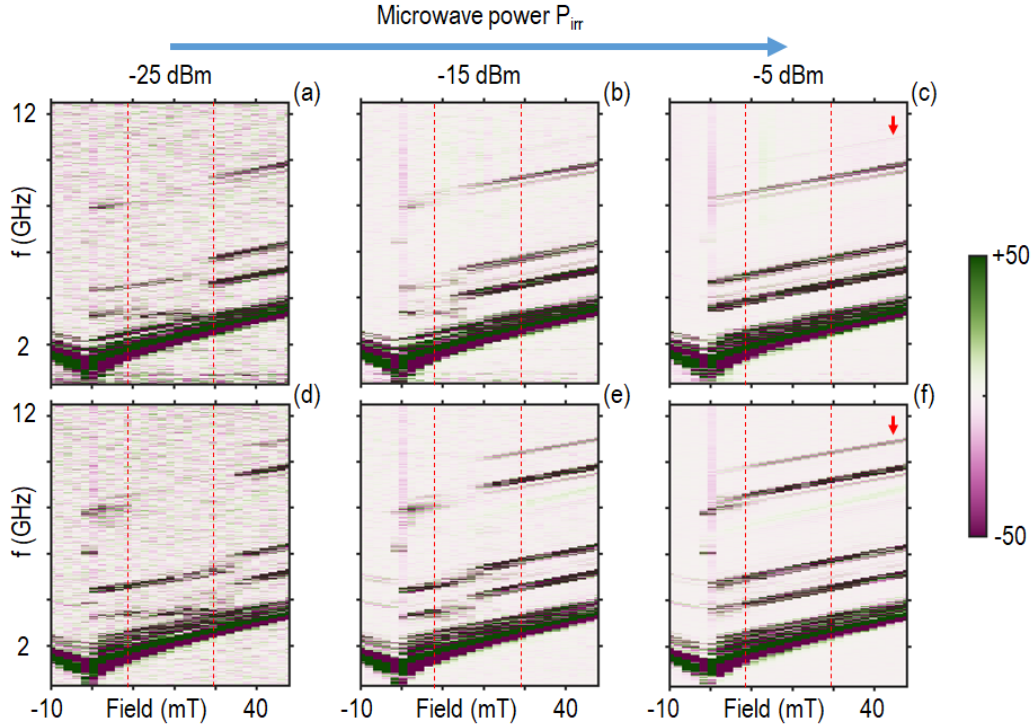


Figure 4.3: Transmission spectra ΔS_{21} for (a)-(c) *sample_SiO₂* and for (d)-(f) *sample_Cu*. Irradiation power is indicated for each of the three columns. The system is each time initialized at -90 mT. Here the reported spectra focus on the magnetic field region of the nanomagnet reversal. Red dashed lines are guides to the reader's eyes to identify critical field reduction as P_{irr} is increased. (c) and (f) The red arrows indicate the PSSW2 branch in YIG.

From the VNA measurements at -30 dBm we estimate the Py coercivity field to be (26 ± 2) mT [(38 ± 2) mT] for *sample_Cu* [*sample_SiO₂*]. The coercivity for the nominally same Py stripes is influenced by (i) edge and surface roughness and (ii) the stripes' mutual interaction. The mutual interaction is modified via the interface and substrate. The interface is different due to the Cu and SiO₂ spacers. One can not exclude the impact of their different roughness. It is known that a magnetic underlayer affects interactions within a magnetic lattice (e.g. [111]). As we increase P_{irr} the critical field reduces which indicates the switching of Py stripes. The critical field reduction depends on the interface (compare e.g. Fig 4.2b,e). The same reduction of critical fields is observed in the transmission signal in Fig. 4.3. For this study we have repeated the measurements at $P_{\text{irr}} = -30, -25, -20, -15, -10, -5$ and 0 dBm. The nonlinear regime starts at $P_{\text{irr}} \approx -10$ dBm. The selected power range is such that we investigate the device response in both linear and nonlinear regime.

Following the approach of published literature we identify three regimes in Fig. 4.2: *AP state*, *X state* and *P state* [126],[96]. We describe the X state as a transition regime within which the stripe arrays undergo reversal. In this field regime, we attribute the reduced (vanishing) transmission to the magnetic disorder arrays. We identify two critical field values to mark the

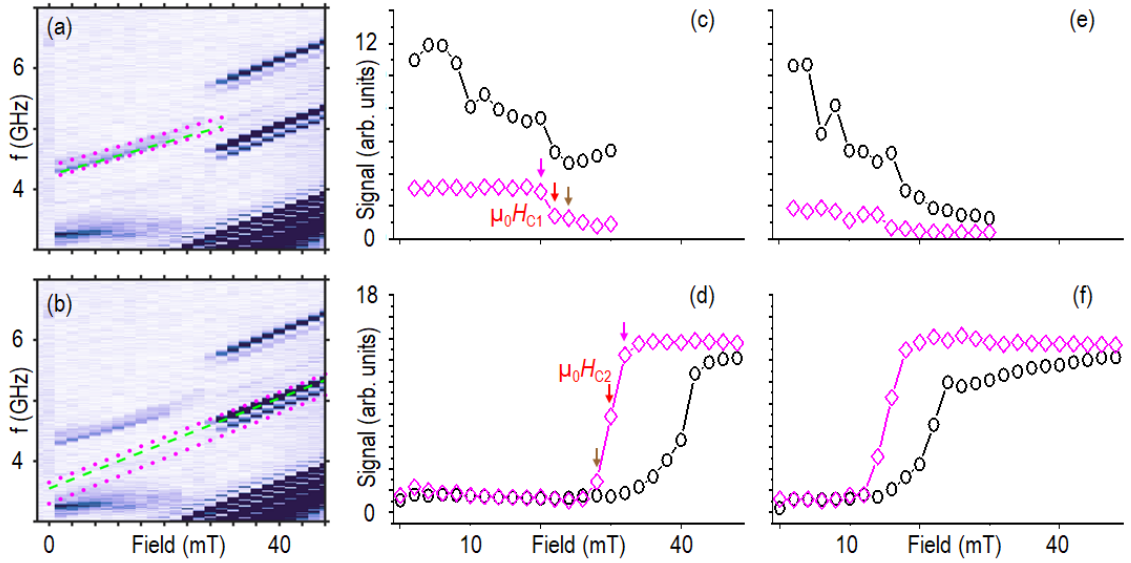


Figure 4.4: (a),(b) $\text{Mag}(S_{21})$ measured with *sample_SiO₂* at $P_{\text{irr}} = -25$ dBm. The two branches that are used to extract the critical fields $\mu_0 H_{C1}$ and $\mu_0 H_{C2}$ are highlighted, respectively, in (a) and (b). The dashed green line indicates the frequency of the maximum intensity and the magenta dotted lines identify the frequency window over which the signal is integrated. (c) [(d)] Integrated signal extracted from (a) [(b)] at $P_{\text{irr}} = -25$ dBm. (e),(f) Integrated signal extracted from $\text{Mag}(S_{21})$ at $P_{\text{irr}} = -15$ dBm. (d),(e) For both the rising and falling branches, field values that realize 30% (brown arrow), 50% (red arrow) and 70% (magenta arrow) of the measured maximum intensity are extracted.

beginning ($\mu_0 H_{C1}$) and end ($\mu_0 H_{C2}$) of the field region labelled as X. For both samples, $\mu_0 H_{C1}$ and $\mu_0 H_{C2}$ become smaller as P_{irr} is increased. This effect is attributed to the nanomagnet reversal by propagating magnons as reported first in [133]. A magnon with large enough amplitude reaches the remotely located nanomagnets and induce magnetization switching. To quantify the critical fields with respect to P_{irr} we analyse the intensity of selected branches as a function of magnetic field and P_{irr} . Figure 4.4a,b shows the branches as a function of $\mu_0 H$ at -25 dBm. We integrate these branches and report the signal strength as a function of $\mu_0 H$ (Fig. 4.4c-f). For each curve we record the field values at which 30, 50 and 70% of the maximum signal strength are reached. We repeat this analysis at different P_{irr} and for the AP and P branch.

The results are summarized in Fig. 4.5 for *sample_Cu* (circles) and *sample_SiO₂* (diamonds). The data points identify the magnetic field at which 30% (Fig. 4.5a), 50% (Fig. 4.5b) and 70% (Fig. 4.5c) of the maximum signal strength is achieved. The critical fields decrease as the irradiation power increases. For $P_{\text{irr}} < -15$ dBm the switching field distribution defined as $\mu_0 H_{C2} - \mu_0 H_{C1}$ is larger for *sample_Cu* (14 mT) than for *sample_SiO₂* (6 mT). For $P_{\text{irr}} > -15$ dBm the switching field distribution becomes narrower for both samples, however the critical fields for *sample_Cu* settle to larger values than those recorded in *sample_SiO₂*.

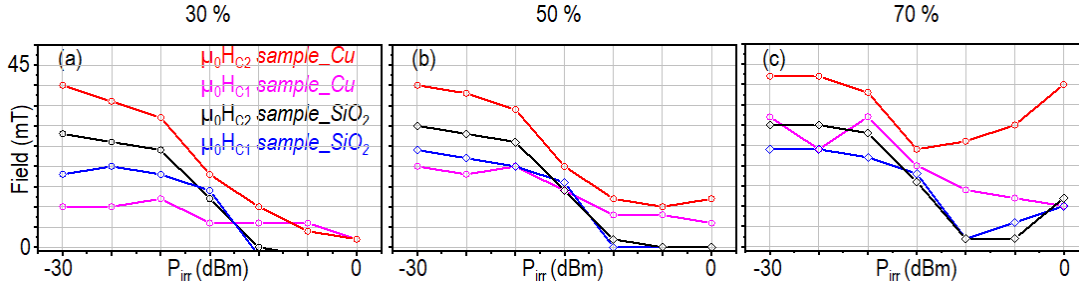


Figure 4.5: $\mu_0 H_{C1}$ for *sample_Cu* (*sample_SiO₂*) is reported in magenta circles (blue diamonds). $\mu_0 H_{C2}$ for *sample_Cu* (*sample_SiO₂*) is reported in red circles (black diamonds). The power-dependent behaviors of the field realizing the 30, 50 and 70 % values are shown in (a), (b) and (c).

Interestingly, at -5 dBm (316 μ W) the critical fields are, within error bars, reduced to zero (< 2 mT) for *sample_SiO₂*. For *sample_Cu* we record the smallest critical field $\mu_0 H_{C1} = 6$ mT. The smallest switching field distribution is 2 mT for $P_{\text{irr}} = -5$ dBm. When P_{irr} approaches 0 dBm, the $\mu_0 H_{C2}$ error bars increase. We observe that at large power levels the field value achieving 70 % of the signal strength moves to higher fields. Again a similar behavior was reported in [133]. We suggest that this is caused by the onset of nonlinear behavior. Additionally we note that this reentrant behavior for $\mu_0 H_{C2}$ is more prominent in *sample_Cu* than in *sample_SiO₂*. In Fig. 4.5a the field $\mu_0 H_{C2}$ for $P_{\text{irr}} = 0$ dBm increases to 40 mT (red curve) which is almost identical to the value in quasistatic switching regime (i.e. $P_{\text{irr}} = -30$ dBm) in *sample_Cu* (45 mT). In the same panel for comparison the field rises to 12 mT for $P_{\text{irr}} = 0$ dBm in *sample_SiO₂* whereas the quasistatic switching occurs at 30 mT. We suspect that his behavior is related to the different interfaces. We speculate this is connected to interfaces Py/YIG and Py/Cu/YIG allowing for spin current transmission from YIG to Py.

4.1.2 Switching yield diagram

To analyse the efficiency of different kinds of magnons to induce the magnetization reversal. We conduct another experiment using the Vector Network Analyzer (VNA). We follow the methodology described in [133]. The system is magnetized at -90 mT and then the field is gradually increased to +14 mT.

We provide microwave excitation within a 250 MHz frequency range starting at frequency f_S with power P_{irr} . f_S is varied from 1 to 9.25 GHz and at each f_S , P_{irr} is increased in steps of 1 dBm from -25 to 6 dBm. At each power step, after irradiation, a sensing measurement is conducted to probe whether there is a modification in reflection and transmission spectra. The sensing measurement is performed with -25 dBm within 3 to 7 GHz thus monitoring the first GC mode branch (Fig. 4.6a,b). The AP and P branch signal strength is integrated as a function of P_{irr} at each irradiation steps. The integrated signal strength values are summarized in the *switching yield diagram* as a function of P_{irr} and f_{irr} (Fig. 4.6c-f). In panel (c)-(f) we

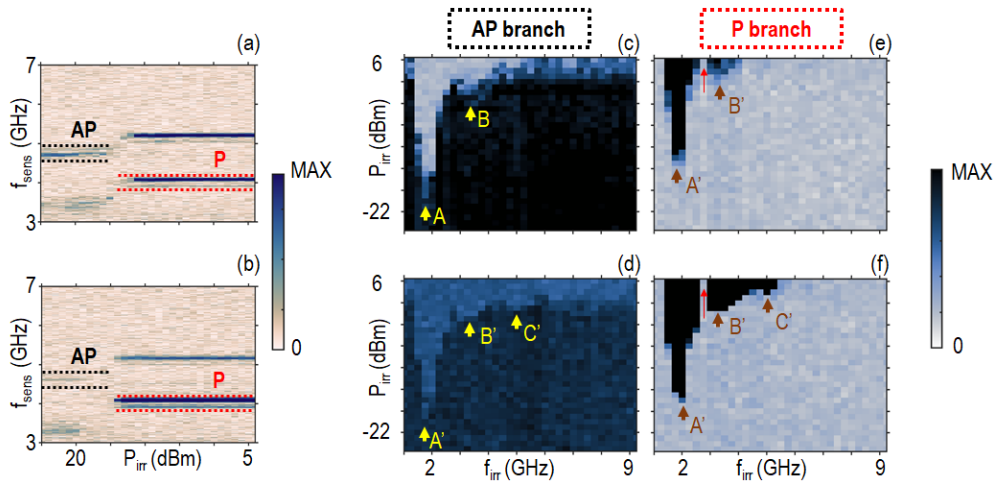


Figure 4.6: Sensing protocol measurements of $\text{Mag}(S_{21})$ for *sample_Cu* and *sample_SiO₂* at 14 mT for the irradiation interval $(1.75 \div 2)$ GHz, i.e. $f_s = 1.75$ GHz. Branch P (AP) is integrated at each P_{irr} within the red (black) dotted sensing frequency band. (c)-(f) Switching yield maps for the AP branch [P branch] for (c) *sample_Cu* and (d) *sample_SiO₂* [(e) *sample_Cu* and (f) *sample_SiO₂*]. (c)-(f) Irradiation frequencies corresponding to dips (peaks) in the integrated signal are indicated in yellow (brown) letters. From AP branch data we extract P_{C1} and from P branch the critical power P_{C2} as a function of f_{irr}

have highlighted the dips (peaks) of the AP (P) branch signal with yellow (brown) arrows and letters. These indicate the f_s values for which P_{irr} takes local minima for inducing reversal.

In Fig. 4.6 we call these power levels P_{C1} . We observe that in *sample_SiO₂* (Fig. 4.4b,f) three different frequencies A', B' and C' lead to local minima in P_{irr} for magnon-induced switching. We attribute these frequencies to three different magnon modes in YIG with wave vectors k_1 , $k_1 + G$ and $k_1 + G + k_{\text{PSSW1}}$, respectively. k_{PSSW1} identifies the first magnon mode across the YIG thickness. For *sample_Cu* we observe two frequencies A' and B' in Fig. 4.6c,e, which, we assume, correspond to k_1 and $k_1 + G$ modes, respectively. From the AP branch in Fig. A.3 we extract the critical power P_{C1} needed to reverse stripes particularly under the emitter CPW (CPW1). From the P branch data, we extract the critical power P_{C2} needed to reverse stripes underneath CPW2. The critical power levels P_{C1} (P_{C2}) are taken as a function of f_{irr} when AP (P) branch intensities decrease (increase) by 50%. The uncertainty in the power values is ± 1 dBm and corresponding to the power step during in the measurements.

Figure 4.7 shows the comparison for *sample_Cu* and *sample_SiO₂* of the critical powers characterizing the magnon-induced switching efficiency at the detector. We compute the actual power that is delivered to spin precessional motion $P_{C2,\text{prec}}(f_s) = P_{C2}(f_s) \cdot [\text{Mag}(S_{11}(f_s))]^2$ [133]. Figure 4.4a and b show the values $[\text{Mag}(S_{11})]^2$ at relevant frequencies for 2 and 3 field values, respectively. Fig. 4.4c and d show the values for P_2 for the two samples. In both cases, the overall trend is that P_{C2} is larger for larger f_{irr} at a fixed field. For a given SW mode, a smaller bias field leads to larger power. This observation is attributed to the larger energy

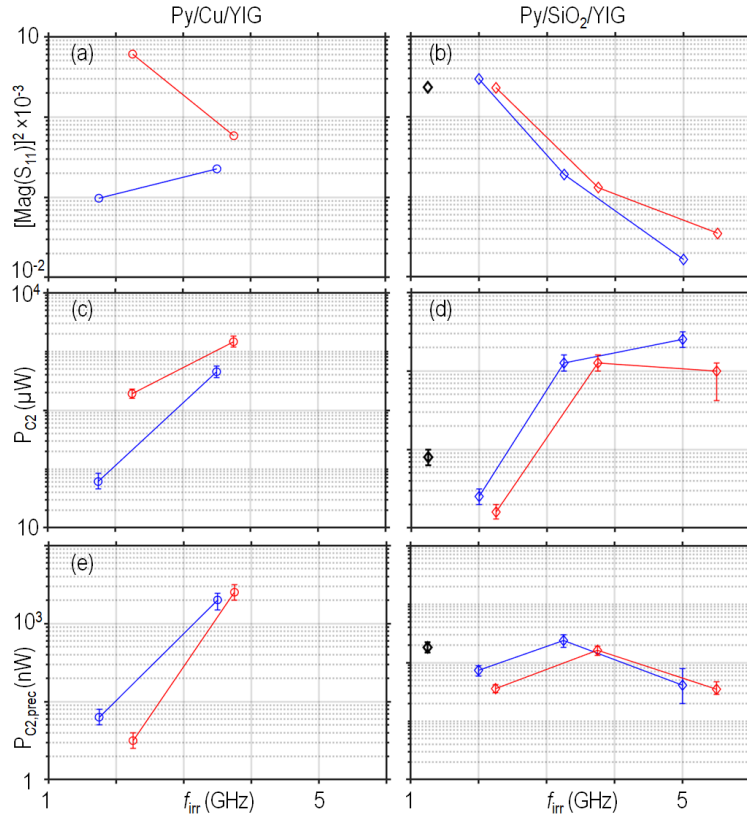


Figure 4.7: (a-b) $\text{Mag}(S_{11})$, (c-d) P_{C2} , (e-f) $P_{C2,\text{prec}}$ are reported for both *sample_Cu* (left column, circles) and *sample_SiO₂* (right column, diamonds) at 2 (black), 14 (blue) and 20 (red) mT.

barrier for reversal at a smaller bias field. Figure 4.4e and f show the values for $P_{C2,\text{prec}}$ for different fields and different f_{irr} . Here the data suggest that the intermediate layer SiO₂ is advantageous for reversal triggered by GC modes. Hence for the same field and same magnon mode, less power is needed to initiate switching in *sample_SiO₂*. The precessional critical power $P_{C2,\text{prec}}$ in *sample_SiO₂* decreases with increasing field while it shows non-monotonic behavior with increasing frequency (for the same field). A large value $P_{C2,\text{prec}}$ is recorded at the first GC mode, for both samples. In *sample_Cu* we observe a different trend in that $P_{C2,\text{prec}}$ at 14 mT is smaller than the value at 20 mT. In Fig. 4.4b $\text{Mag}(S_{11})$ decreases for *sample_SiO₂* with increasing frequency for the same field. In *sample_Cu*, $\text{Mag}(S_{11})$ shows a larger variation as a function of field, it increases (decreases) with the frequency at 14 mT (20 mT).

In the following we discuss two BLS experiments, one with *sample_Cu* and one with *sample_SiO₂*. By BLS we probe locally the magnetic state of Py stripes leveraging the spatial (~ 250 nm) and temporal (pulsed excitation) resolution of the microfocus BLS setup.

4.1.3 Multi-frequency magnon-assisted nanomagnet reversal resolved by micro-focus BLS

In this section we spatially resolve the changes in the Py magnetic state after magnon propagation in *sample_Cu*. For this we measure locally magnon spectra using micro-focus BLS (μ BLS). The field is applied along the CPW longitudinal axis, i.e. y direction in Fig. 4.8, to reproduce the VNA measurement conditions. In the experiment the system is initialized at -90 mT and the field is gradually increased to $+2$ mT thus preparing the nanostripes in an the antiparallel (AP) state as discussed for the VNA measurements. The magnetic state of Py stripes is probed by measuring the resonance frequencies of thermally excited magnons (*thermal magnons*) in Pos2.1 and Pos2.2 (Fig. 4.8b,c). Following the LLGE equation (Eq. 2.19) the resonance frequency reflects the orientation of the vector \mathbf{M} and the strength of the effective field. Then the system is irradiated with microwaves at $f = 1.25$ GHz thus exciting the k_1 magnon mode, i.e. the main CPW-induced mode, propagating through YIG (Fig. 4.8d). Thermal magnons spectra before/after irradiation (black/red curves in Fig. 4.8) are measured and compared. In Pos2.1 (Fig. 4.8b) the thermal magnon spectrum after irradiation (red curve) shows one broad peak at ≈ 5 GHz and one at ≈ 6.6 GHz (indicated by red arrows) that we do not observe in the spectrum before irradiation. We interpret this as a signature of a change in \mathbf{M}_{Py} , i.e. the magnon-induced reversal. Such modification of the magnon spectra is not observed in Pos2.2 which is $\approx 3.5 \mu\text{m}$ further away from the SW emission region than Pos2.1. We attribute the different behavior to the decaying amplitude of magnons. The selected irradiation frequency of 1.25 GHz (green line in Fig. 4.8d) is, at 2 mT above the magnon band gap, thus exciting a propagating spin wave (SW).

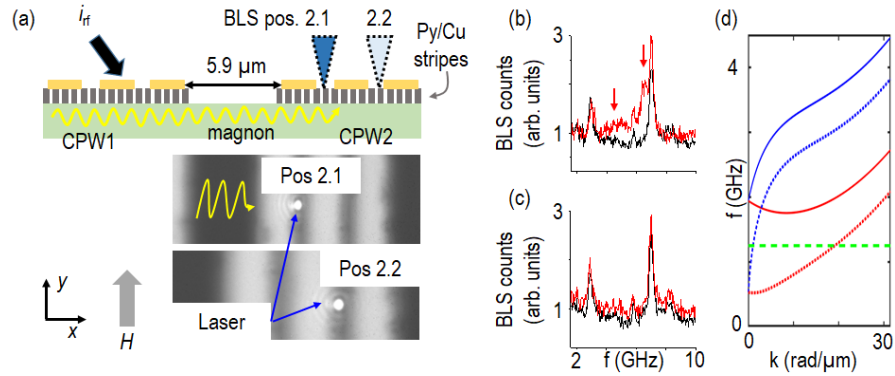


Figure 4.8: (a) Graphical cross section view of the experiment. Pos2.1 and 2.2 on the Py stripes below the detector CPW are probed with the laser. RF current is injected into CPW1, this excites magnons, when the RF frequency matches the magnon band. Camera images of the Pos2.1 and 2.2 in the BLS setup. (b),(c) BLS thermal magnon spectra in Pos2.1 and 2.2, respectively, at 2 mT. Before (after) continuous-wave irradiation at 1.25 GHz the spectrum is shown in black (red). (d) KS model evaluated at 2 mT (24 mT) in dashed (solid) lines for DE (blue) and BV (red) configuration. The green dashed line indicates 1.25 GHz.

In a second experiment, we increase the field to $+24$ mT (after firstly re-initializing the system at -90 mT). At $+24$ mT the system has still the AP state configuration. Here the magnon band-

structure in YIG is shifted to higher frequencies. Therefore 1.25 GHz falls into the magnon band gap (Fig. 4.8d). At 24 mT we repeat the same experimental protocol as for the investigation at 2 mT. We step the power up to 16 dBm and apply the high power RF signal for 2 hours. Still, in Fig. 4.9a,e no significant changes are found in the after spectrum compared to the spectrum before. The small excitation frequency of 1.25 GHz is not able to excite a SW at 24 mT, and the Py stripes in the BLS focus do not change their AP state, though the bias field is close to the coercivity field. This measurement helps rule out heating of the CPW as main cause of the observed magnetization reversal.

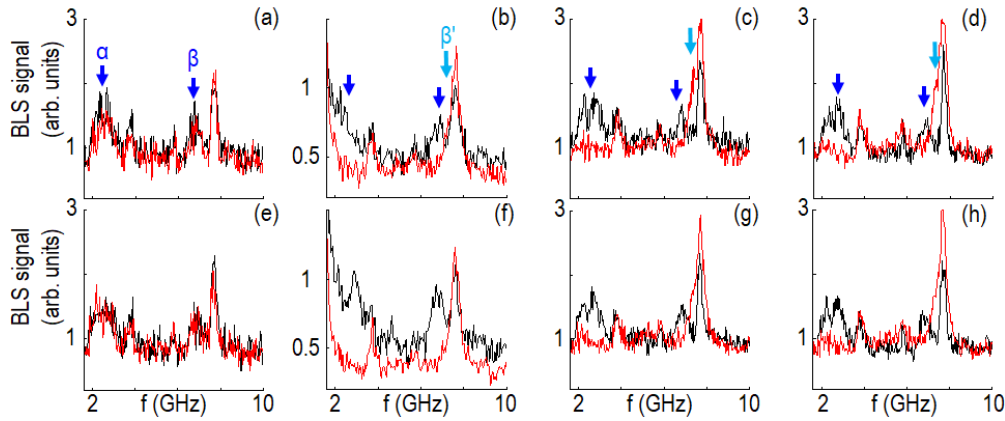


Figure 4.9: Thermal magnon spectra at 24 mT in (a)-(d) Pos 2.1 and (e)-(h) Pos2.2 probed in the μ BLS microscope. The black (red) spectra are acquired before (after) irradiation with microwaves for 2 hours at 16 dBm (uncalibrated value) at 1.25 [(a),(e)], 2.3 [(a),(e)], 4.3 [(a),(e)] and 5 [(a),(e)] GHz. The blue arrows indicate the peaks in the 'as-prepared' state before irradiating with microwaves. The cyan arrow indicates the peak that originates after irradiating with microwaves.

In Fig. 4.9 we explore the effects of further magnon modes at different f : a dipolar magnon mode (k_1), a dipole-exchange mode (1st GC mode, GC1) and parametrically pumped magnons. At each frequency, RF irradiation starts at -20 dBm. Then the power is increased in steps up to 16 dBm (39.8 mW). At each applied power level the irradiation and measurement last 2 hours. We record magnon spectra while the excitation is on and after. Figure 4.9 summarizes the results for the thermal magnon spectra at +24 mT. The peaks labelled α and β will be analyzed in the following to evaluate the effect of RF signals of higher frequencies. When the frequency is at 2.3 GHz (corresponding to magnons with wave vector k_1) the α and β peaks vanish after irradiation and a new peak β' is observed afterwards (Fig. 4.9b,f). The same modifications of spectra are observed after irradiating the sample at 4.3 GHz and 5 GHz.

We find that the disappearance of peaks α and β and the appearance of peak β' occur at different power levels depending on which magnon mode induces the switching (consistent with the VNA observations and switching yield diagram). Importantly, magnon-induced reversal is achieved by multiple magnon modes and depending on their frequency a different power is needed to be pumped into the CPW.

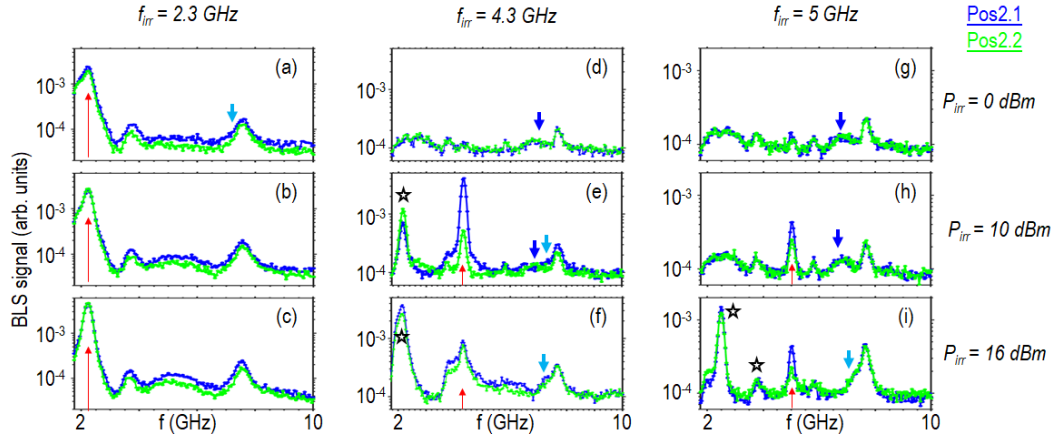


Figure 4.10: The blue (green) BLS spectra are recorded in Pos 2.1 (Pos 2.2) at 24 mT while the continuous wave excitation is on. (a)-(c) BLS spectra are shown while irradiating the sample at 2.3 GHz at increasing power as indicated on the right side of the panels. (d)-(f) [(g)-(i)] BLS spectra during irradiation at 4.3 GHz [5 GHz]. The red upward arrows indicate the directly excited magnon modes. The blue (cyan) downward arrows indicate the Py resonance in the AP (P) state. The star symbols identify the parametrically pumped mode. Each BLS spectrum is integrated for 2 hours. The irradiation lasts for the same duration.

We show in Fig. 4.10 the BLS spectra that were acquired during microwave irradiation at increasing powers for different frequencies. For 2.3 GHz and 0 dBm the peak β is not seen in panel (a) but peak β' is observed. We consider the spectrum to reflect the P state, i.e. magnon-induced switching has happened. For the same power of 0 dBm at higher excitation frequencies peak β is still present indicating the AP state (Fig. 4.10d and g). At 4.3 GHz irradiation, peak β disappears at Pos2.1 for $P_{\text{irr}} = 10$ dBm but not in Pos2.2. We assume that the magnon amplitude reaching Pos2.2 was below the threshold for switching. For $P_{\text{irr}} = 16$ dBm no spectrum shows peak β at the two positions independently of f_{irr} .

In panels (e)-(f) and (h)-(i) of Fig. 4.10 the red arrows indicate the directly excited modes whereas the black stars identify the parametrically pumped mode. Both pumping frequencies $f_p = 4.3$ and 5 GHz are such that when the power is large enough to trigger non-linear dynamics these modes scatter to magnon states at $f = \frac{1}{2} f_p$ which overlaps with the k_1 mode. In (e) the directly excited mode has still much larger (≈ 5.8 times) intensity than the parametrically pumped mode and most likely induces the reversal to the P state in Pos2.1. At 5 GHz, the correspondingly modified magnon spectra of Py stripes are observed only after efficient excitation of the parametrically pumped mode corresponding to the non-linear excitation of k_1 mode. The electromagnetic crosstalk (EMC) is estimated by extracting the signal strength of the raw S_{21} linear magnitude measured by the VNA at 2.3 GHz and 4.3 GHz for an applied magnetic field of 2 mT such that we are not in resonance with any magnon mode. The raw S_{21} linear magnitude is the raw VNA measurement hence no postprocessing procedure is applied. We measure an EMC of -38 dB and -31 dB at 2.3 and 4.3 GHz respectively. Via BLS experiment we experimentally find that irradiation at 1.25 GHz inside the spin wave gap for 2 hours at 16

dBm (uncalibrated power) does not lead to switching. Further control measurements have also been conducted in Ref. [133]. Based on all these control measurements we exclude that the CPW Oersted field leads to the observed switching phenomenon. The presented set of BLS experiments shows that Py switching is indeed triggered by different magnon modes. These findings are promising for SW signals in multi-frequency magnonic circuits.

4.1.4 Magnon-assisted nanomagnet reversal by magnon pulses with μ BLS

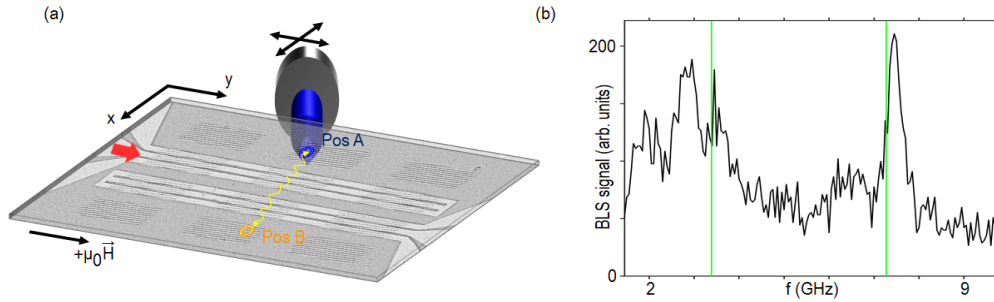


Figure 4.11: (a) Graphical view of μ BLS performed through the transparent substrate. Two positions are probed Pos A (dark blue) and B (orange). The RF signal is injected in the left CPW indicated by the red arrow. The magnetic field is applied along the longitudinal axis of the CPW. (b) The system is in the AP state. Thermal magnon BLS signal at 20 mT for the AP state (i.e. the *as-prepared* state). The first (second) PSSW is indicated by the green line at 3.4 GHz (7.3 GHz).

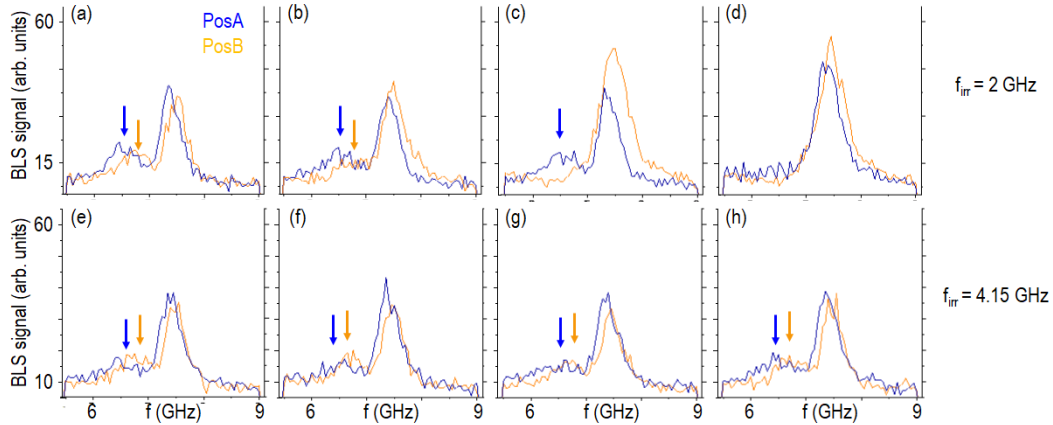


Figure 4.12: Thermal magnon spectra at 20 mT measured by μ BLS on Pos A (Pos B) are shown in dark blue (orange) after a pulsed RF signal has been applied at (a)-(d) 2 GHz and at (e)-(h) 4.15 GHz. The pulse lasts 70 ns and has a 1 μ s repetition rate. The provided RF power in the pulsed excitation is -10 dBm (a,e), -5 dBm (b,f), 0 dBm (c,g) and 5 dBm (d,h). The blue and orange arrows indicate the presence of peak β .

Using *sample_SiO₂* we explore nanostripe-reversal by magnon pulses. The laser is focused through the GGG so that all the YIG can be accessed avoiding the laser beam being blocked

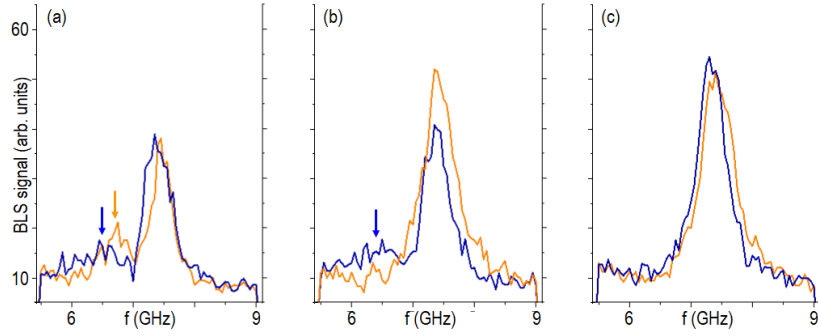


Figure 4.13: BLS thermal magnon spectra at 20 mT for Pos A (Pos B) in dark blue (orange) after pulsed RF irradiation at 4.15 GHz with further increased power. This is a continuation of the dataset shown in 4.12e-h. The pulse power is 10 dBm (a), 15 dBm (b) and 20 dBm (c).

by the CPWs (Fig. 4.11a). The laser focus diameter is again about 250 nm such that at least one Py stripe is measured. The sample is initialized at -65 mT large enough to saturate the Py stripes and then the field is gradually increased to +20 mT. Figure 4.11b illustrates a thermal magnon spectrum obtained by μ BLS when focusing the laser on an area with Py stripes. The signal between 1.5 and 4.1 GHz is attributed to the magnon band minimum, the first resonant mode in DE configuration and the first PSSW mode (at ~ 3.4 GHz). At ~ 6.5 GHz we observe another broad peak attributed to the Py resonance and at ~ 7.3 GHz the strong and sharp peak is attributed to the second PSSW by comparison with the KS model. There is a small frequency shift between the peak frequencies and the ones predicted by the KS model for bare YIG. The hybrid system is such that the stripes modify the internal field in YIG locally via their dipolar stray fields, whereas the KS model assumes a uniformly magnetized thin film. Additionally the magnetic field calibration may not be precise.

In the following we discuss thermal spectra from 5.5 to 9 GHz covering the Py resonance that are acquired in Pos A and B. The distance between PosA (B) and the nearest CPW ground line edge is $d_A \approx 7.19 \mu\text{m}$ ($d_B \approx 22.1 \mu\text{m}$). The DE non-reciprocity favors magnon propagation along $+x$, i.e. towards B. After preparing the system in the AP state we start at a power $P = -10$ dBm to inject RF pulses at 2 GHz (i.e. k_1 mode). The RF pulse is on for 1 seconds. The pulse repetition period is $1 \mu\text{s}$ and the pulse width is 70 ns. Hence in the experiment 10^6 magnon pulses are emitted. For each experiment the power is increased by 5 dBm. At each power step we record the thermal magnon spectra in Pos A and B (Fig. 4.12a-d). At low powers (panel a,b) we observe two peaks that we attribute to the Py signal in AP state (i.e. peak β of Fig. 4.9) and the second YIG-PSSW. For power $P = 0$ dBm (Fig. 4.12c) the peak β is absent in Pos B whereas it is still present in A. This suggests that magnons have led to nanomagnet reversal in Pos B but not in A. We attribute this result to a difference in magnon amplitudes due to the non-reciprocity when magnons propagate in opposite directions. Here, the second YIG-PSSW mode shows larger intensity. This comes from the fact that now this resonance partially overlaps with the Py peak that has shifted to higher frequency in the P state. At $P = 5$ dBm, peak β is absent also in A (Fig. 4.12d).

We conduct the same experiment with pulse irradiation at $f_{\text{irr}} = 4.15$ GHz which coincides with the first GC mode of the device in P state. In Fig. 4.12e-h the same power levels that have been discussed for $f_{\text{irr}} = 2$ GHz are investigated. No modifications are observed in the thermal magnon spectra up to $P = 5$ dBm, i.e. the peak β indicating the AP state is present in each panel e-h. Then we increase the power to 10, 15 and 20 dBm (Fig. 4.13) and observe the first change in thermal magnon spectra in B for $P = 15$ dBm. At $P = 20$ dBm peak β is absent in both Pos A and B. These results provide evidence that, with large enough power, dipolar magnons and GC modes propagating in opposite directions assist in the magnetization reversal of remotely located nanomagnets. The threshold amplitude for switching could be reached in both directions.

Throughout this work micromagnetic simulations have been conducted to analyse further the magnon-induced switching mechanism and to support a deeper microscopic understanding of the mechanism. We have not been able to reproduce such phenomenon in micromagnetic simulations. Possible reasons behind this could be related to roughness of stripes' edges and surface roughness at the interface between Py and the underlying YIG.

4.2 Inductive spectroscopy of LPE-grown 11-nm-thick YIG

In this section we investigate the magnetization dynamics of 11-nm-thick YIG layer with integrated Py stripes. To the best of our knowledge, this is the first report on coherent magnetization dynamics of liquid-phase-epitaxy (LPE) grown 11-nm-thick YIG exploring propagation of magnons with wavelengths down to 99 nm. To realize chiral nanomagnonics [114], ultra-thin magnetic layers are important which exhibit low magnon damping and interfacial DMI (iDMI). Recently, group velocities of counterpropagating spin waves were found to be asymmetric in magnetron-sputtered 7-nm-thick yttrium iron garnet (YIG). This observation was made on mainly long-wavelength magnons and attributed to iDMI arising at the interface between YIG and the garnet substrate [114]. To advance the frontiers of chiral nanomagnonics it is now important to study short-waved magnon propagation in the presence of iDMI and in LPE-grown YIG. Therefore the investigation of short-waved magnons excitation and detection in ultra thin YIG layer is performed. Furthermore we are motivated to explore the thickness dependence of magnon-induced reversal. Therefore we fabricate one-dimensional Py grating couplers on top of the 11-nm-thick YIG. CPWs were patterned onto the Py nanostripes to excite spin waves via RF magnetic fields. The device design is identical to those fabricated on the thick YIG. Here the focus is to understand the role played by the thickness of the YIG in the magnon-induced reversal of nanomagnets. We also explore the role of interfaces in that on the same chip. We prepare the same Py/YIG hybrid structures without (*device type A*) and with (*device type B*) a 5-nm-thick SiO₂ spacer.

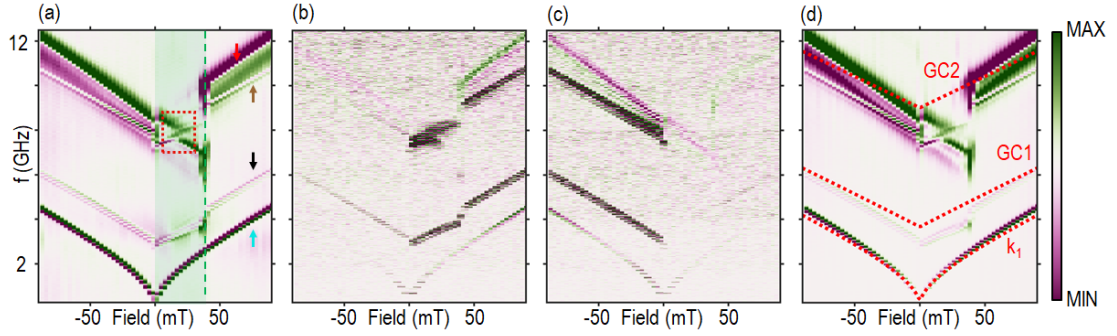


Figure 4.14: AESWS spectra taken at -9dBm for a device type B. Neighboring-subtracted (a) S_{11} , (b) S_{21} , (c) S_{12} and (d) S_{22} signals. (a) The red dashed box indicates the region of the avoided crossing. The Py resonance is indicated by the arrow. k_1 , GC1 and GC2 modes are indicated respectively by the cyan, dark blue and brown arrows. The green shaded area is the field range within which the stripes are antiparallel to the YIG. (d) The red dashed lines identify the k_1 , GC1 and GC2 mode as predicted by KS model.

4.2.1 Field-dependent VNA spectra and avoided crossing

In Fig. 4.14 the spectra are taken at -9 dBm sweeping the field from -90 to +90 mT with 3 mT steps. The VNA setup is configured to measure S_{12} and S_{21} with equal signal-to-noise ratio (SNR) such that chiral propagation properties can be extracted. In reflection (Fig 4.14a,d) we observe several branches at negative fields and above +38 mT. In the framework of the KS formalism we interpret these branches to be indicative of the Py resonance (red arrow), first and second GC modes (brown and black arrow) and the k_1 mode (cyan arrow). Due to its small thickness, the YIG-PSSW is expected above 100 GHz and not observed. Crossing zero field leads to an AP state of Py as observed for the thicker YIG. This field region (green shaded rectangular box) exists up to 40 mT. Here, three main branches are observed in reflection. Interestingly, we find an avoided crossing at 18 mT between two magnon modes that we assume to be the fundamental Py mode and the second GC mode (GC2). We observe avoided crossings for devices with interfaces Py/YIG and Py/SiO₂/YIG. We attribute the origin of avoided crossings to dipolar coupling effect between the Py fundamental mode and the GC2 mode in YIG.

The frequencies predicted by the KS model (red dashed lines in Fig. 4.14d) for 11-nm-thick YIG are shown on top of the reflection spectrum. The model assumes a homogeneously magnetized thin film and the Damon-Eshbach mode. The model describes well the dipolar mode k_1 and the first GC mode (GC1) of the P state. However GC2 is overestimated by a constant offset of ~ 2 GHz. The slope of the branch is well reproduced. As the experimentally observed branch lies at lower frequencies than the model (for the same external field) we suggest that the stray field of Py stripes modifies the internal field in YIG. The intermixing zone of YIG with the GGG substrate is reported to be (1.9 ± 0.4) nm [110]. The intermixing zone might induce also an internal field variation and modify the spin pinning boundary condition. They are known to shift the resonance frequency [16].

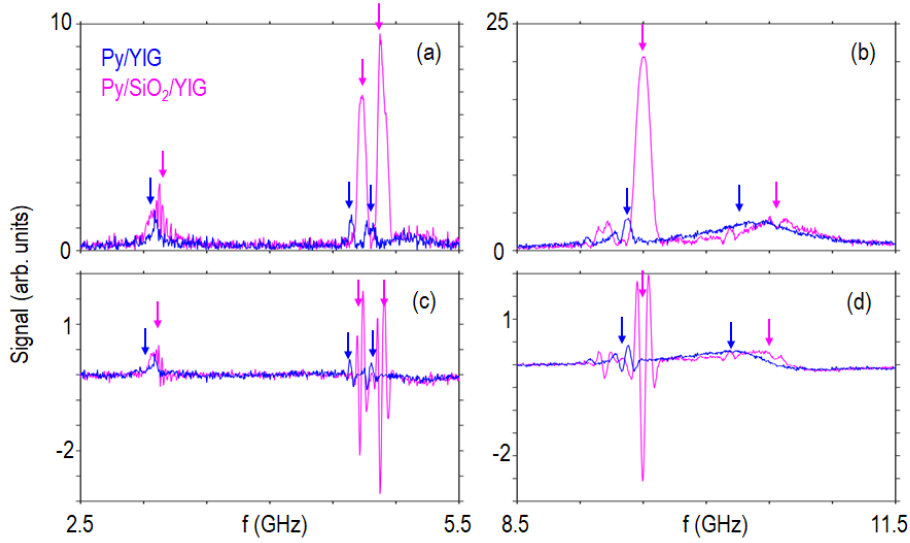


Figure 4.15: (a),(b) $\text{Mag}(S_{21})$ and (c), (d) $\text{Imag}(S_{21})$ at +50 mT measured for sample A (blue) and B (magenta). Resonances are shifted to larger frequencies in sample B. The magenta and blue arrows indicate the magnon resonances.

For samples (A) Py/YIG and (B) Py/SiO₂/YIG in Fig. 4.15 we report spectra showing the k_1 , GC1 and GC2 resonances. The two peaks between 4.5-5 GHz in Fig. 4.15a (indicated by the arrows) are interpreted as $G + k_1$ and $G - k_1$ modes and the frequency discrepancies are ≈ 86 MHz and 96 MHz from sample A to B. The low-frequency mode at ≈ 3 GHz is the k_1 resonance. In Fig. 4.15b the $2G + k_1$ and $2G - k_1$ modes and the Py fundamental mode are shown. Here their frequency differences between the two devices amount to ≈ 160 MHz, 134 MHz and 173 MHz respectively. The frequencies are smaller in Py/SiO₂/YIG compared to Py/YIG. The oscillatory signals in the imaginary part of the transmission spectra in Fig. 4.15c,d are attributed to magnon resonances. The reason behind the observed oscillations is explained in paragraph 3.2.3 (equation 3.4). Assuming dipolar effects to modify the internal field in YIG, the 5-nm-thick SiO₂ might reduce the coupling between Py and YIG and lead to a larger internal field in YIG.

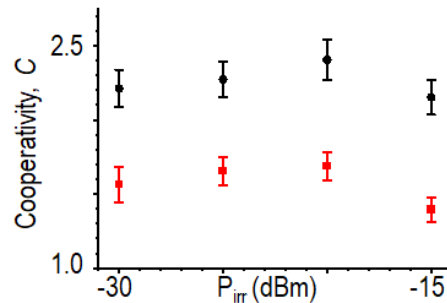


Figure 4.16: Cooperativity as a function of P_{irr} for sample A (black dots) and B (red squares).

For the field of 18 mT that induces the avoided crossing (box in Fig. 4.14) we extract the

coupling strength g between the two coupled modes, namely the fundamental Py mode and the GC2 mode in YIG. We extract at -2 mT the linewidths of the resonant modes when they have the same frequencies as in +18 mT. In doing so we estimate the dissipation rate of each isolated magnon mode κ_{Py} and $\kappa_{\text{GC2,YIG}}$. Then we evaluate the cooperativity C (see section 2.9). The results for devices A and B are reported in Fig. 4.16. Cooperativity is extracted at different irradiation powers. The average of all the measurement yields in sample A (B) a cooperativity $C = 2.26 \pm 0.11$ ($C = 1.57 \pm 0.13$). Hence cooperativity is larger for sample A that features both exchange and dipolar coupling at the Py/YIG interface. Both samples are in the intermediate coupling regime with $C > 1$ and $\kappa_{\text{Py}} > g > \kappa_{\text{GC2,YIG}}$ [137]. We believe that the observed constant trend of C as a function of P_{irr} is due to the fact that for the reported power levels the effect of nonlinearities is still weak. We have extracted the cooperativity for larger powers and observed a reduction of C . We suggest that this reduction could be explained by multi magnon scattering processes that lead to an increased broadening of the magnon modes by increasing the dissipation rates. This is in agreement with recently published findings where Lee et al. [136] report avoided crossing gap closing beyond a threshold power due to the Suhl instability of the Kittel mode in YIG. For our sample with iDMI the three magnon scattering at large enough powers might play a role as well[103].

4.2.2 Magnon-assisted switching: switching field distribution and switching yield diagram

The magnon switching efficiency is characterized at different magnetic fields. To conduct these experiments we inject RF currents in CPW1 and measure S_{11} and S_{21} . The reflection and transmission spectra respectively are shown in Fig. 4.17. We consistently observe a stronger transmission intensity for the sample B incorporating the SiO₂ barrier layer. The spectra qualitatively resemble to what has been observed in the 113-nm-thick YIG: they contain several branches that we attribute to GC1 and GC2, the Py fundamental mode and the main CPW-induced mode. We focus now on the fields highlighted by the dashed red line at which switching from the AP state is completed and the P state is established. The data suggest that the switching is accomplished at much higher fields and powers than observed on the 113-nm-thick YIG.

To extract the switching field distribution we focus on the high-frequency branch. The methodology is described in chapter 4.1. At -25 dBm the switching field distribution extends from 24 to 41 mT for sample A and from 29 to 46 mT for sample B. The switching field distribution is weakly dependent on P_{irr} (Fig. 4.18). At 3 dBm the distribution tends to become narrower for the sample A. The lowest recorded field for switching is 16 mT. In general the distribution is broad and approximately constant over the power range that we probe. For $P_{\text{irr}} > -2$ dBm, $\mu_0 H_{\text{C2}}$ moves to slightly smaller values. For sample A we notice that the switching field distribution narrows to a few mT centered at ~ 34.5 mT at high power. The switching field distribution for the sample B remains broader. This could be a consequence of adding a spacer layer between Py and YIG.

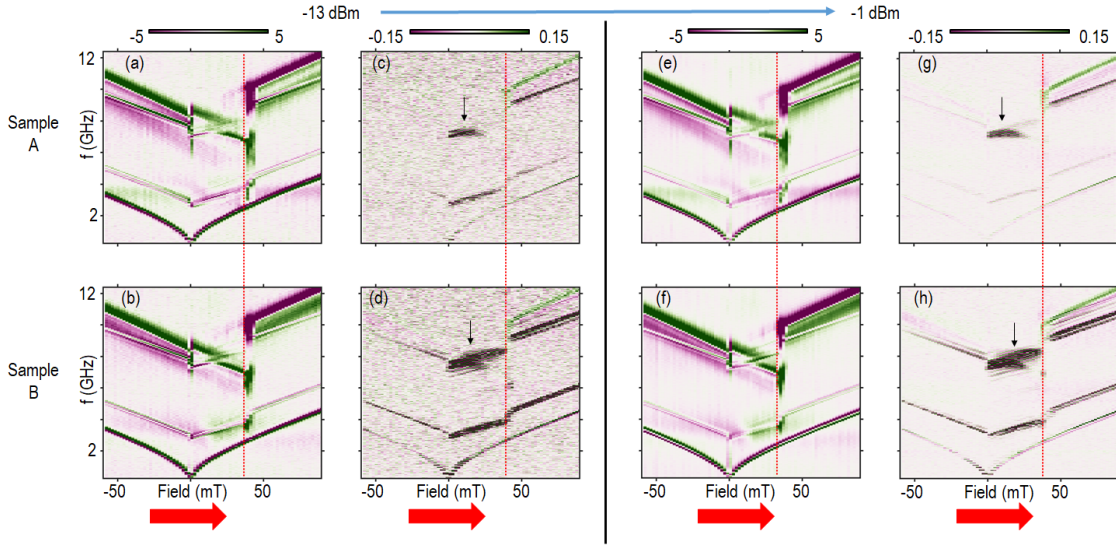


Figure 4.17: VNA measurements at -13 dBm (a-d) and -1 dBm (e-h). Neighbor-subtracted S_{11} and S_{21} respectively for sample A (a,c,e,g) and B (b,d,f,h). The solid red line at the bottom of the panels indicates the field sweep direction. The vertical dashed red lines in the graphs is a guide for the reader’s eye to appreciate tiny shifts in the critical field when comparison different powers and different interfaces A, B. The vertical black arrow in the transmission graphs (b,d,g,h) indicate GC2 in the AP state showing a broader and stronger response for sample B (d,h).

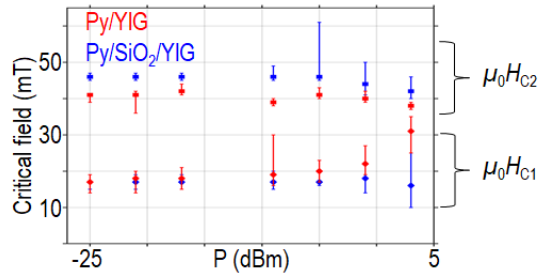


Figure 4.18: Switching field distribution for sample A (B) in red (blue).

Now we discuss the switching yield for the 11-nm-thick YIG sample. The methodology is discussed in [133] and in chapter 4.1. We analyse switching at 34 and 38 mT for the stripes beneath the emitter to evaluate the critical power P_{C1} . Considering the reduced YIG magnetic volume and larger coercivity of the stripes we use -20 dBm as the sensing power and set the power sweep from -20 to 9 dBm. The sensing window is 3-7 GHz. We provide microwave irradiation within a 250 MHz frequency range starting at f_S . Overall f ranges from 1 to 9.25 GHz. We find that the lowest power to initiate switching is -11 dBm (0.776 mW) at 38 mT. We identify three local minima in Fig. 4.19. We attribute the three minima to the k_1 mode, GC1 and the Py mode (at 6.5 GHz). Switching at this frequency is a known effect as MAS [29]. This is different from the magnon-assisted switching that occurs at the low frequencies ~ 2.5 (k_1) and

3.5 GHz (GC1). The latter frequencies are not resonant with the Py dynamics. The bias field of 34 mT is already close to the quasistatic switching field of the stripes. Still, for both devices we observe that relatively large powers are needed to switch nanomagnets independently of the frequency. We suggest that this observation can be explained by (i) the locally varied internal field in 11-nm-thick YIG due to the Py stripes and by (ii) the coupling of magnon modes between Py and YIG in the AP state.

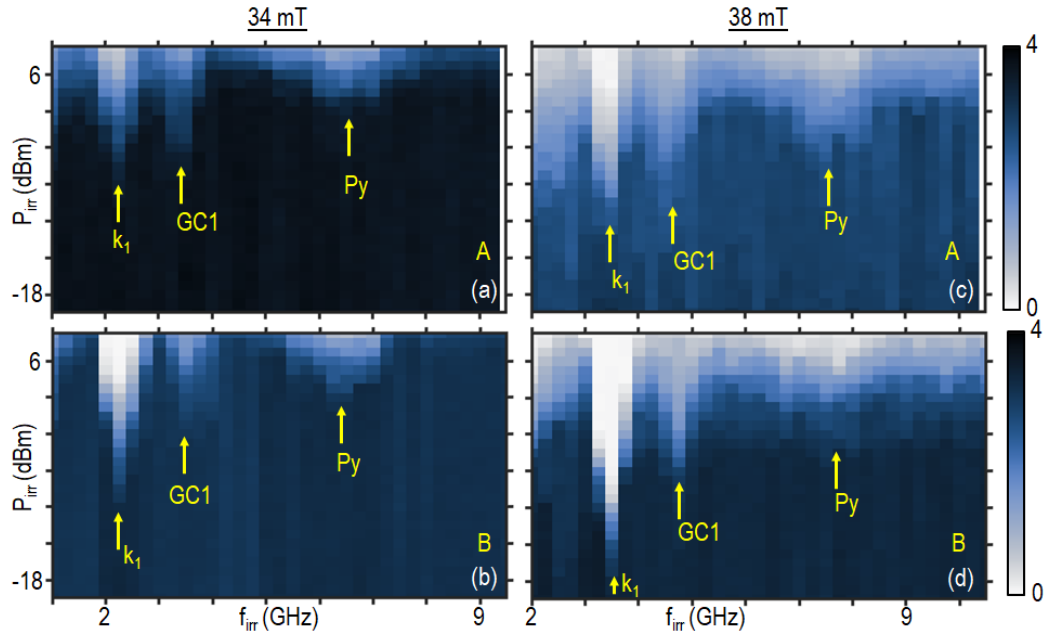


Figure 4.19: Switching yield diagram at 34 mT (a),(b) and 38 mT (c),(d) studying the reversal of stripes below the emitter CPW. Results for sample A [B] are shown in panels (a),(c) [(b),(d)]. The yellow arrows indicate the frequency values that are analyzed in terms of switching yield efficiency.

In Fig. 4.20 we summarize the switching efficiencies. The critical power increases with the frequency (Fig. 4.20a). The slope is steeper for sample B than A. It features one order of magnitude lower powers at low frequency. The efficiency in sample A it is within error bars constant and more power is needed than in B. The actual power that goes into the spin precessional motion of the system is shown in Fig. 4.20b. The most efficient switching occurs at k_1 for sample B. The power P_{Clprec} is only 50 nW. MAS is less efficient by at least a factor of 2.

4.2.3 Amplitude non-reciprocity, chiral magnon propagation and iDMI estimation

In the following we report spectra obtained for counterpropagating magnons observed on the same 11-nm-thick YIG and excited by two different grating couplers based on either Py/YIG or Py/SiO₂/YIG. The signal non-reciprocity for sample A and B is characterized for different power levels at +12 mT in the P state. An exemplary dataset taken at -13 dBm is reported in

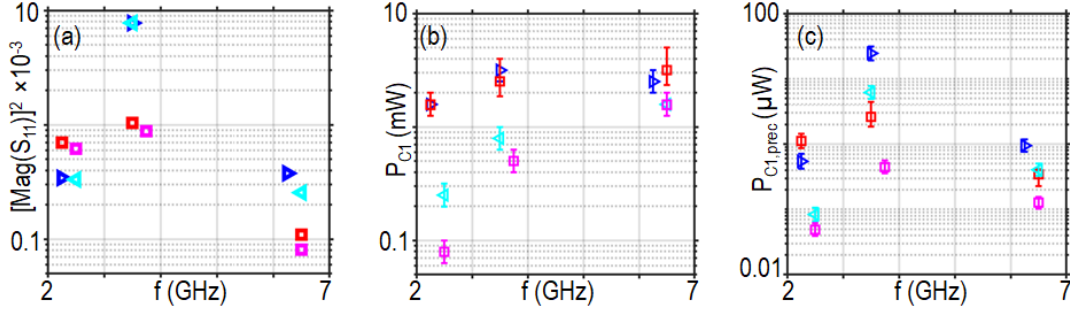


Figure 4.20: (a) P_{C1} , (b) $P_{C1,prec}$ and (c) $\text{Mag}(S_{11})$ for sample A (B) at 34 mT in blue (cyan) and at 38 mT in red (magenta).

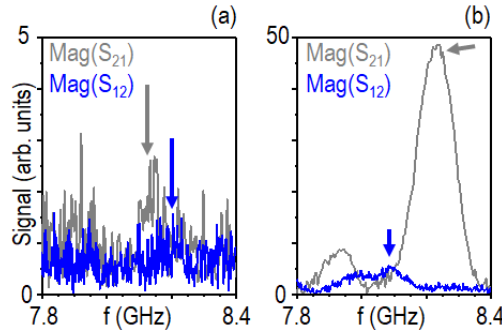


Figure 4.21: $\text{Mag}(S_{12})$ and $\text{Mag}(S_{21})$ are respectively illustrated in grey and blue for (a) sample A and for (b) sample B. The measurements are taken at $P_{\text{irr}} = -13$ dBm.

Fig. 4.21. We fit a Lorentzian to the GC2 resonance to extract the signal amplitude that is utilized to calculate η with Eq. 3.6. We calculate η for $P_{\text{irr}} = -13, -9$ and -5 dBm. The results are summarized in table 4.1:

$P_{\text{VNA}} =$	-13 dBm	-9 dBm	-5 dBm
sample A	(0.816 ± 0.205)	(0.889 ± 0.198)	(0.698 ± 0.177)
sample B	(0.971 ± 0.040)	(0.994 ± 0.022)	(0.923 ± 0.044)

Table 4.1: Non-reciprocity η for the GC2 magnon resonance. The value $\eta = 1$ indicates unidirectional spin-wave emission by a CPW.

In sample B, η reaches 0.971 compared to 0.816 for sample A. We note that for the direct interface Py/YIG similar values to sample A have been reported in [114] for 10-nm-thick YIG. We achieve $\eta = 0.971$ for the magnon mode with k (λ) = 63.7 rad/ μm (99 nm). Such high non-reciprocity is expected [105] when chiral spin wave pumping is active. The high non-reciprocity is indicative of exchange-dominated magnons. In the limit of perfectly right-circular polarization the magnon chirality becomes 1. This value means perfect unidirectional excitation of magnons by the stripe array.

Next we focus on characterizing the magnon group velocity v_g in sample A and B at different powers. Following [114], [77] and [58] we measure S_{12} and S_{21} at the same field. For the same resonant magnon mode we compare the group velocity extracted from the two counterpropagating magnons. We study the signals when the system is in the P state.

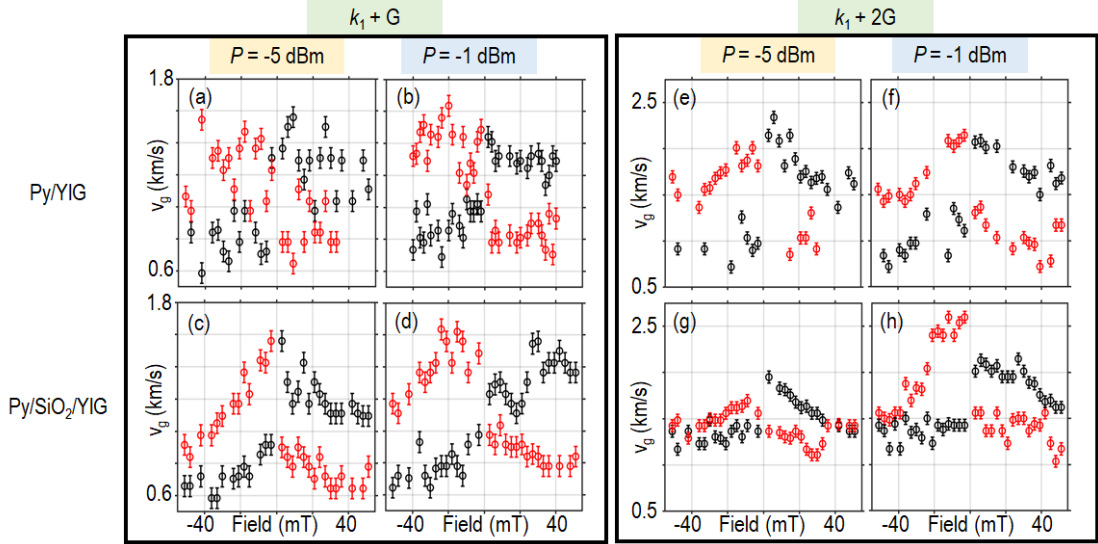


Figure 4.22: Group velocity extracted for $k_1 + G$ (a-d) and $k_1 + 2G$ (e-h). In the VNA measurements we use $P_{\text{VNA}} = -5$ dBm (-1 dBm) in panels a,c and e,g (b,d and f,h). Group velocities for sample A (B) are summarized in panels a,b and e,f (c,d and g,h)

We consider measurements acquired with $P_{\text{VNA}} = -1$ dBm for a large SNR. In Fig. 4.22 we report the extracted group velocities for two magnon modes $k_1 + G$ and $k_1 + 2G$ for sample A and B. The red (black) datasets represents the group velocity extracted for S_{12} (S_{21}) i.e. magnons propagating with $+k$ ($-k$). We find asymmetric group velocities between counterpropagating magnons. The asymmetry is reversed almost abruptly when the field changes sign. We calculate δv_g as the difference of group velocities extracted from S_{12} and from S_{21} (red and black datasets in Fig. 4.22, respectively). Therefore δv_g is positive (negative) when $H < 0$ ($H > 0$). On average the magnitude of the group velocity asymmetry $|\delta v_g|$ in Fig. 4.22b amounts to ~ 300 m/s. The asymmetry is observed for magnons with $\lambda = 195$ and $\lambda = 99$ nm (GC2). In general we observe that v_g decreases with increasing field magnitude $|H|$.

In the following we assume that $\delta v_g \neq 0$ arises from iDMI. Following [114] we extract a iDMI strength $D = (77 \pm 17) \mu\text{J}/\text{m}^2$. The data in Fig. 4.22 have been taken at relatively large power. We now compare this value D with the value of D obtained with reference sample which we fabricated with the same CPW geometry as used in [114]. This device is on bare YIG without any magnetic grating. It excites most efficiently a magnon mode with $k_1 = 2.75 \text{ rad}/\mu\text{m}$. We sweep the field from 90 mT to zero with 2 mT steps and record the scattering matrix in the symmetric jumper configuration. We extract the group velocity at $P_{\text{VNA}} = -13$ dBm benefiting from the large SNR. Figure 4.23 summarizes in red [black] the group velocities extracted from signal $\text{Imag}(S_{12})$ [$\text{Imag}(S_{21})$] at positive fields. The dashed blue line illustrates the v_g predicted

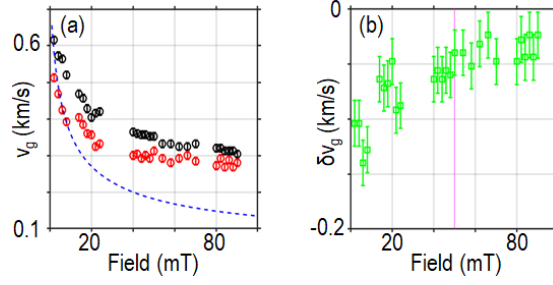


Figure 4.23: (a) Experimentally extracted group velocities for S_{12} (S_{21}) transmission in red (black) colored symbols. The group velocity taken from the KS model at $k = 2.75 \text{ rad}/\mu\text{m}$ is shown as the dashed blue line. (b) Group velocity asymmetry δv_g . The magenta line at 50 mT indicates the field beyond which δv_g seems to level off.

	(a)	(b)	(c)	(d)	(e)
$D [\mu\text{J}/\text{m}^2]$	4.34	4.57	3.78	3.68	6.3

Table 4.2: Values D extracted from the frequency shift δf_{\pm} of (a-b) GC1 and (c-d) GC2 magnon modes at -6 and -12 mT, respectively. (e) D extracted from the group velocity asymmetry at 80 mT with the same CPW design as in [114].

by the KS model. This curve describes well the lower lying experimental data below 10 mT. The experimental group velocities approach $\sim 300 \text{ m/s}$ at 80 mT (Fig. 4.23a). Here the KS model predicts a smaller value. In Fig. 4.23b the group velocity asymmetry δv_g is summarized and varies with H . δv_g approaches -50 m/s at 80 mT. The behavior qualitatively agrees with what has been reported in [114]. Following [114] we consider δv_g for $\mu_0|H| > 48 \text{ mT}$ to estimate the iDMI strength D . We find $D = (6.3 \pm 1.8) \mu\text{J}/\text{m}^2$. This value is consistent with data in [114] and [135]. Additionally, we extract the frequency difference δf_{\pm} between counterpropagating magnons with $\mathbf{k} = -\mathbf{k}_1$ and $+\mathbf{k}_1$. According to Eq. 2.37 this is a separate measure of D . We apply this for sample A and measure δf_{\pm} for GC1 and GC2 at -6 and -12 mT for $P_{\text{VNA}} = -5 \text{ dBm}$. Table 4.2 summarizes the extracted values D .

4.3 Thermal magnon spectra of bottom-up nanopatterned Py and YIG thin films

In this section we present a method by which we target nanopatterning of Py with lateral feature size below 50 nm (Fig. 3.16). Practically we follow a bottom-up approach in that self-organized DNA lattices are exploited to modify the Py properties in length scales which are routinely smaller than achieved in our electron-beam lithography processes. We present BLS studies of thermally-activated magnons in surface corrugated Py. In all cases the surface corrugation is realized by decorating the substrate with DNA-based structures and then evaporating the magnetic thin film on top. We discuss experimental results for a Py thin film deposited on mica and for a Py thin film deposited on 100-nm-thick YIG. In both studies

the DNA samples are purchased by Tilibit. The DNA origami provided by Tilibit modify nanomagnets at lateral length scales that could still be reached with conventional top-down nanolithography. Such bottom-up created artificial nanosystems can hence be compared to having similar lateral parameters that have been fabricated with top-down approach. To go beyond the state-of-the-art in this PhD we have pursued the unprecedented downscaling of magnonic crystals in that we applied DNA periodic lattice with lattice pitch $p = 31$ nm.

4.3.1 Atomic force microscopy characterization of DNA origami on mica

DNA origami lattices, which we first report on, are purchased from Tilibit Nanosystems GmbH. The DNA lattices, subsequently coated by Py, feature a dual basis unit cell with two different holes having 30 (type A) and 24 (type B) nm diameter. The lattice pitch p is defined as the distance between holes of the same type. From the measurements of real space images we obtain $p = (136 \pm 5)$ nm (Fig. 4.24a,b). In the analysis several 1D line profiles have been considered and an average value is extracted from each of them. Then the average value and its standard deviation are estimated. This value is further confirmed by the analysis of FFT images (Fig. 4.24c,d). Extracting $2 \cdot \Delta k$ in Fig. 4.24d allows us to estimate the lattice pitch $p = \frac{2\pi}{\Delta k} = 138$ nm, in agreement with the previously estimated value. The sample is further processed in the cleanroom to deposit, via electron-beam evaporation, 5-nm-thick Py. For capping against oxidation, 3-nm-thick Al is added. After this step AFM characterization gives $p = (126 \pm 3)$ nm thus suggesting a slight modification of the lattice. Wave vector analysis and topography analysis both suggest that by growing Py onto DNA lattices we obtain periodically surface corrugated Py thin films (Fig. 4.25c).

4.3.2 BLS microscopy of thermal magnons

In the following we probe thermal magnons by μ BLS setup. We compare data obtained on plain film Py (PF-Py) and Py on DNA which exhibits surface corrugation (SC-Py). The laser light ($\lambda = 532$ nm) is focused within ~ 300 nm and scanned over regions of interest (ROIs) that we identified by AFM. Using a green laser at an optical power = 0.8 mW (measured at the input of the objective lens) we record thermal magnon spectra in different spots of the sample (Fig. 4.26).

We conduct two-dimensional raster scans at different in-plane magnetic fields going from 240 to 20 mT. The raster scans cover an area of $(10 \mu\text{m})^2$. The step size is 500 nm in x and y direction. Fig. 4.27a compares BLS spectra for thermal magnons measured on both SC-Py and PF-Py. Peaks are observed at smaller frequency as the field is reduced from 240 mT to 60 mT. At the same field the magnon resonance peak obtained on SC-Py is at a lower frequency and features a weaker intensity than the of the PF-Py region. The full width at half maximum (FWHM, Δf) is observed to decrease with increasing H and f_{res} for both kinds of Py. This characteristic behavior does not follow $\Delta f(f_{\text{res}})$ expected for Gilbert damping. The FWHM is larger for SC-Py at all fields by approximately the same amount of 0.25 GHz. We

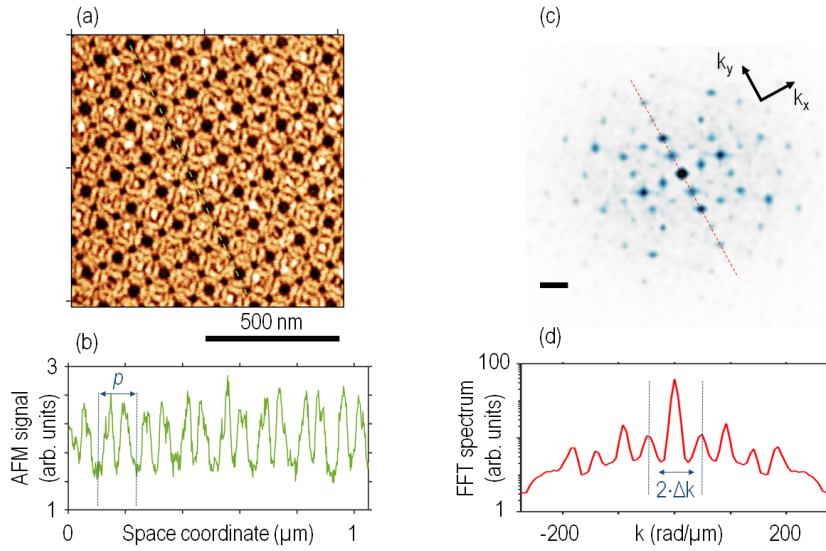


Figure 4.24: (a) AFM real space image of DNA lattice on mica before Py evaporation. The green dashed line indicates a 1D line profile that is used to extract the lattice pitch p . (b) 1D line profile extracted from (a). (c) Reciprocal space image obtained from the FFT of (a). The scale bar is $62.8 \text{ rad}/\mu\text{m}$. (d) 1D line cut of the FFT 2D spectrum to evaluate the reciprocal vectors along the high symmetry axis.

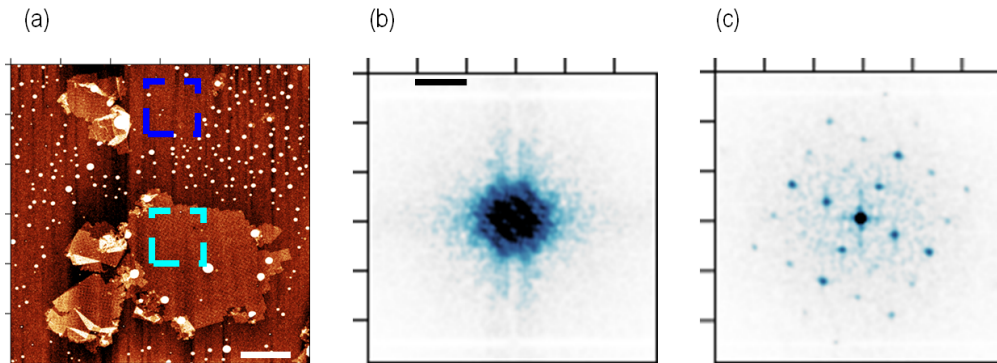


Figure 4.25: (a) AFM image of a DNA lattice coated by 5-nm-thick Py. FFT analysis of the topography data highlighted by the blue [cyan] dashed box is reported in (b) [(c)]. The data shown in (c) substantiate that the Py covering the DNA inherits its periodic topography.

attribute the larger FWHM on SC-Py to be induced by the surface corrugation. The larger linewidth might indicate two-magnon scattering. The surface corrugation imprinted by the DNA can have the same effect as defects/impurities enabling two-magnon scattering. This is in agreement with Ref.s [47],[57] where two-magnon scattering is proved to play a role in the frequency-dependent spin relaxation of periodically patterned systems. Besides, a similar behavior was reported for CoFeB thin films with top-down engineered surface roughness [94]. At the same time the signal intensity is smaller (4.27a). We note the presence of particulates in our sample, that appear as white dots in Fig. 4.26. These are chemical residues

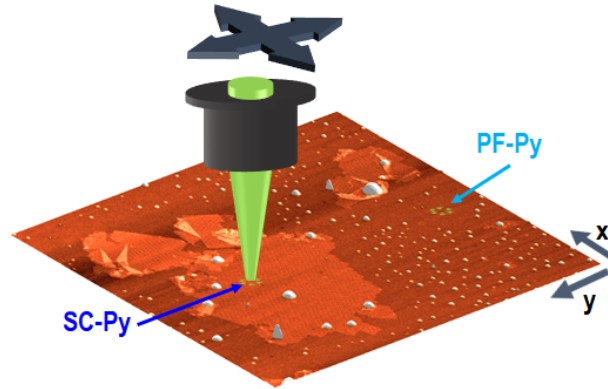


Figure 4.26: Sketch of the BLS experiment. The green laser light is focused on the sample achieving local probing of the magnetization dynamics. Measurements are conducted on the surface corrugated Py, (SC-Py), and, as reference, on the plain film Py, (PF-Py).

of the buffer solution containing the DNA lattices. If one was to measure exactly on top of the particulate, the resulting spectra could be modified. To address this, we have repeated reference measurements in macroscopically different regions of the PF-Py. In comparison to all these reference measurements we observed a larger FWHM and smaller resonance frequency for measurements on SC-Py. These data suggest that SC-Py magnetization possesses inhomogeneous internal fields and/or spin structures. We attribute these properties to the periodic surface corrugation induced by the DNA. In a further study we measure the thermal magnon spectra over a 2D area. Our goal is to locally observe the space-dependence of the magnon band minimum (Fig. 4.28). The magnon band minimum is found to reside at smaller frequencies for the space regions corresponding to SC-Py as it can be seen by comparison of Fig. 4.28a and b. Here the magnetic field is fixed at 240 mT.

We fit the field-dependent resonance frequencies of PF-Py with Kittel's formula assuming an ideal plain film with $N_x = 1$ (Eq. 2.25) to extract $\mu_0 M_{\text{eff}}$. Therefore $N_x = N_z = 0$ for the plain film. We measure the field-dependent spectra in different positions on PF-Py. For each position we extract a value for $\mu_0 M_{\text{eff}}$. We average these values to obtain the final estimated effective magnetization of the plain film: $\mu_0 M_S^* = (797 \pm 5)$ mT. We use $\mu_0 M_S^*$ as a fixed parameter to fit the field-dependent resonance frequencies of SC-Py. Here we assume $N_x < 1$ and $N_y = N_z \neq 0$ because of the surface corrugation. We fit Kittel's formula (Eq. 2.24) to extract the modified demagnetization factors. Our approach to analyze the effect of surface corrugation on the demagnetization field is motivated by [17]. Here, the author has predicted that surface roughness in a thin film generates an effective perpendicular anisotropy term which is purely of dipolar origin. In [31], demagnetization tensor components modified by surface roughness have been considered. The fit results for field-dependent spectra obtained on five different positions on SC-Py are reported in Fig. 4.27d. In Fig. 4.27d measurement positions 2-5 are taken on a different region, i.e. on a different DNA patch, than in measurement position 1. These two distinct patches are separated by several μm . We average these five values and

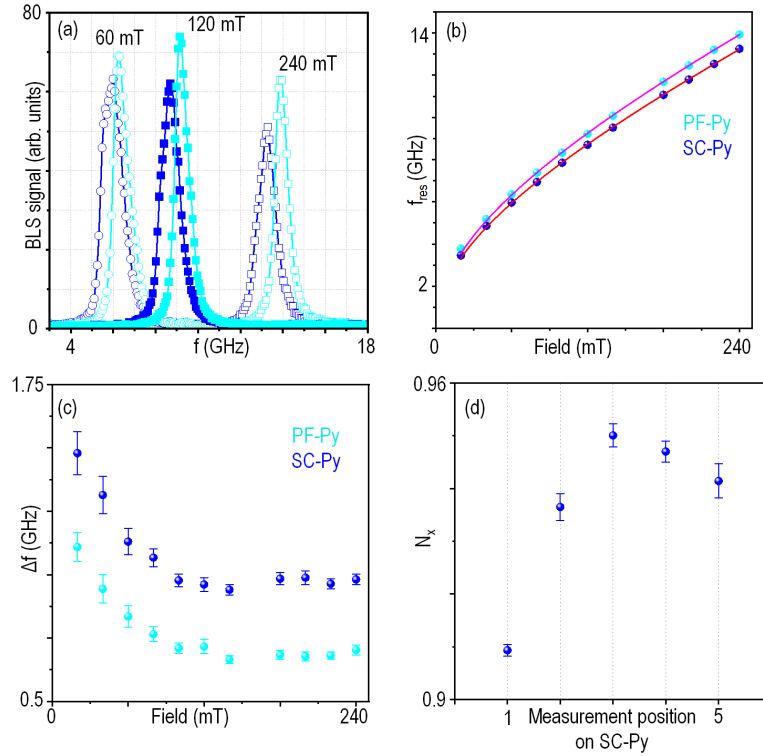


Figure 4.27: Spectra for SC-Py (PF-Py) in blue (cyan). (a) BLS spectra for $\mu_0 H = 240, 120$ and 60 mT. After normalizing the BLS spectra with respect to the counts obtained for the elastic peak we have multiplied them by a factor 10^5 (b) Field dependence of f_{res} obtained after fitting a Lorentzian to each spectrum experimental dataset. The solid magenta and red lines are the fits to the Kittel formula. For PF-Py we have assumed $N_x = 1$ when fitting the Kittel formula. (c) Field dependence of linewidth Δf . (d) The fitted demagnetization factor N_x for four measurement positions on SC-Py.

obtain the averaged demagnetization tensor component: $N_x = (0.937 \pm 0.002)$. We interpret the systematically modified resonances in SC-Py by a change in internal field due to the modified demagnetization tensor component of the SC-Py. From the fit results we evaluate the N_y and N_z components as well. In the fit we assume $N_y = N_z$ and obtain the average value $N_y = N_z = 0.032 \pm 0.001$.

4.3.3 Perpendicular standing spin waves in a DNA-decorated YIG thin film

We immobilize DNA origami PF2 (Fig. 3.12) on 100-nm-thick YIG (Fig. 4.29). We use AFM to assess the successful DNA adsorption on the surface. After identifying regions of interest with the AFM we deposit 10-nm-thick Py and we add a cap layer (3 nm Al) as protection layer from oxidation. Fig. 4.29a,b show a detailed AFM image of DNA-PF2 immobilized on the substrate before evaporation. In Fig. 3.12c the AFM image is taken after Py evaporation. It shows a large area being decorated by DNA-PF2.

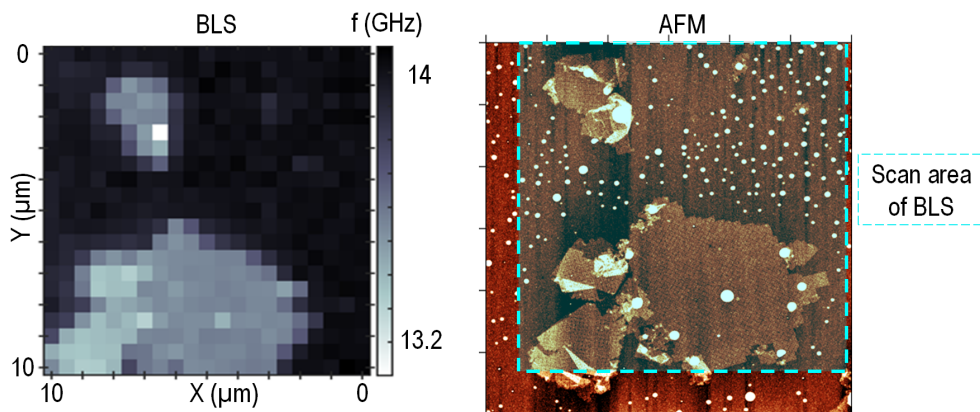


Figure 4.28: Magnon resonance at 240 mT frequency is extracted for each measurement point and reported as a function of space coordinates x,y in a 2D color map (left panel). This is to be compared with the AFM image (right panel) taken on the area probed by BLS. The BLS data reveal lower resonance frequencies for Py (grey) on DNA compared to Py on mica (dark).

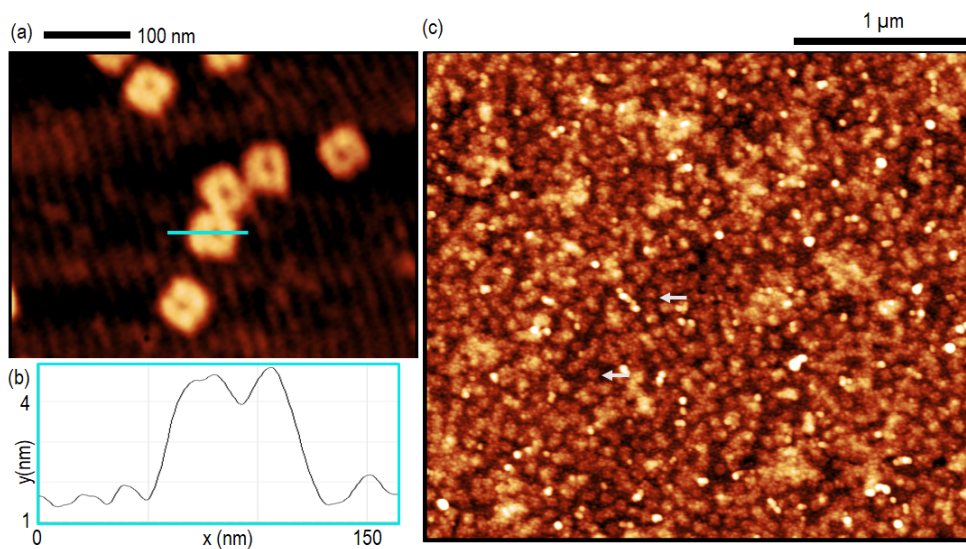


Figure 4.29: (a) DNA-PF2 immobilized on the substrate before Py evaporation. (b) 1D line profile across the DNA origami highlighted by the cyan line in (a). (c) Large scale image of DNA-PF2 after evaporation of 10-nm-Py and 3-nm-thick Al. The grey arrows indicate topography signals attributed to underlying DNA-PF2.

In the μ BLS setup we focus the green laser light onto the sample and record field-dependent thermal magnon spectra. The field varies from 230 mT to 20 mT. We measure two positions where the Py is coating the DNA origami on YIG (Pos1 and Pos2). On the same chip, we take spectra on Pos3, a position where DNA-PF2 was avoided. An additional reference dataset (Pos4) is measured on another chip with the nominally identical YIG substrate. Pos3 represents a sample that has been exposed to all the process steps and solutions for DNA deposition without containing DNA-PF2. Pos4 is measured on a pristine interface Py/YIG bilayer that did

not undergo the chemical treatments involved in the DNA deposition. Py was evaporated in the same deposition for both YIG substrates.

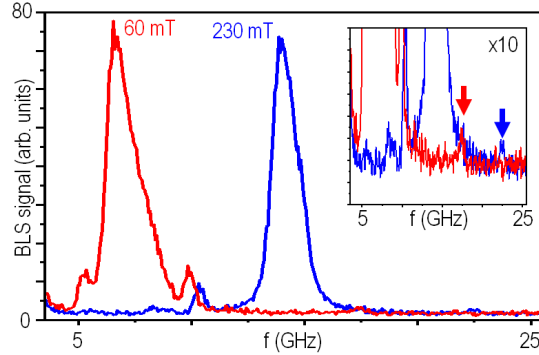


Figure 4.30: BLS spectra taken of a location where Py resides on top of the DNA-PF2. (a) BLS spectra for $\mu_0 H = 230$ (blue) and 60 (red) mT. The inset shows the same spectra on a different y-scale to highlight (arrows) the high-order PSSW of YIG.

In Fig. 4.30 we report normalized BLS spectra taken at 230 mT and 60 mT on Pos1. Several peaks are observed. The peaks shift to low frequency when the applied field is reduced. The most prominent peak is attributed to the Py resonance. This main peak has asymmetric shape and we fit it with two Lorentzian curves. We suggest that this could be related to the fact that with the laser we probe the resonance of the plain film Py and the resonance of the Py covering the DNA origami. We speculate the shifted resonance of the Py covering the DNA origami has the same origin as the DNA-shifted resonances discussed in paragraph 4.3.2. The multiple peaks with lower intensities are attributed to PSSWs in YIG with different quantization number by evaluating the KS formalism for 100-nm-thick YIG. Here we focus on the highest YIG resonance that is indicated by the red and blue arrows in the inset of Fig. 4.30. For this resonance we study the field-dependent behavior. The same YIG has been investigated by Che et al. [107] hence we assume their magnetic parameters: $\mu_0 M_{\text{eff}} = 180$ mT and $A_{\text{ex}} = 2.7$ pJ/m. We fit the relationship $\omega_{\text{PSSW}, d_s}$ from Eq. 2.33 to extract the spin pinning parameter d_s . The peak resonance and its field-dependent behavior is reported in Fig. 4.31 for Pos1, Pos2, Pos3 and Pos4. The fit results are reported in each panel. d_s is the smallest for Pos1 and Pos2 which are considered to contain DNA. d_s is maximum for Pos 3 where, without placing DNA, oxygen plasma is conducted before Py evaporation. The second largest spin pinning parameter is recorded for the pristine YIG interface, without any chemical treatment before the Py evaporation. This findings suggest that the presence of DNA at the interface between YIG and Py locally modifies the spin pinning boundary condition and leads to a smaller frequency for the PSSW resonance.

4.3.4 Towards unprecedented miniaturization of magnonic crystals

We have encountered several experimental challenges that stemmed all mainly from the low yield and poor reproducibility of the DNA honeycomb lattice with the small p . We aimed

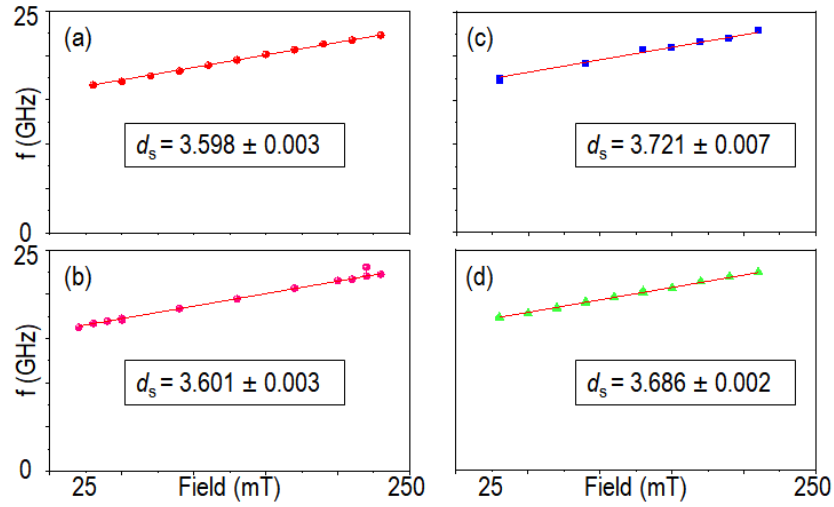


Figure 4.31: The extracted resonance frequency for the high-order PSSW in YIG is reported as a function of magnetic field. Eq. 2.33 is fitted to the data to evaluate d_s for two distinct spot Py/DNA-PF2/YIG (a,b), one reference spot on the chip Py/YIG (c) and one reference spot where Py is evaporated on a pristine YIG substrate (d). The estimated d_s is consistently smaller when the PSSW is probed in spots where DNA-PF2 resides between Py and YIG.

at lattices extending over several μm . After the long-term optimization of preparation and deposition protocols, we successfully placed sufficiently large DNA lattices and evaporated 5-nm-thick Py protected by 3-nm-thick Al (Fig. 4.33). The surface corrugation is experimentally demonstrated by these AFM data.

We show micromagnetic simulations to highlight the key potential that this approach and this geometry has to offer for nanomagnonics. The we present the AFM characterization.

We conducted micromagnetic simulations on surface corrugated Py thin films. We consider periodic lattices featuring lateral parameters comparable to the DNA honeycomb lattice. The modelled geometry is shown in Fig. 3.1. In Fig. 4.32a,b We report the simulated magnon band structures at +90 mT for ideal-surface corrugated Py thin films. The Py thickness is 3 nm (a) and 5 nm (b). The color-coded intensity represents the power spectral density for the middle layer. The dashed green lines mark the wave vector region which corresponds to the unit cell in reciprocal space (first Brillouin zone, BZ1). For each thickness we observe the formation of a magnon band structure with allowed minibands. The simulation results support the assumption that the proposed patterning method can be used to fabricate magnonic crystals. A band gap (BG) opening occurs at the wave vector corresponding to $k_{rmBZ1} = 116 \text{ rad}\mu\text{m}$. The minibands can be understood in terms of backfolding due to a periodic scattering potential induced by the corrugation. The width and center frequency of the BG depend on the film thickness (Fig. 4.32c and d). For small thickness, the BG width is $\approx 2.25 \text{ GHz}$. It monotonically decreases as the thickness is increased. The qualitative trend corresponds to $\text{BG width} \propto \frac{1}{\text{thickness}}$ and agrees with recent findings for surface-modulated thin film Py

investigated in the dipolar regime in [85], [97]. In the simulations the BG width is non-zero for $t = 40$ nm. For a 2-nm surface modulation, representing only 5% of the total thickness of 40 nm, a BG is still developed. No difference is observed for magnons propagating in opposite directions. The BG center frequency has a non-monotonic behavior and reaches its maximum (≈ 27.4 GHz) for $t_C = 10$ nm. The micromagnetic modelling suggests that in order to see a large effect the thin film thickness should be smaller than t_C . In so doing one achieves a surface modulation of at least 20% of the total thickness.

We note that in agreement with [85] we observe the formation of an engineered band structure for a surface corrugation height of 2 nm. However in [85] the lateral modulation is such that the first BZ boundaries fall in the dipolar regime with $k_{BZ1} = \frac{1}{2} \frac{2\pi}{a_z} = 10.5 \text{ rad}/\mu\text{m}$ (Fig. 2.4). In our systems the modulation is such that the first BZ boundaries fall inside in the exchange-dominated regime with $k_{BZ1} = \frac{1}{2} \frac{4\pi}{3p} = \frac{1}{2} 232 \text{ rad}/\mu\text{m} = 116 \text{ rad}/\mu\text{m}$.

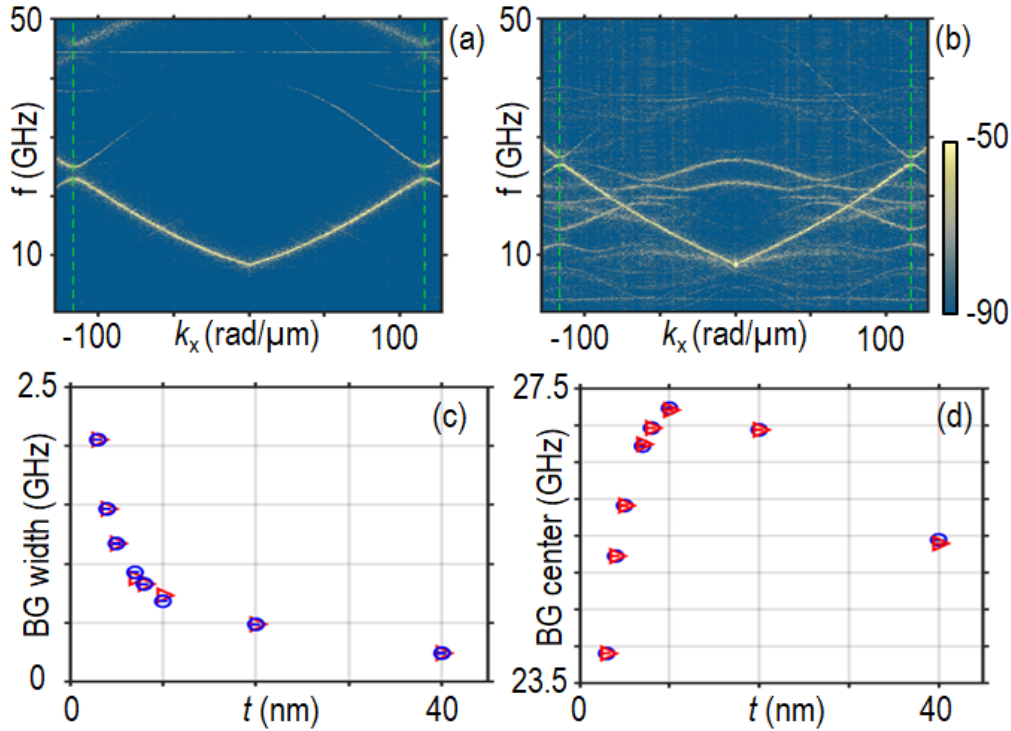


Figure 4.32: (a),(b) Bandstructure at +90 mT for a 3 and 5 nm thick Py thin films respectively, with 2 nm surface corrugation. (c),(d) BG width and its center frequency are analyzed as a function of total film thickness for the same 2 nm surface corrugation. The red (blue) dataset indicates magnons with $k_x > 0$ (< 0).

The lattice pitch of the experimentally explored honeycomb lattice is by design $p = 31$ nm. In Fig. 4.33 the DNA honeycomb lattice is studied after immobilization on the mica substrate. In panel a we report a large scale AFM picture of a single layer of DNA lattice that has adhered in a flat manner on the substrate. The FFT of the topography signal is shown in panel b. Panel c

shows a detailed view of the periodic lattice. After evaporation of 5-nm-thick Py and 3-nm-thick Al (the cap layer) we characterize the system again with AFM and obtain the image in Fig. 4.33d. The periodic structure of the lattice is not observed in the topography signal due to increased surface roughness. Still the FFT analysis shows the periodic pattern of hexagonally distributed peaks. This is strong evidence that the overgrown magnetic thin film inherits the periodic topography by the DNA lattice. The usage of DNA lattices as nanotemplates for magnetic materials by over-growth is hence successful. In the AFM characterization we extract for both cases, before and after evaporation, $p = (31 \pm 1)$ nm. From this we estimate the side length of the hexagonal surface corrugation to be $l = (18 \pm 1)$ nm. These values are consistent with the design values. If such structure would be operated as magnonic grating coupler the first resonant wave vector (wavelength) would amount to $k_{GC1} = 232$ rad/ μm ($\lambda_{GC1} = 27$ nm). Magnons with such a wave vector (wavelength) would reside at a few 10 GHz in thin Py. Based on Eq. 2.28 we expect the linewidth to few GHz broad, considering the relatively high damping parameter α of thin film Py and the high estimated resonance frequency. These efforts motivate a weak magnon signal that has low SNR in the thermal magnon measurement with μBLS . Indeed so far we have not been able to probe corresponding GC modes by thermal excitations in μBLS . A further reason might be the limited wave vector regime of μBLS . With our lens the μBLS can detect magnons with $k < 26.6$ rad/ μm . For a good SNR either the intensity of the branches back-folded to $k < 26.6$ rad/ μm must be large enough or the surface corrugation of the metal surface must allow for diffraction of the laser light to achieve high wave vector for momentum conservation with the short-waved magnons. Here, further work is needed to optimize the detection scheme.

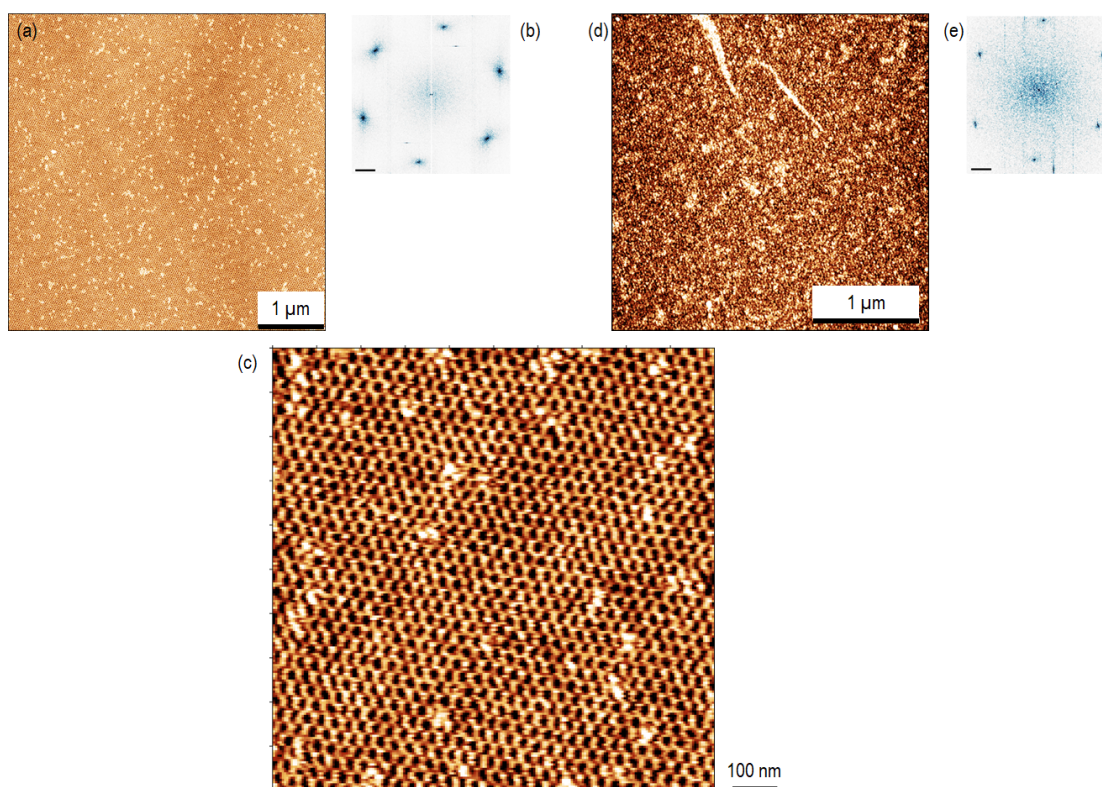


Figure 4.33: (a-c) AFM characterization of a mica substrate decorated with DNA honeycomb lattices (a) before Py evaporation. (b) FFT analysis of the topography signal. (c) Detailed image showing the hexagons of the lattice [taken from (a)]. (d) AFM image after evaporation of 5-nm-thick Py and 3-nm-thick Al. FFT image computed from (d). (b),(d) The scale bar is $62.8 \text{ rad}/\mu\text{m}^{-1}$.

5 Conclusions and outlook

In this chapter we summarize the main achievements of this thesis and give an outlook to the future work that this thesis stimulates.

5.1 Conclusions

In this thesis we have prepared one-dimensional periodic array of nanomagnets integrated on top of yttrium iron garnet with different thicknesses and different interlayer spacers, i.e. Cu and SiO₂. By inductive VNA spectroscopy and μ BLS microscopy we have studied the magnetization dynamics and the magnon-induced nanomagnet reversal. We demonstrated that different magnon modes induce switching. The critical powers to initiate switching depend on the magnon frequency. This switching occurs for continuous wave excitation and for pulsed excitation as we demonstrated with μ BLS. We observed that magnons propagating to both directions induce reversal at different excitation powers due to non-reciprocity in DE configuration. The studies on hybrid structures Py/YIG differing by the interlayer spacer (Cu and SiO₂) suggest that static interlayer exchange interaction is not necessary and that dipolar coupling between Py and YIG is key for the magnon-induced reversal. Adding the spacer is found to modify the stripes' coercivity with respect to the direct-interface Py/YIG samples [133]. At high RF powers P_{irr} we found that the critical field for switching increases in the sample with the Cu spacer between Py and YIG. A similar observation was also reported in the sample with direct-interface [133]. The rise of the critical field at high RF powers might be due to non linear spin wave excitations. We have not observed in the sample with SiO₂ the same increase of critical field. This result suggests that such a behavior is related to the magnetic interface. *Sample_SiO₂* blocks spin current transmission across the interface in contrary to the other two samples ([133] and *sample_Cu*).

These findings motivate further the design and optimization of materials and device structures to achieve switching at minimum power. An enhanced coercivity is relevant in the perspective of future applications of the reversal phenomenon to non-volatile magnon memory. Based on our results we suggest that the dynamic stray field of the propagating magnons is enough

to initiate the switching. In our experiments based on long nanostripes such a field could nucleate a magnetic domain at the edge of a stripe. The domain wall may then be moved by the combined action of the magnons and magnetic field until the reversal is completed. However a full microscopic understanding of this magnon-induced reversal mechanism is still lacking.

On the 11-nm-thick YIG we have prepared one-dimensional periodic arrays of nanomagnets on the bare YIG substrate and on SiO₂, acting as a spacer, on YIG. The magnon-induced reversal occurs at larger powers than in 113-nm-thick YIG. Overall we find that switching is less efficient and need larger bias fields than for the 113-nm-thick YIG. In the ultra-thin YIG we characterized the non-reciprocity of propagating magnons with $\lambda = 99$ nm (GC2 mode). We apply two methods to evaluate iDMI strength. We find values that are consistent with sputtered thin YIG [135], [114]. During this study we find that the group velocity asymmetry depends on VNA power. We suggest this is consequence of non-linear magnon dynamics at high RF powers. However the microscopic reason is not yet experimentally investigated.

We find avoided a crossing between the Py fundamental mode and the GC2 mode. The cooperativity C was characterized for samples with both exchange and dipole-dipole interactions (Py/YIG) and with only dipole-dipole interaction (Py/SiO₂/YIG). The avoided crossing is evidence for coupled dynamics between YIG and Py. We consider this coupled dynamics a possible explanation for the large magnon amplitude non-reciprocity that we have measured. We found in our data that the coupled dynamics leads to larger critical fields and larger critical power levels are required for the magnon-induced switching of Py stripes. In both type of samples, we find intermediate coupling regime with $C > 1$. Our findings are stimulating in the perspective of chiral nanomagnonics at short wavelengths.

DNA nanotechnology is the bottom-up approach we propose to explore novel pathways for nanomagnonics. We have prepared Py thin films on different substrates that have been previously decorated with DNA periodic lattices and individual DNA origami structures. Our findings suggest that DNA can be used as a nanostructured template onto which magnetic thin films are grown and obtain modified properties that allow us to engineer magnon resonances in Py and YIG on ultra-short length scales. In surface corrugated Py on DNA periodic lattice our data show a frequency shift of the magnon band minimum. Our interpretation is that the demagnetization tensor is modified by the surface corrugation thus changing the internal field. For the Py on the DNA-decorated YIG we observe a frequency shift of confined magnon modes in YIG. The PSSW of YIG resides at lower frequency when the individual nanoscale DNA structure is in between the Py and YIG. Using the KS model we suggest that this is explained by a locally modified spin pinning boundary condition induced by the presence of DNA origami.

Our micromagnetic simulations suggest that the novel DNA-based approach can lead to the fabrication of magnonic crystals with minibands and frequency gaps. The magnonic crystals would feature a first Brillouin zone that falls already into the exchange-dominated regime. By AFM we prepare and characterize DNA honeycomb lattices on mica with 31 nm lattice

pitch. We have successfully prepared deposition protocols and evaporated Py thin films on different samples inheriting the surface corrugation. Limitations in either signal strength of backfolded magnon branches or the wave vector resolution of BLS might have compromised the experimental verification of minibands.

5.2 Outlook

Magnon-induced reversal of nanomagnets

The magnon-induced reversal of nanomagnets unlocks the possibility of non-volatile memory of spin wave signals where magnetic bits are written with linear and non linear magnon signals without conversion to the electrical domain. Understanding the physics of the reversal mechanism is key to exploit this phenomenon at minimum power and without the currently applied bias field. Future studies should explore in particular nanomagnets avoiding domain wall formation and promising nanoscale magnetic bits for storage. The intrinsic timescales need to be addressed by further time-resolved studies.

To achieve imaging one could consider XMCD measurements with burst excitation of magnons. The high spatial and temporal resolution at state-of-the-art synchrotron beamlines combined with the element-specific sensitivity of the technique could allow to follow the switching event in case of coherent reversal. Probing different elements will contribute to observe the dynamics in the nanomagnet and the magnon propagation before and after the interaction with the nanomagnet itself. To evidence the full functionality of the magnonic memory the XMCD experiment might be performed on a nanomagnet array which experiences a specific spin-wave interference pattern in the underlying YIG (Fig. 5.1). Such an experiment would mimic the storage of magnon signals resulting from a wave-based logic operation.

We propose to research novel approaches, device design and materials that would allow for toggle switching, i.e. the ability to switch between the two available magnetic states. This would enable to write a magnetic bit, and at a later stage when needed to reconfigure the nanomagnet in its original state.

Miniaturization of magnonic crystals with DNA nanotechnology

After successful patterning of Py at a lateral length scale < 50 nm the next step is to probe the expected high-frequency eigenmodes. We propose to investigate magnon modes by X-ray scattering (SAXS). Recently Wittrock and co-authors [131] have demonstrated together with our group the small angle X-ray scattering from sub-100-nm propagating magnons in yttrium iron garnet. This technique detects low intensity modes and achieves direct k -space imaging with large k exceeding the limitations of our lab-based technique such as BLS. Additionally we suggest to explore the magnon band structure and band gaps of surface-corrugated thin films close to Γ point by wave-vector-resolved BLS [71].

Other relevant aspects that further promote DNA nanotechnology as a nanopatterning tool to

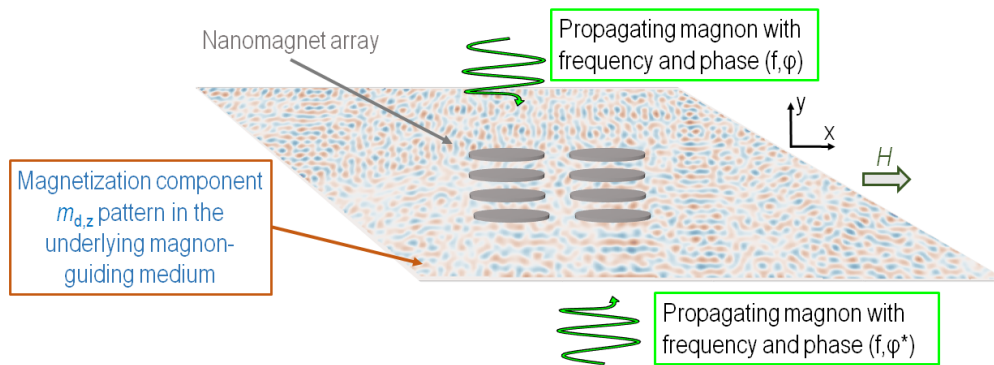


Figure 5.1: Sketch of a suggested experiment to demonstrate magnetic bit writing induced by an interference effect mimicking a wave-based logic operation. Two counterpropagating magnons are excited phase-coherently by the same RF signal with a relative phase shift $\phi = \phi^* - \phi$. The magnon interference leads to a peculiar magnon amplitude pattern depending on ϕ . Nanomagnet reversal depending on ϕ would be investigated.

achieve unprecedented downscaling in nanomagnonics are the following:

- The DNA structural and chemical stability allow one to utilize DNA lattices (made by DNA origami and/or DNA tiles) as etching masks. Sub-10-nm patterning was demonstrated by HF vapor etching of Si [74]. This has not yet been applied to magnetic thin films.
- Motivated by the advance in 2D materials and Moiré patterns we propose to prepare double layers of DNA lattices. This can be achieved by engineering the self-folding of large DNA 2D lattices by altering the salt concentration in the chemical buffer. The self-folding would naturally lead to a Moiré pattern as the honeycomb lattice sheet come on top of each other. This could potentially enable to explore the Moiré pattern induced physics of exchange-dominated magnons.
- DNA biochemistry can be utilized to form superlattices of nanoparticles (NPs) which are called programmable atom equivalent lattice, as discussed in the introduction (section 3.5). We imagine ferro- and ferrimagnetic NPs to enhance the prospects of DNA nanotechnology in magnonics.
- DNA decoration of a low-damping skyrmion-hosting materials such as insulating Cu_2OSeO_3 might modify a skyrmion lattice which is commensurate with the DNA lattice.

A Appendix

A.1 Methods

A.1.1 Experimental equipment for the preparation of DNA samples

In this paragraph we show the experimental setup that have been utilized to measure the concentrations of DNA samples and anneal the DNA-containing liquid solution that we discussed in section 3.5.3.

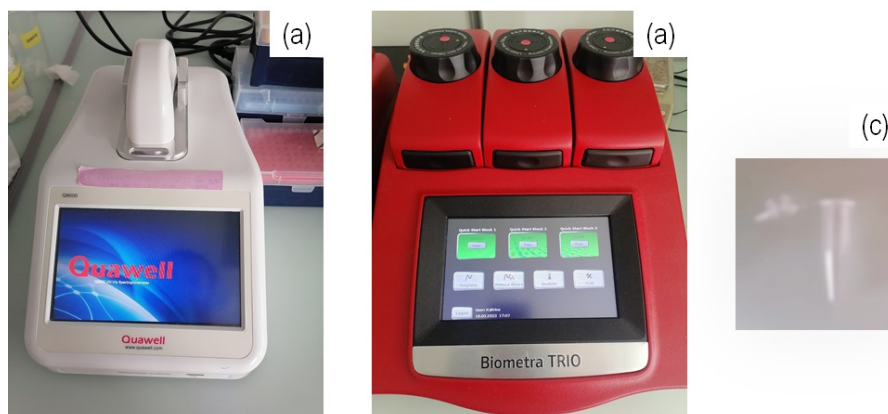


Figure A.1: Experimental equipment at PBL to measure the concentrations of DNA samples (a) and conduct the thermal annealing that leads to the formation of DNA honeycomb lattice (b). In (c) a typical PCR tube that we used to prepare the DNA-containing liquid solution is shown.

A.1.2 Annealing protocol for the customized DNA origami lattice ordered and obtained from Tilibit nanosystems

The following information are provided to us by Tilibit nanosystems. We report here below the annealing protocol that Tilibit nanosystems has used to produce our customized DNA

origami lattice:

- Incubate the sample at 70 °C for 5 mins
- Cooling down from 65 °C to 55 °C with 12 seconds per 0.1 °C speed
- Cooling down from 55 °C to 20 °C with 6 mins per 0.1 °C speed
- Incubate the sample at 20 °C forever

The solution that underwent the annealing has a total volume of 100 μl and it contains 50 nM of scaffold mixed with 200 nM of staples in buffer B (also referred to as crystallization buffer). Tilibit nanosystems has communicated to us that a combination of base-stacking and base-pairing interactions were used at the edges of the DNA origami structures for multimerization. Structures were folded and crystallized in a one pot assembly according to the annealing protocol that is outlined above. Further technical details are found in [106].

A.2 Experimental data

A.2.1 Magnon-induced reversal in 113-nm-thick YIG

Switching yield of nanostripes beneath the detector CPW

In this paragraph we provide further experimental data to paragraph 4.1.2. In Fig. A.2 we report the switching yield diagram at 20 mT for the nanostripes below the detector CPW. We observe that at 2.5 GHz, in both samples, the AP branch (Fig. Fig. A.2a,b) disappears at low powers ($P_{\text{irr}} < -20$ dBm). At higher f_{irr} we do not observe any prominent peak. However at large powers ($P_{\text{irr}} > 0$ dBm), the AP branch consistently disappears. The AP branch has larger intensity in *sample_Cu*. The P branch appears at 2.5 GHz for $P_{\text{irr}} \approx -20$ dBm in both samples. Here we observe three different frequencies in *sample_SiO₂* lead to switching (peaks A', B', C' in Fig. A.2d) whereas we observe two clear peaks in *sample_Cu*. We observe that for a selected irradiation window transmission is strongly suppressed. This is attributed to the specific magnon band structure of the hybrid system. The same behavior is found in measurement at 14 mT as well (see Fig. 4.6). We attribute peaks A', B' and C' respectively to the k_1 mode, the GC1 mode and $k_{\text{GC1+PSSW1}}$ mode, with $k_{\text{GC1+PSSW1}} = \sqrt{k_{\text{GC1}}^2 + \kappa_1^2}$ according to the KS formalism (2.5).

Switching yield of nanostripes beneath the emitter CPW

At 14 mT and 20 mT we measure $\text{Mag}(S_{11})$ to characterize the switching yield of the nanostripes beneath the emitter CPW. At 14 mT we define as AP branch the sensing frequency range 4.55 \div 4.75 GHz (Fig. A.3a,b) and as P branch the range 3.9 \div 4.15 GHz (Fig. A.3c,d). At 20 mT we define as AP branch the sensing frequency range 4.7 \div 4.9 GHz (Fig. A.4a,b) and as P branch the range 4.05 \div 4.35 GHz (Fig. A.4c,d). At 14 mT (Fig. A.3) we observe that the AP branch

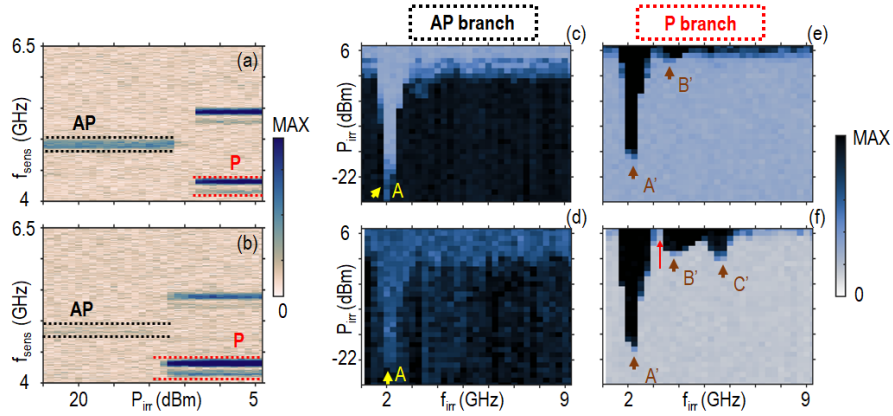


Figure A.2: (a), (b) Sensing protocol measurements of $\text{Mag}(S_{21})$ for, respectively, *sample_Cu* and *sample_SiO₂* at 20 mT for the irradiation interval (2.5 ÷ 2.75) GHz, i.e. $f_s = 2.5$ GHz. Branch P (AP) is integrated at each P_{irr} within the red (black) dotted sensing frequency band. (c)-(f) Switching yield maps for the AP branch [P branch] for (c) *sample_Cu* and (d) *sample_SiO₂* [(e) *sample_Cu* and (f) *sample_SiO₂*]. (c)-(f) Irradiation frequencies corresponding to dips (peaks) in the integrated signal are indicated in yellow (brown) letters.

disappears at low power for $f_{\text{irr}} = 1.75$ GHz, then at larger f_{irr} the AP branch disappears at $P_{\text{irr}} = -5$ dBm and its behavior does not depend significantly on f_{irr} . For the P branch we observe its appearance at -15 dBm for $f_{\text{irr}} = 1.75$ GHz. At higher frequencies for *sample_SiO₂* we find three more magnon frequencies leading to switching and for *sample_Cu* only two frequencies (Fig. A.3c,d). Peaks A', B' and C' are attributed to the same magnon modes discussed for Fig. 4.6f. Peak D' is attributed to the Py resonance therefore this corresponds to MAS [29]. At 20 mT (Fig. A.4) we observed similar behavior as discussed for 14 mT

A.2.2 Inductive spectroscopy of LPE-grown 11-nm-thick YIG

In Fig. A.5 we report as additional example of magnon amplitude non-reciprocity the transmission spectra at -18 mT when the Py magnetization is antiparallel to the YIG.

A.2.3 BLS measurements of confined magnon modes in corrugated Py

In this paragraph we report additional data to our study of 10-nm-thick Py deposited on isolated DNA origami on top of YIG (section 4.3.3). Figure A.6 summarizes the fit results of the spin pinning parameter for the second highest PSSW that we observe in the thermal magnon spectra in section 4.3.3. This PSSW is formed across the YIG thickness. We use the KS model (Eq. 2.33) to fit the resonance frequency and extract d_s . We observe that d_s is consistently smaller when the PSSW is measured on the region where the Py resides on top of the DNA (Fig. A.6c,d). We take two reference measurements. One reference is conducted on the same chip that has been processed to deposit DNA. Here we have found by AFM imaging a spot that is free of DNA origami (Py/YIG in Fig. A.6a). Another reference is taken of on another chip that

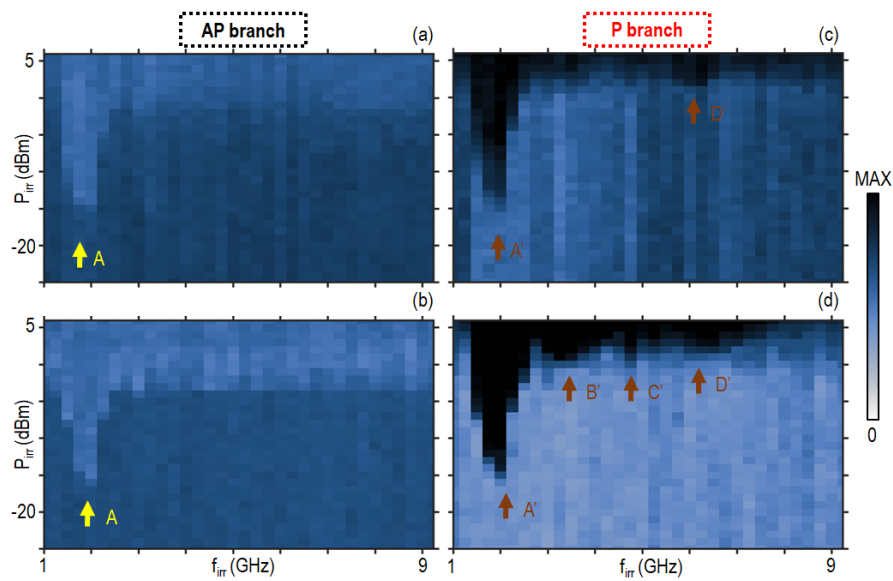


Figure A.3: Switching yield measurements of $\text{Mag}(S_{11})$ for (a and c) *sample_Cu* and (b and d) *sample_SiO₂* at 14 mT. Branch AP [P] is reported in panels (a,b) [(c,d)] Irradiation frequencies corresponding to dips (peaks) in the integrated signal are indicated in yellow (brown) letters.

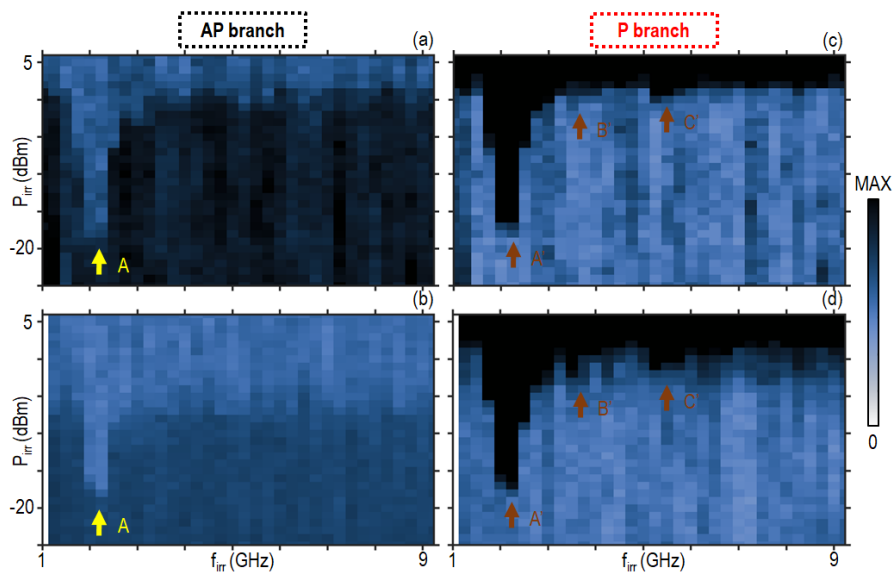


Figure A.4: Switching yield measurements of $\text{Mag}(S_{11})$ for (a and c) *sample_Cu* and (b and d) *sample_SiO₂* at 20 mT. Branch AP [P] is reported in panels (a,b) [(c,d)] Irradiation frequencies corresponding to dips (peaks) in the integrated signal are indicated in yellow (brown) letters.

was not processed hence we label this *bare YIG* (Fig. A.6b). The Py evaporation is conducted in the same batch for both chips.

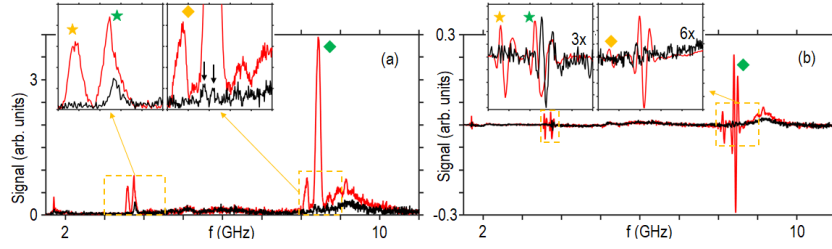


Figure A.5: $\text{Mag}(S_{12})$ [$\text{Mag}(S_{21})$] spectrum, in red [black] for device B at -18 mT (a-b) with irradiation power -9 dBm. In panel a [b] $\text{Mag}(S_{12})$ [$\text{Imag}(S_{12})$] is illustrated. The insets shows the frequency range of GC1 (stars) and GC2 (diamond). Black arrows indicate the resonances in the weakest (black) signal. (a-b) The different wave vectors are identified with symbols: the orange star (diamond) indicate $-k_1 + G$ ($-k_1 + 2G$) while the green star (diamond) indicate $k_1 + G$ ($k_1 + 2G$). Panels (c-f):

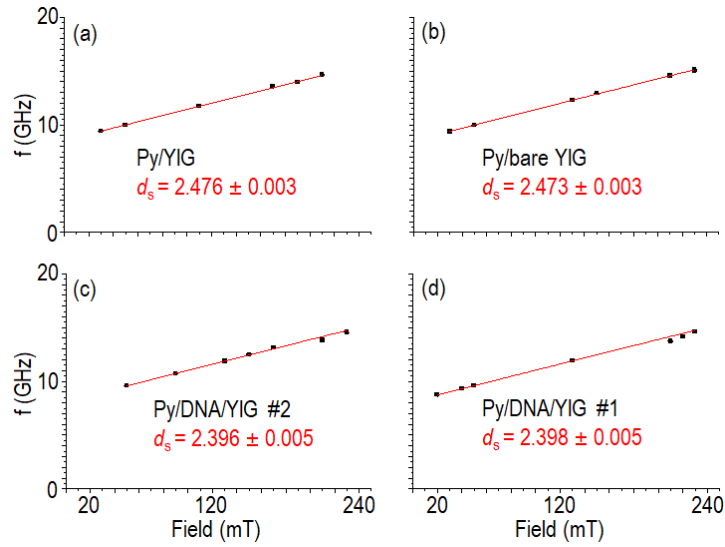


Figure A.6: The spin pinning parameter is extracted for a PSSW mode of YIG. The resonance PSSW frequency is reported as a function of applied field for (a) reference measurement Py on YIG, (b) Py on bare YIG, (c-d) Py on the DNA origami. Different spots of Py coating the DNA origami are probed.

A.2.4 Additional micromagnetic simulation data

In Fig. A.7 we report the estimated band gap (BG) width and center at 180, 150 and 60 mT. We conducted micromagnetic simulations of magnon band dispersion in Damon-Eshbach configuration for the same systems that are discussed in section 4.3.4. These results are consistent with our discussion in section 4.3.4. As the thickness increases the BG width (BGW) decreases. The BGW is 2 GHz for a thickness of 3 nm then it monotonically decreases to 0.25 GHz when $t = 30$ nm. We do not observe that the BGW varies significantly as the field is reduced (Figs A.7a,c,e). The BG center (BGC) shows the non-monotonic behavior discussed in section 4.3.4. At any field we observe that $t = 10$ nm is the critical thickness value beyond

which the BGC starts decreasing.

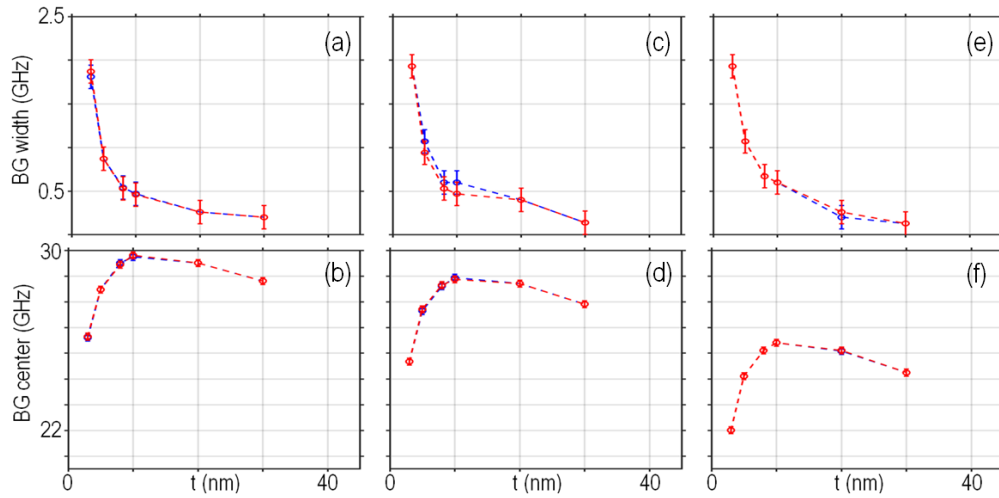


Figure A.7: BG width and center estimated from micromagnetic simulations conducted at (a,b) 180, (c,d) 150 and (e,f) 60 mT. In red (blue) the magnon band with $k>0$ ($k<0$) is illustrated.

A.3 Scripts

In this section we share examples of a simulation code to numerically model magnon dispersion with MuMax3 [65] and the postprocessing code in MATLAB to generate a band structure diagram from the numerical simulation outcome.

MuMax3 script

In the following code comments are in red and starting with `'//'`. By keeping `'//'` the interested reader can directly plug in MuMax3 this code as it is and run the simulation.

```
//—————
//In this code these some abbreviations that are used in labelling geometrical objects
//'hnc' = 'honeycomb'
//'AD' = 'AntiDot'
//'corrug' = 'corrugation'
//—————
//Define output format to txt
OutputFormat = OVF2_TEXT
```

```
//Setting Simulation Geometry

//Define grid size

Nx:=18*180

Ny:=15

Nz:=7

//Define cell size

Cx:=3e-9

Cy:=2.08e-9

Cz:=1e-9

//Define dimensions of the whole simulated volume

Lx:=Cx*Nx

Ly:=Cy*Ny

Lz:=Cz*Nz

//Setting number of cells and cellsize

SetGridSize(Nx, Ny, Nz)

SetCellSize(Cx, Cy, Cz)

//—————

//Define thicknesses of sub-layers

thick_PlainFilm:=3e-9

thick_DNA_corrug:=2e-9

thick_total:= 2*thick_DNA_corrug + thick_PlainFilm

//Define lateral spacing parameter

hex_length:=18e-9

r:=hex_length

//from here on different geometrical object are defined and they combined together to form
the final surface corrugated thin film
```



```

cilynd_Atype:=cylinder(r,thick_DNA_corrug).repeat(3*hex_length,(sqrt(3))*hex_length,0).transl(0,0,0)
cilynd_Btype:=cylinder(r,thick_DNA_corrug).repeat(3*hex_length,(sqrt(3))*hex_length,0).transl(-
1.5*hex_length,0.5*hex_length*sqrt(3),0)
dot_hnc_L:=(cilynd_Atype).add(cilynd_Btype)
shifted_dot_hnc_L:=dot_hnc_L.transl(0,0,-Lz/2 + thick_DNA_corrug/2)
AD_hnc_L:=(shifted_dot_hnc_L.inverse())
AD2_hnc_L:=AD_hnc_L.intersect(cuboid(Lx,Ly,thick_DNA_corrug).transl(0,0,-Lz/2+thick_DNA_corrug/2))
AD3_hnc_L:=hnc_top2.transl(0,0,Lz - thick_DNA_corrug)
py_PlainFilm_region:=cuboid(Lx,Ly,(Lz-(2*thick_DNA_corrug)))
PlainFilm_withDot:= py_PlainFilm_region.add(shifted_dot_hnc_L)

//here the surface corrugated thin film is defined
SurfaceCorrugated_film:=PlainFilm_withDot.add(AD3_hnc_L)

//here this is just relabelling parameter

//The surface corrugated thin film is defined as the total magnetic volume to consider for
simulation
MagneticSample_toSimulate:=(SurfaceCorrugated_film)

//—————

////Set Periodic Boundary Conditions setpbc(5,15,0)

//Set excitation area
excitation_region:=cuboid(21e-9,Ly,Lz)

//Define different simulation regions
defregion(0,excitation_region)
defregion(1,excitation_region.inverse())
defregion(2,MagneticSample_toSimulate)

//—————

//save regions and set final geometry
save(regions)

```

```
setgeom(MagneticSample_toSimulate)

//—————

//Define magnetic and simulation parameters

u0:=pi*(4e-7)

//Small misalignment is applied to deviate from high symmetry axis

theta := 88*pi/180

phi := 89*pi/180

//Saturation magnetization and exchange constant for Py

Msat.SetRegion(2,800e3)

Aex.SetRegion(2,13e-12)

//Damping is set to low values because the focus is on bandstructure simulation

alpha= 1e-8

//Initial magnetic configuration

m.setRegion(2, uniform(0,1,0))

//External magnetic field magnitude

brel:=.09

//—————Obtaining static equilibrium

//Set external magnetic field

B_ext = vector(brel*sin(theta)*cos(phi), brel*sin(theta)*sin(phi), brel*cos(theta))

relax()

saveas(m,"relaxed_and_run_to90")

//Set the starting time to zero

t=0

f:= 100e9 //cutoff frequency

tstep := 5e-12 //sampling time

trun := tstep*3000 //total simulation time
```

```

t_shift:= 10*tstep //time shift w.r.t t=0 of the pulse peak

w:=2*pi*f //pulsation

amp:=-.01e-3 //pulse amplitude

//————Exciting magnetization dynamics

//Apply magnetic field pulse only in a selected region to make inhomogenous in space

//the pulse is the plan orthogonal to the equilibrium direction of the magnetization

B_ext.setRegion(0,vector(brel*sin(theta)*cos(phi) + amp*sinc(2*pi*f*(t-t_shift)), brel*sin(theta)*sin(phi),
brel*cos(theta)+amp*sinc(2*pi*f*(t-t_shift)))

B_ext.setregion(1,vector(brel*sin(theta)*cos(phi), brel*sin(theta)*sin(phi), brel*cos(theta))

//save magnetization unit vector every multiple of the sampling time

//————

//this is what it is used for postprocessing and generating the bandstructure

autosave(m,tstep)

//save averaged magnetization unit vector every multiple of the sampling time in table

tableautosave(tstep)

//Run simulation for the total time specified above

run(trun)

```

MATLAB script

The following MATLAB script is used to process layer by layer the unit magnetization vector that is recorded during the dynamic simulation in MuMax3. This code produces a band structure for each layer. This layer-by-layer analysis is relevant to observe the major contribution of the corrugated parts and the plain film part of the whole ferromagnetic thin film.

```

clear all;

close all;

pathall='C:\Users \mucchiet \Desktop \mumax_sim \forthesis \90mT '; %path to PC location
where all Mumax simulations folder are contained

allfolds = dir([pathall,'*.out']); % replace *.out with the exact name of the folder

```

```

% if you do not replace *.out and leave it like that then the
% postprocessing will be applied to each and every one of the folder inside
% the path pathall
for g=1:length(allfolds)
clearvars -except pathall allfolds g
path=[pathall,allfolds(g).name,'\']
Files=dir([path,'m0*.ovf']);
pathInit=path;
FilesInit='relaxed_and_run_to90.ovf'; % takes in magnetization of the relaxation stage - equilibrium configuration
TimeStep=5e-12; %sampling period
f_coff=30e9; %%% cutoff freq
%—————
%create parameters and values
datafileNull=[path,Files(1).name];
OOMMF_converted_dataNull=oommf2matlabwithTime(datafileNull);
datafileInit=[pathInit,FilesInit];
OOMMF_converted_Init=oommf2matlabwithTime(datafileInit);
%—————
mInit=OOMMF_converted_dataNull.dataz; % select the component of the magnetization
componentM='mz'
%—————
xn=OOMMF_converted_dataNull.xnodes;
yn=OOMMF_converted_dataNull.ynodes;
zn=OOMMF_converted_dataNull.znodes;
%—————

```

```

stepx=3e-9; %cell size in x, propagation direction
stepy=2.08e-9; %cell size in y, propagation direction
%—————
xpos=stepx.*(1:xn);
ypos=stepy.*(1:yn);

Dx = stepx;

dfx = 2*pi/(((OOMMF_converted_Init.xnodes)-1).*Dx); %spatial frequency step k_max =
2*pi*(1/Dx)*0.5; %Nyquist cutoff wavevector (Nyquist theorem)

SimulationKx = (-k_max:dfx:k_max); %build the kx wavevector

D = TimeStep; %sampling time

df = 1/((length(Files)-1).*D); %frequency step

f_max = (1/D)*0.5; %Nyquist cutoff frequency (Nyquist theorem)

SimulationFreq = (1e-9).*(-f_max:df:f_max); %build frequency

SimulationTime=D.*(0:(length(Files))-1); %simulation time array

hammw_f = hanning(length(SimulationFreq)); %define HANNING window for frequency
hammw_x = hanning(length(SimulationKx)); %define HANNING window for x-coordinate
hammw2d = hammw_f*hammw_x.'; %define 2D HANNING window for frequency and x-space
for zeta=1:zn %for loop to generate bandstructure for each z-layer
sweepz=zeta
selZ_idx=sweepz;
Zl=length(selZ_idx);
clear zn
zn=Zl;
parfor k=1:(length(Files))
datafile=[path,Files(k).name];
%%%%%% % when copying to matlab these two text lines must be put in the same code
lines

```

```

realspaceDynM(k, :, :) =
(squeeze(oommf2matlabwithTime(datafile).dataz(:, :, selZ_idx)) - squeeze(mInit(:, :, selZ_idx)));
%%%%%%%%%%%%%%%%%%%%%%%%%%%%%%%%%%%%%%%%%%%%%%%%%%%%%%%%%%%%%%%%%%%%%%%%
%build z-component of dynamic magnetization unit vector m_d
end
parfor zc=1:length(selZ_idx)
for yc=1:yn
dynamicfftM(:, :, yc, zc) = fftn(hammw2d.*squeeze(realspaceDynM(:, :, yc, zc))); %fft in time, x
space for band structure as function of y and z coordinate
end
end
sumZ_FFT_dynM = sum(dynamicfftM, 4); %sum across all z layers (this is trivial in this case
because it is processing one layer at a time)
sumZY_FFT_dynM = sum(sumZ_FFT_dynM, 3); %sum across all y-cells
sumZY_FFT_dynM = sumZY_FFT_dynM / (yn * zn); %compute average across y, z plane
figure
imagesc(SimulationKx, SimulationFreq, 20 * log10(abs(fftshift(sumZY_FFT_dynM)))); %graph
of PSD as function of kx and frequency
axis xy;
xlim([-1.1 * pi / ((18e-9) * (3/2)) 1.1 * pi / ((18e-9) * (3/2))]); %adjust x-range (kx) to observe the first
Brillouin zone (here the boundary is set to 10% larger so to observe the band gap at pi / ((18e-
9) * (3/2))
ylim([0.0 f_coff / 1e9]) % adjust y range (freq. range)
caxis([-105 -10]) % adjust color scale
saveas(gcf, [path, componentM, 'FFT_kx_AbsVal_layerZ', num2str(zeta), '_fig']); %save the gen-
erated image as .fig in matlab
end
end

```


Bibliography

- [1] Brillouin, Léon. “Diffusion de la lumière et des rayons X par un corps transparent homogène - Influence de l’agitation thermique”. In: *Ann. Phys.* 9.17 (1922), pp. 88–122. DOI: 10.1051/anphys/192209170088. URL: <https://doi.org/10.1051/anphys/192209170088>.
- [2] Mandelstam, L. Zh. “Radio-Fiziko-Khimicheskogo Obschestva”. In: 58 (1926), p. 381.
- [3] Lev Davidovich Landau and Evgenii Mikhailovich Lifshitz. “ON THE THEORY OF THE DISPERSION OF MAGNETIC PERMEABILITY IN FERROMAGNETIC BODIES”. In: 1935.
- [4] Charles Kittel. “On the Theory of Ferromagnetic Resonance Absorption”. In: *Phys. Rev.* 73 (2 Jan. 1948), pp. 155–161. DOI: 10.1103/PhysRev.73.155. URL: <https://link.aps.org/doi/10.1103/PhysRev.73.155>.
- [5] Conyers Herring and Charles Kittel. “On the Theory of Spin Waves in Ferromagnetic Media”. In: *Phys. Rev.* 81 (5 Mar. 1951), pp. 869–880. DOI: 10.1103/PhysRev.81.869. URL: <https://link.aps.org/doi/10.1103/PhysRev.81.869>.
- [6] Rosalind E Franklin and Raymond G Gosling. “Molecular configuration in sodium thymonucleate”. In: *Nature* 171 (1953), pp. 740–741.
- [7] James D Watson and Francis HC Crick. “Molecular structure of nucleic acids: a structure for deoxyribose nucleic acid”. In: *Nature* 171.4356 (1953), pp. 737–738.
- [8] Maurice Hugh Frederick Wilkins, Alex R STOKES, and Herbert R Wilson. “Molecular structure of nucleic acids: molecular structure of deoxypentose nucleic acids”. In: *Nature* 171 (1953), pp. 738–740.
- [9] Thomas L. Gilbert. “A Lagrangian Formulation of the Gyromagnetic Equation of the Magnetization Field”. In: *Physical Review D* 100 (1955), p. 1243.
- [10] I. Dzyaloshinsky. “A thermodynamic theory of “weak” ferromagnetism of antiferromagnetics”. In: *Journal of Physics and Chemistry of Solids* 4.4 (1958), pp. 241–255. ISSN: 0022-3697. DOI: [https://doi.org/10.1016/0022-3697\(58\)90076-3](https://doi.org/10.1016/0022-3697(58)90076-3). URL: <https://www.sciencedirect.com/science/article/pii/0022369758900763>.
- [11] Tôru Moriya. “Anisotropic Superexchange Interaction and Weak Ferromagnetism”. In: *Phys. Rev.* 120 (1 Oct. 1960), pp. 91–98. DOI: 10.1103/PhysRev.120.91. URL: <https://link.aps.org/doi/10.1103/PhysRev.120.91>.

- [12] William Fuller Brown. *Micromagnetics*. 18. interscience publishers, 1963.
- [13] J. Sandercock. *Light Scattering in Solids*. Paris: Flammarion Press, 1971.
- [14] S. M. Lindsay, M. W. Anderson, and J. R. Sandercock. “Construction and alignment of a high performance multipass vernier tandem Fabry–Perot interferometer”. In: *Review of Scientific Instruments* 52.10 (1981), pp. 1478–1486. DOI: 10.1063/1.1136479. eprint: <https://doi.org/10.1063/1.1136479>. URL: <https://doi.org/10.1063/1.1136479>.
- [15] Nadrian C. Seeman. “Nucleic acid junctions and lattices”. In: *Journal of Theoretical Biology* 99.2 (1982), pp. 237–247. ISSN: 0022-5193. DOI: [https://doi.org/10.1016/0022-5193\(82\)90002-9](https://doi.org/10.1016/0022-5193(82)90002-9). URL: <https://www.sciencedirect.com/science/article/pii/0022519382900029>.
- [16] B A Kalinikos and A N Slavin. “Theory of dipole-exchange spin wave spectrum for ferromagnetic films with mixed exchange boundary conditions”. In: *Journal of Physics C: Solid State Physics* 19.35 (Dec. 1986), p. 7013. DOI: 10.1088/0022-3719/19/35/014. URL: <https://dx.doi.org/10.1088/0022-3719/19/35/014>.
- [17] Patrick Bruno. “Dipolar magnetic surface anisotropy in ferromagnetic thin films with interfacial roughness”. In: *Journal of Applied Physics* 64.6 (1988), pp. 3153–3156. DOI: 10.1063/1.341530. eprint: <https://doi.org/10.1063/1.341530>. URL: <https://doi.org/10.1063/1.341530>.
- [18] B. Wadell. *Transmission Line Design Handbook*. Artech House, 1991.
- [19] L. Berger. “Emission of spin waves by a magnetic multilayer traversed by a current”. In: *Phys. Rev. B* 54 (13 Oct. 1996), pp. 9353–9358. DOI: 10.1103/PhysRevB.54.9353. URL: <https://link.aps.org/doi/10.1103/PhysRevB.54.9353>.
- [20] A.G. Gurevich and G.A. Melkov. *Magnetization Oscillations and Waves*. CRC Press, 1996.
- [21] J.C. Slonczewski. “Current-driven excitation of magnetic multilayers”. In: *Journal of Magnetism and Magnetic Materials* 159.1 (1996), pp. L1–L7. ISSN: 0304-8853. DOI: [https://doi.org/10.1016/0304-8853\(96\)00062-5](https://doi.org/10.1016/0304-8853(96)00062-5). URL: <https://www.sciencedirect.com/science/article/pii/0304885396000625>.
- [22] J. O. Vasseur et al. “Magnon band structure of periodic composites”. In: *Phys. Rev. B* 54 (2 July 1996), pp. 1043–1049. DOI: 10.1103/PhysRevB.54.1043. URL: <https://link.aps.org/doi/10.1103/PhysRevB.54.1043>.
- [23] Burkard Hillebrands. “Progress in multipass tandem Fabry–Perot interferometry: I. A fully automated, easy to use, self-aligning spectrometer with increased stability and flexibility”. In: *Review of Scientific Instruments* 70.3 (1999), pp. 1589–1598. DOI: 10.1063/1.1149637. eprint: <https://doi.org/10.1063/1.1149637>. URL: <https://doi.org/10.1063/1.1149637>.

- [24] Arne Brataas, Yu. V. Nazarov, and Gerrit E. W. Bauer. “Finite-Element Theory of Transport in Ferromagnet–Normal Metal Systems”. In: *Phys. Rev. Lett.* 84 (11 Mar. 2000), pp. 2481–2484. DOI: 10.1103/PhysRevLett.84.2481. URL: <https://link.aps.org/doi/10.1103/PhysRevLett.84.2481>.
- [25] Jean-Louis Viovy. “Electrophoresis of DNA and other polyelectrolytes: Physical mechanisms”. In: *Rev. Mod. Phys.* 72 (3 July 2000), pp. 813–872. DOI: 10.1103/RevModPhys.72.813. URL: <https://link.aps.org/doi/10.1103/RevModPhys.72.813>.
- [26] Yaroslav Tserkovnyak, Arne Brataas, and Gerrit E. W. Bauer. “Enhanced Gilbert Damping in Thin Ferromagnetic Films”. In: *Phys. Rev. Lett.* 88 (11 Feb. 2002), p. 117601. DOI: 10.1103/PhysRevLett.88.117601. URL: <https://link.aps.org/doi/10.1103/PhysRevLett.88.117601>.
- [27] Yaroslav Tserkovnyak, Arne Brataas, and Gerrit E. W. Bauer. “Spin pumping and magnetization dynamics in metallic multilayers”. In: *Phys. Rev. B* 66 (22 Dec. 2002), p. 224403. DOI: 10.1103/PhysRevB.66.224403. URL: <https://link.aps.org/doi/10.1103/PhysRevB.66.224403>.
- [28] Nadrian C Seeman. “At the Crossroads of Chemistry, Biology, and Materials: Structural DNA Nanotechnology”. In: *Chemistry & Biology* 10.12 (2003), pp. 1151–1159. ISSN: 1074-5521. DOI: <https://doi.org/10.1016/j.chembiol.2003.12.002>. URL: <https://www.sciencedirect.com/science/article/pii/S1074552103002734>.
- [29] Christophe Thirion, Wolfgang Wernsdorfer, and Dominique Maily. “Switching of magnetization by nonlinear resonance studied in single nanoparticles”. In: *Nature Materials* 2 (2003), pp. 524–527. URL: <https://doi.org/10.1038/nmat946>.
- [30] S. Zhang and Z. Li. “Roles of Nonequilibrium Conduction Electrons on the Magnetization Dynamics of Ferromagnets”. In: *Phys. Rev. Lett.* 93 (12 Sept. 2004), p. 127204. DOI: 10.1103/PhysRevLett.93.127204. URL: <https://link.aps.org/doi/10.1103/PhysRevLett.93.127204>.
- [31] C. B. Craus et al. “The influence of the surface topography on the magnetization dynamics in soft magnetic thin films”. In: *Journal of Applied Physics* 97.1 (2005), p. 013904. DOI: 10.1063/1.1819998. eprint: <https://doi.org/10.1063/1.1819998>. URL: <https://doi.org/10.1063/1.1819998>.
- [32] Yu He et al. “Self-Assembly of Hexagonal DNA Two-Dimensional (2D) Arrays”. In: *Journal of the American Chemical Society* 127.35 (2005). PMID: 16131180, pp. 12202–12203. DOI: 10.1021/ja0541938. eprint: <https://doi.org/10.1021/ja0541938>. URL: <https://doi.org/10.1021/ja0541938>.
- [33] P. Rothmund. “Folding DNA to create nanoscale shapes and patterns”. In: *Nature* 440 (2006), pp. 297–302. URL: <https://doi.org/10.1038/nature04586>.
- [34] Joachim Stöhr and H. C. Siegmann. “Magnetism From Fundamentals to Nanoscale Dynamics”. In: 2006.

- [35] L. F. Yin et al. “Magnetocrystalline Anisotropy in Permalloy Revisited”. In: *Phys. Rev. Lett.* 97 (6 Aug. 2006), p. 067203. DOI: 10.1103/PhysRevLett.97.067203. URL: <https://link.aps.org/doi/10.1103/PhysRevLett.97.067203>.
- [36] Jack Bass and William P Pratt. “Spin-diffusion lengths in metals and alloys, and spin-flipping at metal/metal interfaces: an experimentalist’s critical review”. In: *Journal of Physics: Condensed Matter* 19.18 (Apr. 2007), p. 183201. DOI: 10.1088/0953-8984/19/18/183201. URL: <https://dx.doi.org/10.1088/0953-8984/19/18/183201>.
- [37] K. J. Kennewell, M. Kostylev, and R. L. Stamps. “Calculation of spin wave mode response induced by a coplanar microwave line”. In: *Journal of Applied Physics* 101.9 (2007), p. 09D107. DOI: 10.1063/1.2710068. eprint: <https://doi.org/10.1063/1.2710068>. URL: <https://doi.org/10.1063/1.2710068>.
- [38] Joel K. W. Yang and Karl K. Berggren. “Using high-contrast salty development of hydrogen silsesquioxane for sub-10-nm half-pitch lithography”. In: *Journal of Vacuum Science & Technology B: Microelectronics and Nanometer Structures Processing, Measurement, and Phenomena* 25.6 (2007), pp. 2025–2029. DOI: 10.1116/1.2801881. eprint: <https://avs.scitation.org/doi/pdf/10.1116/1.2801881>. URL: <https://avs.scitation.org/doi/abs/10.1116/1.2801881>.
- [39] Sergej O. Demokritov and Vladislav E. Demidov. “Micro-Brillouin Light Scattering Spectroscopy of Magnetic Nanostructures”. In: *IEEE Transactions on Magnetics* 44.1 (2008), pp. 6–12. DOI: 10.1109/TMAG.2007.910227.
- [40] M. Heide, G. Bihlmayer, and S. Blügel. “Dzyaloshinskii-Moriya interaction accounting for the orientation of magnetic domains in ultrathin films: Fe/W(110)”. In: *Phys. Rev. B* 78 (14 Oct. 2008), p. 140403. DOI: 10.1103/PhysRevB.78.140403. URL: <https://link.aps.org/doi/10.1103/PhysRevB.78.140403>.
- [41] M. Krawczyk and H. Puzskarski. “Plane-wave theory of three-dimensional magnonic crystals”. In: *Phys. Rev. B* 77 (5 Feb. 2008), p. 054437. DOI: 10.1103/PhysRevB.77.054437. URL: <https://link.aps.org/doi/10.1103/PhysRevB.77.054437>.
- [42] Rudolf Schäfer and Alex Hubert. *Magnetic Domains*. Springer / Springer Berlin Heidelberg / Springer, Berlin, 2008.
- [43] Jørn Foros et al. “Noise and dissipation in magnetoelectronic nanostructures”. In: *Phys. Rev. B* 79 (21 June 2009), p. 214407. DOI: 10.1103/PhysRevB.79.214407. URL: <https://link.aps.org/doi/10.1103/PhysRevB.79.214407>.
- [44] Wolfgang Nolting and Anupuru Ramakanth. *Quantum Theory of Magnetism*. Springer Berlin, Heidelberg, 2009.
- [45] L. Udvardi and L. Szunyogh. “Chiral Asymmetry of the Spin-Wave Spectra in Ultrathin Magnetic Films”. In: *Phys. Rev. Lett.* 102 (20 May 2009), p. 207204. DOI: 10.1103/PhysRevLett.102.207204. URL: <https://link.aps.org/doi/10.1103/PhysRevLett.102.207204>.

- [46] John C. Slonczewski. “Initiation of spin-transfer torque by thermal transport from magnons”. In: *Phys. Rev. B* 82 (5 Aug. 2010), p. 054403. DOI: 10.1103/PhysRevB.82.054403. URL: <https://link.aps.org/doi/10.1103/PhysRevB.82.054403>.
- [47] I Barsukov et al. “Frequency dependence of spin relaxation in periodic systems”. In: *Physical Review B* 84.14 (2011), p. 140410.
- [48] S. Neusser. “Spin waves in antidot lattices: From quantization to magnonic crystals”. Dissertation. Technische Universität München, München, 2011.
- [49] Jesús Tamarit-López et al. “Oxygen Plasma Treated Interactive Polycarbonate DNA Microarraying Platform”. In: *Bioconjugate Chemistry* 22.12 (2011). PMID: 22044406, pp. 2573–2580. DOI: 10.1021/bc2004268. eprint: <https://doi.org/10.1021/bc2004268>. URL: <https://doi.org/10.1021/bc2004268>.
- [50] P. Yan, X. S. Wang, and X. R. Wang. “All-Magnonic Spin-Transfer Torque and Domain Wall Propagation”. In: *Phys. Rev. Lett.* 107 (17 Oct. 2011), p. 177207. DOI: 10.1103/PhysRevLett.107.177207. URL: <https://link.aps.org/doi/10.1103/PhysRevLett.107.177207>.
- [51] Anton Kuzyk et al. “DNA-based self-assembly of chiral plasmonic nanostructures with tailored optical response”. In: *Nature* 483 (2012), pp. 311–314. URL: <https://doi.org/10.1038/nature10889>.
- [52] Yubing Xie. *The Nanobiotechnology Handbook*. CRC Press, 2012.
- [53] Haiming Yu et al. “High propagating velocity of spin waves and temperature dependent damping in a CoFeB thin film”. In: *Applied Physics Letters* 100.26 (2012), p. 262412. DOI: 10.1063/1.4731273. eprint: <https://doi.org/10.1063/1.4731273>. URL: <https://doi.org/10.1063/1.4731273>.
- [54] Gavin S. Abo et al. “Definition of Magnetic Exchange Length”. In: *IEEE Transactions on Magnetics* 49.8 (2013), pp. 4937–4939. DOI: 10.1109/TMAG.2013.2258028.
- [55] A. Fert, V. Cros, and J. Sampaio. “Skyrmions on the track”. In: *Nature Nanotechnology* 8 (2013), pp. 152–156. URL: <https://doi.org/10.1038/nnano.2013.29>.
- [56] Jayavardhana Gubbi et al. “Internet of Things (IoT): A vision, architectural elements, and future directions”. In: *Future Generation Computer Systems* 29.7 (2013). Including Special sections: Cyber-enabled Distributed Computing for Ubiquitous Cloud and Network Services & Cloud Computing and Scientific Applications — Big Data, Scalable Analytics, and Beyond, pp. 1645–1660. ISSN: 0167-739X. DOI: <https://doi.org/10.1016/j.future.2013.01.010>. URL: <https://www.sciencedirect.com/science/article/pii/S0167739X13000241>.
- [57] M. Körner et al. “Two-magnon scattering in permalloy thin films due to rippled substrates”. In: *Phys. Rev. B* 88 (5 Aug. 2013), p. 054405. DOI: 10.1103/PhysRevB.88.054405. URL: <https://link.aps.org/doi/10.1103/PhysRevB.88.054405>.

- [58] Jung-Hwan Moon et al. “Spin-wave propagation in the presence of interfacial Dzyaloshinskii-Moriya interaction”. In: *Phys. Rev. B* 88 (18 Nov. 2013), p. 184404. DOI: 10.1103/PhysRevB.88.184404. URL: <https://link.aps.org/doi/10.1103/PhysRevB.88.184404>.
- [59] Schwarze T. “Spin Waves in 2D and 3D Magnonic Crystals: From Nanostructured Ferromagnetic Materials to Chiral Helimagnets”. Dissertation. Technische Universität München, München, 2013.
- [60] Haiming Yu et al. “Omnidirectional spin-wave nanograting coupler”. In: *Nature Communications* 4 (2013). eprint: <https://doi.org/10.1063/1.2710068>. URL: <https://doi.org/10.1038/ncomms3702>.
- [61] Vikash Bhardwaj. *Science behind Non-Specific Science; For Molecular Biologist & Biotechnologist*. May 2014. ISBN: 9789384049430.
- [62] Crosby S. Chang et al. “The phase accumulation and antenna near field of microscopic propagating spin wave devices”. In: *Applied Physics Letters* 104.3 (2014), p. 032408. DOI: 10.1063/1.4863078. eprint: <https://doi.org/10.1063/1.4863078>. URL: <https://doi.org/10.1063/1.4863078>.
- [63] M Krawczyk and D Grundler. “Review and prospects of magnonic crystals and devices with reprogrammable band structure”. In: *Journal of Physics: Condensed Matter* 26.12 (Mar. 2014), p. 123202. DOI: 10.1088/0953-8984/26/12/123202. URL: <https://dx.doi.org/10.1088/0953-8984/26/12/123202>.
- [64] Li Huey Tan, Hang Xing, and Yi Lu. “DNA as a Powerful Tool for Morphology Control, Spatial Positioning, and Dynamic Assembly of Nanoparticles”. In: *Accounts of Chemical Research* 47.6 (2014). PMID: 24871359, pp. 1881–1890. DOI: 10.1021/ar500081k. eprint: <https://doi.org/10.1021/ar500081k>. URL: <https://doi.org/10.1021/ar500081k>.
- [65] Arne Vansteenkiste et al. “The design and verification of MuMax3”. In: *AIP Advances* 4.10 (2014), p. 107133. DOI: 10.1063/1.4899186. eprint: <https://doi.org/10.1063/1.4899186>. URL: <https://doi.org/10.1063/1.4899186>.
- [66] Hailong Wang et al. “Antiferromagnonic Spin Transport from $Y_3Fe_5O_{12}$ into NiO”. In: *Phys. Rev. Lett.* 113 (9 Aug. 2014), p. 097202. DOI: 10.1103/PhysRevLett.113.097202. URL: <https://link.aps.org/doi/10.1103/PhysRevLett.113.097202>.
- [67] Xufeng Zhang et al. “Strongly Coupled Magnons and Cavity Microwave Photons”. In: *Phys. Rev. Lett.* 113 (15 Oct. 2014), p. 156401. DOI: 10.1103/PhysRevLett.113.156401. URL: <https://link.aps.org/doi/10.1103/PhysRevLett.113.156401>.
- [68] A. V. Chumak et al. “Magnon spintronics”. In: *Nature Physics* 11 (2015), pp. 453–461. URL: <https://doi.org/10.1038/nphys3347>.
- [69] Vladislav E. Demidov and Sergej O. Demokritov. “Magnonic Waveguides Studied by Microfocus Brillouin Light Scattering”. In: *IEEE Transactions on Magnetics* 51.4 (2015), pp. 1–15. DOI: 10.1109/TMAG.2014.2388196.

- [70] M. Haertinger et al. “Spin pumping in YIG/Pt bilayers as a function of layer thickness”. In: *Phys. Rev. B* 92 (5 Aug. 2015), p. 054437. DOI: 10.1103/PhysRevB.92.054437. URL: <https://link.aps.org/doi/10.1103/PhysRevB.92.054437>.
- [71] Thomas Sebastian et al. “Micro-focused Brillouin light scattering: imaging spin waves at the nanoscale”. In: *Frontiers in Physics* 3 (2015). ISSN: 2296-424X. DOI: 10.3389/fphy.2015.00035. URL: <https://www.frontiersin.org/articles/10.3389/fphy.2015.00035>.
- [72] Jairo Sinova et al. “Spin Hall effects”. In: *Rev. Mod. Phys.* 87 (4 Oct. 2015), pp. 1213–1260. DOI: 10.1103/RevModPhys.87.1213. URL: <https://link.aps.org/doi/10.1103/RevModPhys.87.1213>.
- [73] Hugo K. Christenson and Neil H. Thomson. “The nature of the air-cleaved mica surface”. In: *Surface Science Reports* 71.2 (2016), pp. 367–390. ISSN: 0167-5729. DOI: <https://doi.org/10.1016/j.surfrep.2016.03.001>. URL: <https://www.sciencedirect.com/science/article/pii/S0167572916000066>.
- [74] Cheikh Tidiane Diagne et al. “DNA Origami Mask for Sub-Ten-Nanometer Lithography”. In: *ACS Nano* 10.7 (2016). PMID: 27281227, pp. 6458–6463. DOI: 10.1021/acsnano.6b00413. eprint: <https://doi.org/10.1021/acsnano.6b00413>. URL: <https://doi.org/10.1021/acsnano.6b00413>.
- [75] Jonas J Funke and Hendrik Dietz. “Placing molecules with Bohr radius resolution using DNA origami”. In: *Nature nanotechnology* 11.1 (2016), pp. 47–52.
- [76] Ashwin Gopinath et al. “Engineering and mapping nanocavity emission via precision placement of DNA origami”. In: *Nature* 535 (2016), pp. 401–405. URL: <https://doi.org/10.1038/nature18287>.
- [77] Joo-Von Kim, Robert L. Stamps, and Robert E. Camley. “Spin Wave Power Flow and Caustics in Ultrathin Ferromagnets with the Dzyaloshinskii-Moriya Interaction”. In: *Phys. Rev. Lett.* 117 (19 Nov. 2016), p. 197204. DOI: 10.1103/PhysRevLett.117.197204. URL: <https://link.aps.org/doi/10.1103/PhysRevLett.117.197204>.
- [78] Haiming Yu et al. “Approaching soft X-ray wavelengths in nanomagnet-based microwave technology”. In: *Nature Communications* 7 (2016). URL: <https://doi.org/10.1038/ncomms11255>.
- [79] Alessandro Cecconello et al. “Chiroplasmonic DNA-based nanostructures”. In: *Nature Reviews Materials* 2 (9 2017). DOI: 10.1038/natrevmats.2017.39. URL: <https://doi.org/10.1038/natrevmats.2017.39>.
- [80] Nadrian C. Seeman and Hanadi F. Sleiman. “DNA nanotechnology”. In: *Nature Reviews Materials* 3 (1 2017). DOI: 10.1038/natrevmats.2017.68. URL: <https://doi.org/10.1038/natrevmats.2017.68>.
- [81] S. Woo, T. Delaney, and G. Beach. “Magnetic domain wall depinning assisted by spin wave bursts”. In: *Nature Physics* 13 (2017), pp. 448–454. URL: <https://doi.org/10.1038/nphys4022>.

- [82] J. Wunderlich. “Current-switched magnetic insulator”. In: *Nature Materials* 16 (2017), pp. 284–285. URL: <https://doi.org/10.1038/nmat4862>.
- [83] Jilei Chen et al. “Strong Interlayer Magnon-Magnon Coupling in Magnetic Metal-Insulator Hybrid Nanostructures”. In: *Phys. Rev. Lett.* 120 (21 May 2018), p. 217202. DOI: 10.1103/PhysRevLett.120.217202. URL: <https://link.aps.org/doi/10.1103/PhysRevLett.120.217202>.
- [84] Yi Chen et al. “Different Stability of DNA Origami Nanostructure between on Interface and in Bulk Solution”. In: *ACS Applied Bio Materials* 1.5 (2018), pp. 1424–1429. DOI: 10.1021/acsabm.8b00379. eprint: <https://doi.org/10.1021/acsabm.8b00379>. URL: <https://doi.org/10.1021/acsabm.8b00379>.
- [85] R. A. Gallardo et al. “Dipolar interaction induced band gaps and flat modes in surface-modulated magnonic crystals”. In: *Phys. Rev. B* 97 (14 Apr. 2018), p. 144405. DOI: 10.1103/PhysRevB.97.144405. URL: <https://link.aps.org/doi/10.1103/PhysRevB.97.144405>.
- [86] Fatih N. Gür et al. “DNA-Assembled Plasmonic Waveguides for Nanoscale Light Propagation to a Fluorescent Nanodiamond”. In: *Nano Letters* 18.11 (2018). PMID: 30339400, pp. 7323–7329. DOI: 10.1021/acs.nanolett.8b03524. eprint: <https://doi.org/10.1021/acs.nanolett.8b03524>. URL: <https://doi.org/10.1021/acs.nanolett.8b03524>.
- [87] Charlotte Kielar et al. “Dynamics of DNA Origami Lattice Formation at Solid–Liquid Interfaces”. In: *ACS Applied Materials & Interfaces* 10.51 (2018), pp. 44844–44853. DOI: 10.1021/acsami.8b16047. eprint: <https://doi.org/10.1021/acsami.8b16047>. URL: <https://doi.org/10.1021/acsami.8b16047>.
- [88] Stefan Klingler et al. “Spin-Torque Excitation of Perpendicular Standing Spin Waves in Coupled YIG/Co Heterostructures”. In: *Phys. Rev. Lett.* 120 (12 Mar. 2018), p. 127201. DOI: 10.1103/PhysRevLett.120.127201. URL: <https://link.aps.org/doi/10.1103/PhysRevLett.120.127201>.
- [89] Chuanpu Liu et al. “Long-distance propagation of short-wavelength spin waves”. In: *Nature communications* 9.1 (2018), p. 738.
- [90] Huajun Qin et al. “Exchange-torque-induced excitation of perpendicular standing spin waves in nanometer-thick YIG films”. In: *Scientific Reports* 8 (2018). URL: <https://doi.org/10.1038/s41598-018-23933-y>.
- [91] Yiheng Rao et al. “Thickness dependence of magnetic properties in submicron yttrium iron garnet films”. In: *Journal of Physics D: Applied Physics* 51.43 (Sept. 2018), p. 435001. DOI: 10.1088/1361-6463/aade43. URL: <https://dx.doi.org/10.1088/1361-6463/aade43>.
- [92] Boxuan Shen et al. “Plasmonic nanostructures through DNA-assisted lithography”. In: *Science Advances* 4.2 (2018), eaap8978. DOI: 10.1126/sciadv.aap8978. eprint: <https://www.science.org/doi/pdf/10.1126/sciadv.aap8978>. URL: <https://www.science.org/doi/abs/10.1126/sciadv.aap8978>.
- [93] Gyeongho Son et al. In: *Nanophotonics* 7.12 (2018), pp. 1845–1864. DOI: doi:10.1515/nanoph-2018-0075. URL: <https://doi.org/10.1515/nanoph-2018-0075>.

- [94] Hongkang Xie et al. “Effect of substrate roughness on the magnetic properties of CoFeB films”. In: *Journal of Magnetism and Magnetic Materials* 461 (2018), pp. 19–22. ISSN: 0304-8853. DOI: <https://doi.org/10.1016/j.jmmm.2018.04.046>. URL: <https://www.sciencedirect.com/science/article/pii/S0304885317335151>.
- [95] Victor A. S. V. Bittencourt, Verena Feulner, and Silvia Viola Kusminskiy. “Magnon heralding in cavity optomagnonics”. In: *Phys. Rev. A* 100 (1 July 2019), p. 013810. DOI: 10.1103/PhysRevA.100.013810. URL: <https://link.aps.org/doi/10.1103/PhysRevA.100.013810>.
- [96] Jilei Chen et al. “Excitation of unidirectional exchange spin waves by a nanoscale magnetic grating”. In: *Phys. Rev. B* 100 (10 Sept. 2019), p. 104427. DOI: 10.1103/PhysRevB.100.104427. URL: <https://link.aps.org/doi/10.1103/PhysRevB.100.104427>.
- [97] M. Langer et al. “Spin-wave modes in transition from a thin film to a full magnonic crystal”. In: *Phys. Rev. B* 99 (2 Jan. 2019), p. 024426. DOI: 10.1103/PhysRevB.99.024426. URL: <https://link.aps.org/doi/10.1103/PhysRevB.99.024426>.
- [98] Christine R. Laramy, Matthew N. O’Brien, and Chad A. Mirkin. “Crystal engineering with DNA”. In: *Nature Reviews Materials* 4 (Mar. 2019), pp. 201–224. DOI: 10.1038/s41578-019-0087-2.
- [99] Mikael Madsen and Kurt V. Gothelf. “Chemistries for DNA Nanotechnology”. In: *Chemical Reviews* 119.10 (2019), pp. 6384–6458. DOI: 10.1021/acs.chemrev.8b00570. eprint: <https://doi.org/10.1021/acs.chemrev.8b00570>. URL: <https://doi.org/10.1021/acs.chemrev.8b00570>.
- [100] A. Manchon et al. “Current-induced spin-orbit torques in ferromagnetic and antiferromagnetic systems”. In: *Rev. Mod. Phys.* 91 (3 Sept. 2019), p. 035004. DOI: 10.1103/RevModPhys.91.035004. URL: <https://link.aps.org/doi/10.1103/RevModPhys.91.035004>.
- [101] Adrian P. Nievergelt et al. “High-Speed Atomic Force Microscopy: Large-Range HS-AFM Imaging of DNA Self-Assembly through In Situ Data-Driven Control (Small Methods 7/2019)”. In: *Small Methods* 3.7 (2019), p. 1970022. DOI: <https://doi.org/10.1002/smt.201970022>. eprint: <https://onlinelibrary.wiley.com/doi/pdf/10.1002/smt.201970022>. URL: <https://onlinelibrary.wiley.com/doi/abs/10.1002/smt.201970022>.
- [102] Petteri Piskunen et al. “DNA Origami-Mediated Substrate Nanopatterning of Inorganic Structures for Sensing Applications”. In: *JoVE (Journal of Visualized Experiments)* 151 (2019), e60313.
- [103] Roman Verba, Vasil Tiberkevich, and Andrei Slavin. “Hamiltonian formalism for nonlinear spin wave dynamics under antisymmetric interactions: Application to Dzyaloshinskii-Moriya interaction”. In: *Phys. Rev. B* 99 (17 May 2019), p. 174431. DOI: 10.1103/PhysRevB.99.174431. URL: <https://link.aps.org/doi/10.1103/PhysRevB.99.174431>.

- [104] Yi Wang et al. “Magnetization switching by magnon-mediated spin torque through an antiferromagnetic insulator”. In: *Science* 366.6469 (2019), pp. 1125–1128. DOI: 10.1126/science.aav8076. eprint: <https://www.science.org/doi/pdf/10.1126/science.aav8076>. URL: <https://www.science.org/doi/abs/10.1126/science.aav8076>.
- [105] Tao Yu, Yaroslav M. Blanter, and Gerrit E. W. Bauer. “Chiral Pumping of Spin Waves”. In: *Phys. Rev. Lett.* 123 (24 Dec. 2019), p. 247202. DOI: 10.1103/PhysRevLett.123.247202. URL: <https://link.aps.org/doi/10.1103/PhysRevLett.123.247202>.
- [106] Ali Aghebat Rafat et al. “Barcoded DNA origami structures for multiplexed optimization and enrichment of DNA-based protein-binding cavities”. In: *Nature chemistry* 12.9 (2020), pp. 852–859.
- [107] Ping Che et al. “Efficient wavelength conversion of exchange magnons below 100nm by magnetic coplanar waveguides”. In: *Nature Communications* 11 (2020). URL: <https://doi.org/10.1038/s41467-020-15265-1>.
- [108] Fabio Cramer, Grace E Shephard, and Philip J Heron. “The misuse of colour in science communication”. In: *Nature communications* 11.1 (2020), p. 5444.
- [109] Marcello DeLuca et al. “Dynamic DNA nanotechnology: toward functional nanoscale devices”. In: *Nanoscale Horiz.* 5 (2 2020), pp. 182–201. DOI: 10.1039/C9NH00529C. URL: <http://dx.doi.org/10.1039/C9NH00529C>.
- [110] Carsten Dubs et al. “Low damping and microstructural perfection of sub-40nm-thin yttrium iron garnet films grown by liquid phase epitaxy”. In: *Phys. Rev. Mater.* 4 (2 Feb. 2020), p. 024416. DOI: 10.1103/PhysRevMaterials.4.024416. URL: <https://link.aps.org/doi/10.1103/PhysRevMaterials.4.024416>.
- [111] Ezio Iacocca, Sebastian Gliga, and Olle G. Heinonen. “Tailoring Spin-Wave Channels in a Reconfigurable Artificial Spin Ice”. In: *Phys. Rev. Appl.* 13 (4 Apr. 2020), p. 044047. DOI: 10.1103/PhysRevApplied.13.044047. URL: <https://link.aps.org/doi/10.1103/PhysRevApplied.13.044047>.
- [112] H. Ramezani and H. Dietz. “Building machines with DNA molecules”. In: *Nature Reviews Genetics* 21 (2020), pp. 5–26. URL: <https://doi.org/10.1038/s41576-019-0175-6>.
- [113] Lior Shani et al. “DNA-assembled superconducting 3D nanoscale architectures”. In: *Nature Communications* 11 (2020). URL: <https://doi.org/10.1038/s41467-020-19439-9>.
- [114] Hanchen Wang et al. “Chiral Spin-Wave Velocities Induced by All-Garnet Interfacial Dzyaloshinskii-Moriya Interaction in Ultrathin Yttrium Iron Garnet Films”. In: *Phys. Rev. Lett.* 124 (2 Jan. 2020), p. 027203. DOI: 10.1103/PhysRevLett.124.027203. URL: <https://link.aps.org/doi/10.1103/PhysRevLett.124.027203>.
- [115] Korbinian Baumgaertl. “Magnonic crystals with reconfigurable magnetic defects for spin-based microwave electronics”. PhD thesis. EPFL, 2021.
- [116] P. Che. “Helimagnons and Skyrmion Dynamics in Cu₂OSeO₃ and Fe/Gd Multilayers Explored by Brillouin Light Scattering and X-ray Microscopy”. PhD thesis. EPFL, 2021.

- [117] Zhiren Chen et al. “Magnon Torque Transferred into a Magnetic Insulator through an Antiferromagnetic Insulator”. In: *Nanomaterials* 11.11 (2021). ISSN: 2079-4991. DOI: 10.3390/nano11112766. URL: <https://www.mdpi.com/2079-4991/11/11/2766>.
- [118] Swarup Dey et al. “DNA origami”. In: *Nature Reviews Methods Primers* 1.1 (2021), p. 13.
- [119] M. C. Giordano. “Atomic layer deposition of Ni and Ni₈₀Fe₂₀ for tubular spin-wave nanocavities”. PhD thesis. EPFL, 2021.
- [120] Christopher M. Green et al. “Correlative Super-Resolution and Atomic Force Microscopy of DNA Nanostructures and Characterization of Addressable Site Defects”. In: *ACS Nano* 15.7 (2021). PMID: 34137595, pp. 11597–11606. DOI: 10.1021/acsnano.1c01976. eprint: <https://doi.org/10.1021/acsnano.1c01976>. URL: <https://doi.org/10.1021/acsnano.1c01976>.
- [121] C. Y. Guo et al. “Switching the perpendicular magnetization of a magnetic insulator by magnon transfer torque”. In: *Phys. Rev. B* 104 (9 Sept. 2021), p. 094412. DOI: 10.1103/PhysRevB.104.094412. URL: <https://link.aps.org/doi/10.1103/PhysRevB.104.094412>.
- [122] Shengbo Liu et al. “DNA-based plasmonic nanostructures and their optical and biomedical applications”. In: *Nanotechnology* 32.40 (July 2021), p. 402002. DOI: 10.1088/1361-6528/ac0d1c. URL: <https://dx.doi.org/10.1088/1361-6528/ac0d1c>.
- [123] David L. Nelson and Michael Cox. *Principles of Biochemistry*. WH Freeman New York, 2021.
- [124] Qiming Shao et al. “Roadmap of Spin–Orbit Torques”. In: *IEEE Transactions on Magnetism* 57.7 (2021), pp. 1–39. DOI: 10.1109/TMAG.2021.3078583.
- [125] Hanchen Wang et al. “Sub-50nm wavelength spin waves excited by low-damping Co₂₅Fe₇₅ nanowires”. In: *Applied Physics Letters* 119.15 (2021), p. 152402. DOI: 10.1063/5.0064134.
- [126] Hanchen Wang et al. “Tunable Damping in Magnetic Nanowires Induced by Chiral Pumping of Spin Waves”. In: *ACS Nano* 15.5 (2021). PMID: 33977721, pp. 9076–9083. DOI: 10.1021/acsnano.1c02250. eprint: <https://doi.org/10.1021/acsnano.1c02250>. URL: <https://doi.org/10.1021/acsnano.1c02250>.
- [127] S. Watanabe. “Magnons, worms and nanogratings in artificial magnetic quasicrystals”. PhD thesis. EPFL, 2021.
- [128] Timothée P. Allenet et al. “On EUV resist screening with interference lithography in H1-2022”. In: *International Conference on Extreme Ultraviolet Lithography 2022*. Ed. by Toshiro Itani et al. Vol. PC12292. International Society for Optics and Photonics. SPIE, 2022, PC122920C. DOI: 10.1117/12.2641837. URL: <https://doi.org/10.1117/12.2641837>.
- [129] Neil W Ashcroft and N David Mermin. *Solid state physics*. Cengage Learning, 2022.
- [130] Viola Krizakova et al. “Spin-orbit torque switching of magnetic tunnel junctions for memory applications”. In: *Journal of Magnetism and Magnetic Materials* 562 (2022), p. 169692. ISSN: 0304-8853. DOI: <https://doi.org/10.1016/j.jmmm.2022.169692>. URL: <https://www.sciencedirect.com/science/article/pii/S0304885322006023>.

- [131] Wittrock S. et al. *in preparation*. 2023.
- [132] K. An et al. *Optimizing the magnon-phonon cooperativity in planar geometries*. 2023. DOI: 10.48550/ARXIV.2302.09936. URL: <https://arxiv.org/abs/2302.09936>.
- [133] Korbinian Baumgaertl and Dirk Grundler. “Reversal of nanomagnets by propagating magnons in ferrimagnetic yttrium iron garnet enabling nonvolatile magnon memory”. In: *Nature Communications* 14.1 (2023), p. 1490.
- [134] Katherine E. Dunn and Alistair Elfick. “Harnessing DNA Nanotechnology and Chemistry for Applications in Photonics and Electronics”. In: *Bioconjugate Chemistry* 34.1 (2023). PMID: 36121896, pp. 97–104. DOI: 10.1021/acs.bioconjchem.2c00286. eprint: <https://doi.org/10.1021/acs.bioconjchem.2c00286>. URL: <https://doi.org/10.1021/acs.bioconjchem.2c00286>.
- [135] Takian Fakhrol et al. “Influence of substrate on interfacial Dzyaloshinskii-Moriya interaction in epitaxial $\text{Tm}_3\text{Fe}_5\text{O}_{12}$ films”. In: *Phys. Rev. B* 107 (5 Feb. 2023), p. 054421. DOI: 10.1103/PhysRevB.107.054421. URL: <https://link.aps.org/doi/10.1103/PhysRevB.107.054421>.
- [136] Oscar Lee et al. “Nonlinear Magnon Polaritons”. In: *Physical review letters* 130.4 (2023), p. 046703.
- [137] Amrit Kumar Mondal et al. “Bias field orientation driven reconfigurable magnonics and magnonmagnon coupling in triangular shaped $\text{Ni}_{80}\text{Fe}_{20}$ nanodot arrays”. In: *Nanotechnology* 34.13 (Jan. 2023), p. 135701. DOI: 10.1088/1361-6528/acae5e. URL: <https://dx.doi.org/10.1088/1361-6528/acae5e>.
- [138] Zhihao Wang et al. “Sulfonium-Functionalized Polystyrene-Based Nonchemically Amplified Resists Enabling Sub-13 nm Nanolithography”. In: *ACS Applied Materials & Interfaces* 15.1 (2023). PMID: 36578201, pp. 2289–2300. DOI: 10.1021/acsami.2c19940. eprint: <https://doi.org/10.1021/acsami.2c19940>. URL: <https://doi.org/10.1021/acsami.2c19940>.
- [139] URL: <https://optics.org/news/9/10/36>.
- [140] URL: <https://bastingslab.com/research/>.
- [141] URL: <https://www.tilibit.com/>.
- [142] URL: <https://github.com/grahamrow/Muview2>.
- [143] URL: <http://doi.org/10.5281/zenodo.1243862>.
- [144] URL: <http://tablestable.com/en/products/view/39/>.
- [145] URL: <https://www.epfl.ch/labs/lbni/>.
- [146] Marcello DeLuca et al. “Prediction and Control in DNA Nanotechnology”. In: *ACS Applied Bio Materials* 0.0 (0). PMID: 36880799, null. DOI: 10.1021/acsabm.2c01045. eprint: <https://doi.org/10.1021/acsabm.2c01045>. URL: <https://doi.org/10.1021/acsabm.2c01045>.

Andrea Mucchietto

a.mucchietto@gmail.com
+41782290949

PROFESSIONAL SUMMARY

Ph.D. candidate in materials science and engineering with 4 years experience in nanomagnetism, nanofabrication, synthesis of DNA nanostructures and micromagnetic modelling. My experimental skillset covers: electrical and optical characterization of magnetic nanodevices, hands-on experience with RF/microwave setup, light scattering-based optical setup and scanning probe microscopy setups.

TECHNICAL SKILLS

Nanofabrication

- Electron beam lithography and photolithography
- Dry and wet etching
- Thin film evaporation and sputtering
- Device design (CAD software: KLayout)

Materials characterization

- Scanning electron microscope (SEM)
- Atomic and magnetic force microscopy (AFM/MFM)
- Brillouin light scattering (BLS)
- RF/Microwave spectroscopy with Vector Network Analyzer (VNA)
- Scanning tunneling microscopy (STM)
- Gel electrophoresis

Experimental skills

- AFM/MFM setup, measurements and maintenance
- Interferometric laser-based optical setup (BLS) with RF microwave station, measurements and maintenance
- RF electrical characterization setup (VNA) calibration
- STM and ultra-high-vacuum systems, measurements and maintenance
- Preparation and handling of 2D lattices based on DNA self-assembly

Data analysis

- Data analysis and visualization with MATLAB and OriginLab
- Data analysis and visualization with Python

Numerical modelling

- MuMax³ and OOMMF micromagnetic modelling of magnetostatics and magnetodynamics

EDUCATION

- **Ph.D. in Materials Science and Engineering** *Dec 2018 - Apr 2023 (expected)*

École polytechnique fédérale de Lausanne, Switzerland

Thesis supervisor: Prof. Dr. Dirk Grundler, Laboratory of Nanoscale Magnetic Materials and Magnonics

- **M.Sc. in Electrical Engineering** *Sep 2016 - Sep 2018*

Polytechnic University of Turin, Italy

I was accepted for an international joint degree program during which I conducted:
one academic semester at INP-PHELMA (FR)
one academic semester at EPFL (CH)

Thesis supervisor: Prof. Dr. Dirk Grundler, Laboratory of Nanoscale Magnetic Materials and Magnonics

- **B.Sc. in Physics** *Sep 2012 - Mar 2016*

University of Trieste, Italy

Thesis supervisor: Dr. Luca Floreano, IOM-CNR, Trieste

PUBLICATIONS

- Giordano, M. C., Hamdi, M., Mucchietto, A., & Grundler, D. (2023). Confined spin waves in magnetochiral nanotubes with axial and circumferential magnetization. *Physical Review Materials*, 7(2), 024405.

Personal contribution: Brillouin light scattering microscopy experiments with RF station and phase resolution, participation in data analysis, discussion and manuscript writing.

- Kúkolová, A., Escobar Steinvall, S., Paul, R., Leran, J., Che, P., Hamdi, M., Mucchietto, A., Grundler, D. and Fontcuberta i Morral, A., 2021. van der Waals Epitaxy of $\text{Co}_{10-x}\text{Zn}_{10-y}\text{Mn}_{x+y}$ Thin Films: Chemical Composition Engineering and Magnetic Properties. *The Journal of Physical Chemistry C*, 125(17), pp.9391-9399.

Personal contribution: Atomic force microscopy measurements and support by Brillouin light scattering microscopy.

- Che, P., Stasinopoulos, I., Mucchietto, A., Li, J., Berger, H., Bauer, A., Pfeiderer, C. and Grundler, D., 2021. Confined dipole and exchange spin waves in a bulk chiral magnet with Dzyaloshinskii-Moriya interaction. *Physical Review Research*, 3(3).

Personal contribution: Micromagnetic modelling of magnetization dynamics, data discussion and manuscript revision.

- Baumgaertl, K., Gräfe, J., Che, P., Mucchietto, A., Förster, J., Träger, N., Bechtel, M., Weigand, M., Schütz, G. and Grundler, D., 2020. Nanoimaging of Ultrashort Magnon Emission by Ferromagnetic Grating Couplers at GHz Frequencies. *Nano Letters*, 20(10), pp.7281-7286.

Personal contribution: Participation in X-ray transmission measurements, discussion and interpretation of experimental results

CONFERENCES AND WORKSHOPS

- Poster contribution at Swiss Physical Society (SPS) meeting, Lausanne 2018
- Poster contribution at Magnonics 2022 conference, Oxnard 2022
- Poster contribution at NeuroSpin 2022 summer school, Lausanne 2022
- Contributed talk at MMM2022 conference, Minneapolis 2022

FURTHER RESEARCH EXPERIENCE

- **Synchrotron beamtimes** - BESSY II, Berlin, Germany - *during PhD research*
 - Small angle x-ray scattering (SAXS) to investigate non-linear spin-wave dynamics
(October 2022)
 - X-ray magnetic circular dichroism (XMCD) to explore magnon interaction with different non-collinear magnetic spin textures
(January 2020)
 - XMCD for real-space imaging of magnon excitation via magnonic grating coupler effect
(May 2019)
- **Research Internship** - KTH, Stockholm, Sweden - *Jun-Aug 2017*

Project: Integration of hybrid-plasmonic infrared nanobolometer.

Main task(s): Optical setup for characterization of plasmonic nanobolometers in the mid infrared range.

Supervisors: Dr. Ottonello Briano, Prof. K. Gylfasson
- **Term contract technician** - A.P.E. Research S.R.L., Trieste, Italy - *Jun-Aug 2016*

Project: Upgrade sample transfer system for ultra-high-vacuum system hosting STM setup.

Main task(s): Upgrade of the sample transfer system for an experimental ultra-high-vacuum system hosting STM setup. STM investigations of metal-organic interfaces.

This job continued my accomplished work during the bachelor thesis in Dr. Floreano's group.

FURTHER PAST ACTIVITIES

Project supervision and management

During PhD: I have supervised four undergraduate student projects (each lasting 4 months). My duties covered: project planning, defining timeline and deliverables, student supervision. The projects addressed micromagnetic modelling of magnon dispersion in one- and two-dimensional periodically patterned magnetic thin films and experimental AFM characterization of DNA origami on mica substrates.

Laboratory safety management

Sep 2019 - May 2022: I was safety correspondent in my research unit during my PhD. I was responsible for implementing, maintaining and upgrading safety measures in labs and offices. (duration: Sep 2019 - May 2022)